# SANDIA REPORT

SAND2010-6498

Unlimited Release

Printed September 2010

# Studies of the Viscoelastic Properties of Water Confined Between Surfaces of Specified Chemical Nature

Nathan W. Moore, Peter J. Feibelman, Gary S. Grest, Jack E. Houston

Prepared by
Sandia National Laboratories
Albuquerque, New Mexico 87185 and Livermore, California 94550

Sandia National Laboratories is a multi-program laboratory managed and operated by Sandia Corporation, a wholly owned subsidiary of Lockheed Martin Corporation, for the U.S. Department of Energy's National Nuclear Security Administration under contract DE-AC04-94AL85000

Approved for public release; further dissemination unlimited.

Issued by Sandia National Laboratories, operated for the United States Department of Energy by Sandia Corporation.

**NOTICE:** This report was prepared as an account of work sponsored by an agency of the United States Government. Neither the United States Government, nor any agency thereof, nor any of their employees, nor any of their contractors, subcontractors, or their employees, make any warranty, express or implied, or assume any legal liability or responsibility for the accuracy, completeness, or usefulness of any information, apparatus, product, or process disclosed, or represent that its use would not infringe privately owned rights. Reference herein to any specific commercial product, process, or service by trade name, trademark, manufacturer, or otherwise, does not necessarily constitute or imply its endorsement, recommendation, or favoring by the United States Government, any agency thereof, or any of their contractors or subcontractors. The views and opinions expressed herein do not necessarily state or reflect those of the United States Government, any agency thereof, or any of their contractors.

Printed in the United States of America. This report has been reproduced directly from the best available copy.

Available to DOE and DOE contractors from

U.S. Department of Energy
Office of Scientific and Technical Information
P.O. Box 62
Oak Ridge, TN 37831

Telephone: (865) 576-8401
Facsimile: (865) 576-5728
E-Mail: reports@adonis.osti.gov
Online ordering: http://www.osti.gov/bridge

Available to the public from

U.S. Department of Commerce
National Technical Information Service
5285 Port Royal Rd.
Springfield, VA 22161

Telephone: (800) 553-6847
Facsimile: (703) 605-6900
E-Mail: orders@ntis.fedworld.gov
Online order: http://www.ntis.gov/help/ordermethods.asp?loc=7-4-0#online

SAND2010-6498
Unlimited Release
Printed September 2010

# Studies of the Viscoelastic Properties of Water Confined Between Surfaces of Specified Chemical Nature

Nathan W. Moore, Gary S. Grest, and Jack E. Houston

Surface and Interface Sciences Department

Peter Feibelman

Energy Sciences Department

Sandia National Laboratories
P.O. Box 5800
Albuquerque, New Mexico 87185-MS1415

**Abstract**

This report summarizes the work completed under the Laboratory Directed Research and Development (LDRD) project 10-0973 of the same title. Understanding the molecular origin of the no-slip boundary condition remains vitally important for understanding molecular transport in biological, environmental and energy-related processes, with broad technological implications. Moreover, the viscoelastic properties of fluids in nanoconfinement or near surfaces are not well-understood. We have critically reviewed progress in this area, evaluated key experimental and theoretical methods, and made unique and important discoveries addressing these and related scientific questions. Thematically, the discoveries include insight into the orientation of water molecules on metal surfaces, the premelting of ice, the nucleation of water and alcohol vapors between surface asperities and the lubricity of these molecules when confined inside nanopores, the influence of water nucleation on adhesion to salts and silicates, and the growth and superplasticity of NaCl nanowires.

# CONTENTS

# 1. INTRODUCTION

## 1.1 Motivation and Approach

One of the original motivations was neatly summarized in a public statement made about this LDRD project by the trade journal, *Tribology and Lubrication Technology Magazine*:

> "Increasing demand for better quality water has spurred research efforts to develop more efficient desalination technologies" [1].

This statement asserts the importance of Sandia's work to improve desalination and other energy-related technologies involving solid-liquid interactions through coordinated fundamental research and engineering. Equally sought is to provide a better molecular understanding of the solid-liquid physics and chemistry relevant to materials in biology, geology, and atmospheric science to improve the efficiency of electrochemical energy storage and transformation, the prediction of weather and climate change, the surety of underground sequestration of carbon and radiological materials, and to improve the efficacy of molecular sensing technologies involving biological materials, for examples.

This project specifically aimed to understand the structure and fluidity of nanoconfined water through coordinated experimental and theoretical studies of water confined between surfaces of a specified chemical nature. As a whole, the interactions of water with solid surfaces are poorly understood at the molecular scale [2-5]. This lack of knowledge has created much confusion and debate across the disciplines over even basic ideas such as the origin of the no-slip boundary condition used every day to engineer hydrodynamic systems. For another example, some cite the exceptional viscosity of water near hydrophilic moieties decorating proteins as a possible explanation for the slower than expected transport of ions across cell membranes and for the slow leak rate of cell membranes that have been punctured [6], while others believe that the latter view is wholly unfounded [7]. Another example is a series of experiments carried out at Sandia using an Interfacial Force Microscope (IFM) in which the researchers concluded that water confined between various hydrophilic surfaces separated by only a few nanometers had a viscosity over one million times that of bulk water [8-10]. Such results excite controversy in part because the experimental and theoretical tools that are capable of ascertaining the structure and fluidity of nanoconfined water are still in their infancy.

To show the breadth of this controversy, Figure 1 shows the distribution of viscosity values measured for nanoconfined fluids reported in the literature. These values were obtained using a variety of techniques (experimental and theoretical), fluids, and confining surface chemistries, although the majority involved water between hydrophilic surfaces sheared with a scanning probe-based tool, such as AFM. Different techniques applied to this problem have involved not only differences in experiment variables, such as shear rate, the confining geometry, and the surface chemistries, but also differences in assumptions made in analyzing the data. Several key details behind these values are listed in Table 1 (see section 2.4.7 Viscosity of Molecularly-Thin Hydration Layers). Rather, the point here is the breadth of the results. The reported viscosity values range over 10 orders of magnitude even for water, and differ somewhat by technique,

with measurements by IFM giving some of the highest viscosity values and MD simulations giving some of the lowest values (Table 1).

Resolving this discrepancy is an important goal of this project. Indeed, the thickness of the interfacial water layer wherein aberrant viscoelastic properties have been purported to exist has most frequently been ≤1 nm [11]. Experimental methods for accurately probing viscoelastic properties over this length scale, while having produced many provocative results, are still in their infancy [12]. At the same time, the structure of a single layer of water molecules on a crystalline surface at low temperature is arguably one of the simplest physical situations one should consider to understand this larger problem, yet with this aim, contemporary computational methods have succeeded in reproducing experimental data in only a handful of situations [13].

Explanations for the origin of the enhanced viscosity values have been equally varied. Thus, much of our effort has been devoted to organizing the scientific literature by publishing reviews and perspectives (see Section 2). Those reviews will serve this report in lieu of a more extensive introduction to the science at hand. A number of important theoretical and experimental discoveries have been made and are summarized below (see also Sections 3 and 4). Uncertainty in the investigative techniques has motivated our extensive effort to characterize some of the methods, both theoretical and experimental, that are key to progress in this field (see Section 3.2 and Section 5).

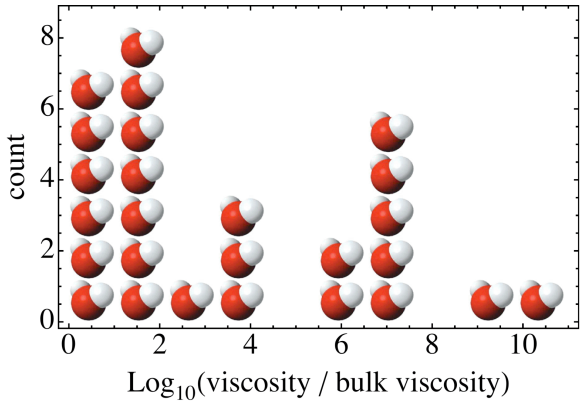


**Figure 1. Distribution of viscosity values reported in the literature for interfacial water and other confined fluids, relative to the bulk values (data and references in Table 1).**

## 1.2 Key Accomplishments

- Discovered superplasticity in salt nanowires [14], attracting media attention from the New York Times [15], National Public Radio [16], New Scientist [17], Chemistry World News [18], Science News [19], ACS News [20], Journal of Chemical Education [21], Tribology and Lubrication Technology Magazine [1].
- Published leading reviews and commentaries on interfacial water (Physics Today [13], Nature Materials [22], Faraday Discussions [23], and Progress in Surface Science [24]).
- Characterized the nucleation of water and alcohol vapors and fluids and their lubricity when confined inside nanopores [25-27].
- Developed a model for the orientation and arrangement of water molecules on Pt(111) at low temperatures [13].
- Measured the thickness and viscosity of the liquid-like layer on ice [28].
- Characterized the influence of water nucleation on adhesion to salts and silicates [26, 29].
- Evaluated methods for measuring the viscoelastic properties of nanometric fluid films, particularly those involving IFM (see Section 5).

## 1.3 Publications during the Project Period


- Feibelman, P.J., “The first wetting layer on a solid,” Physics Today, 2010, 63(2), 34–39.
- Feibelman, P.J., “Surface Water: Pentagonal ice in chains,” Nature Materials, 2009, 8(5), 372–373.
- Feibelman, P.J., " Water – From Interfaces to the Bulk. Concluding Remarks," Faraday Discussions, 2009, 141, 467–475.
- Feibelman, P.J., "Lattice match in density functional calculations: ice Ih vs. -AgI," Phys. Chem. Chem. Phys., 2008, 10, 4688–4691.
- Goertz, M.P. and N.W. Moore, “Mechanics of Soft Interfaces Studied with Displacement-Controlled Scanning Probe Microscopy,” Progress in Surface Science, submitted.
- Goertz, M.P., X.-Y. Zhu, and J.E. Houston, "Exploring the Liquid-like Layer on the Ice Surface," Langmuir, 2009, 25(12), 6905–6908.
- Lorenz, C.D., Michael Chandross, and Gary S. Grest, “Large Scale Molecular Dynamics Simulations of Vapor Phase Lubrication for MEMS," J. Adhesion Sci. Technol., 2010, in press.

- Lorenz, C.D., J.M.D. Lane, M. Chandross, M.J. Stevens, G.S. Grest, “Molecular Dynamics Simulations of Water Confined between Matched Pairs of Hydrophobic and Hydrophilic Self-Assembled Monolayers,” Langmuir, 2009, 25(8), 4535-4542.

- Moore, N.W., J. Juo, J.Y. Huang, S.X. Mao, and J.E. Houston, "Superplastic Nanowires Pulled from the Surface of Common Salt," Nano Letters, 2009, 9(6), 2295–2299.

- Moore, N.W., J.E. Houston, “The Pull-Off Force and the Work of Adhesion: New Challenges at the Nanoscale,” J. Adhesion Sci. Technol., 2010, in press.

- Moore, N.W., “Contact Electrification through Dewetting of a Nanoscale Meniscus between Oxide Surfaces,” in preparation.

- Nie, S., P.J., Feibelman, N.C. Bartelt, and K. Thurmer, “Pentagons and Heptagons in the First Water Layer on Pt(111),” Physical Review Letters, 2010, 105(2): 026102.


## 1.4 Acknowledgements


We thank the LDRD Program at Sandia National Laboratories for supporting this work. Certain portions of this work benefited from partial supported from other agencies and are acknowledged at the end of respective chapters. We are also grateful for our many collaborators who are acknowledged therein.

# 2. PERSPECTIVES & REVIEWS

## 2.1 The First Wetting Layer on a Solid

The following was published under the same title; see: P.J. Feibelman, *Physics Today*, 63(2): 34-39 (2010).

### *2.1.1 Abstract*

For decades researchers imagined that hydrogen bonding imposes a hexagonal, icelike arrangement on the first water molecules on a solid. Recent theory and experiments argue for a richer view.

### *2.1.2 Introduction*

Water is everywhere, the stuff of life, sculptor of the natural environment, helper and headache in a wide range of technologies. The first layer of water molecules at a surface is the structural template that guides the growth of ice, embodies the boundary condition for water transport, and mediates aqueous interfacial chemistry. It thus determines if rain will fall, how fast pollutants migrate in rock and soil, and governs corrosion, catalysis, and countless other processes.

This article is a report on recent efforts to understand water on surfaces that, by virtue of a stronger affinity for water than water has for itself, support a two-dimensional wetting layer. Such surfaces are said to wet completely [30].

The interaction of waxy or oily (hydrophobic) surfaces with adjacent water is weakly attractive at best. Thus, to a first approximation, water on hydrophobic surfaces is water in equilibrium with its vapor, a problem whose narrow range of outcomes is governed by surface topography and dielectric behavior—that is, macroscopic considerations. At complete-wetting surfaces, conversely, the water molecules' arrangements, dynamical behavior, and roles in interfacial chemistry are largely contingent on atomic-scale surface structure and composition. And understanding them presents serious challenges to the experimental and theoretical state of the art.

Spectroscopy, high-resolution imaging, and the scattering of x rays or electrons can reveal important structural clues, provided the experiments don't alter the typically delicate sample. But filling in the atomic-level details theoretically is fraught with difficulty, attributable to force laws of questionable accuracy (whether semi empirical or ab initio), energy surfaces with many relative minima and many barriers, and the quantum nature of the proton—that is, the effects of proton zero-point motion and tunneling.

Still, deciphering the details was not expected to be so challenging, at least not for water on the hexagonal surface of a precious metal. For some two decades researchers imagined that in that ideal case, water molecules would initially arrange themselves as one hexagonal layer of the naturally occurring ice crystal, "ice Ih," which conserves hydrogen bonds by straining to fit the metal lattice constant. But 21st century work on water adsorption, both theoretical and

experimental, has consistently called into question whether an icelike wetting layer *ever* exists. That is the unifying theme of what follows.

Even the most basic question about complete wetting—why a particular surface is more attractive to water than water is to itself—can be hard to answer. Is the observation of a 2D water layer the result of kinetic hindrance—that is, a dewetting barrier—or of thermodynamics? If kinetics is at stake, then total energy minimization is a structural tool of questionable value, whether or not a reliable force law is available. Is the formation of hydrogen bonds between a water layer and a solid sufficient to make complete wetting thermodynamically favorable? When is surface chemistry—for example, the transfer of hydrogen atoms from water molecules to surface sites or surface impurities—at the heart of wetting?

Learning the structure of the first layer of water molecules on a solid is not an end in itself but preliminary to understanding multilayers. With that in mind, two novel studies give one pause [31, 32]. The first water layer on the close-packed surface of platinum, the studies agree, is hydrophobic to succeeding ones. That poses unexpected questions for ice epitaxy and for water transport. For example, on what wetting surfaces should epitaxy occur? And is a "no slip" boundary condition appropriate for transport along the surface? The same questions arise for water on kaolinite, a clay thought to seed ice nucleation in clouds. The first water layer on that oxide has been predicted to grow two-dimensionally—but once again in a way that seems to render the surface hydrophobic to subsequent water [33].

### *2.1.3 Water on Metals*

But for the occasional nugget, metals are not part of our daily experience of nature. More stable materials such as oxides, sulfides, and salts are. So why have most molecular-level studies of wetting referred to metals nonetheless—and at low temperatures in ultrahigh vacuum (UHV)? It's not that metals conduct electrons or that applications like corrosion, fuel cells, and electrocatalysis are any more important than rainfall, erosion, or transport of toxic materials in soil. Rather, metals represent the simplest test bed for refining understanding.

We know how to prepare and clean nearly perfect, single-crystal (particularly, precious) metal surfaces in UHV, and a wide variety of surface science techniques, many of which *do* require electrical conductivity, are available to study them—with and without water present. Years of such studies have produced a large database [4, 34]. About a dozen wetting systems, including water on nine different metal surfaces, are known from diffraction experiments to be ordered and thus more susceptible to analysis [4]. Scanning tunneling microscopy (STM) images of adsorbed water are available for several metal-crystal faces, and some cases—for example, a recent study of water on the (110) surface of copper[7]—allow conclusions to be drawn from theoretical image simulation.

There are also telling spectroscopic experiments—for example, x-ray photoelectron spectroscopy, which easily distinguishes dissociative from nondissociative adsorption, and IR absorption, which in addition provides information on bond orientation.

### *2.1.4 The Classic Bilayer*

Given that the naturally occurring ice crystal is hexagonal with a lattice constant of 4.5 Å, close to √3 times the interatomic spacings of group VIII metals (4.69 Å for ruthenium and iridium, 4.66 Å for rhodium, 4.76 Å for palladium, and 4.80 Å for platinum), one might expect ice crystals to grow epitaxially on their hexagonal faces, starting with the very first adsorbed layer of water molecules. In this classic "puckered bilayer" model of the first wetting layer on a close-packed, precious metal surface at low temperatures (see Figure 2), every other $H_2O$ molecule either lies almost flat, binding to the substrate through its oxygen atom, or, lying about 1 Å higher, contributes one O–H bond to the bilayer's H-bond network and dangles the other O–H bond into the vacuum.

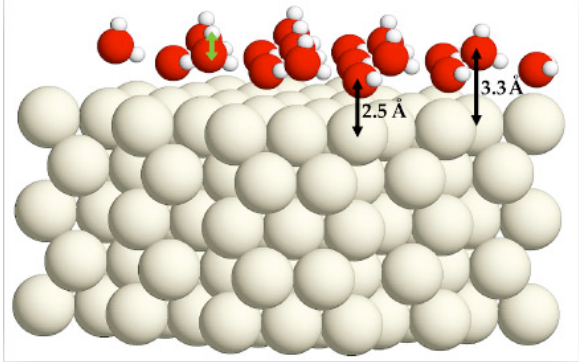


**Figure 2. The classic hexagonal bilayer on a five-layer ruthenium slab. Large, medium, and small balls represent Ru, oxy- gen, and hydrogen atoms. The O atoms of the flat-lying water molecules each lie 2.5 Å directly above a Ru atom. The O atoms of the remaining water molecules lie 0.8 Å higher. The green arrow indicates a dangling O–H bond, which largely consumes the power of the oxygen 2pz orbital to form a bond. (Adapted from ref. [35].)**

Though it has been a paradigm for decades, definitive evidence for the puckered bilayer remains to be uncovered. Indeed, much recent progress in understanding wetting has been the result of challenging the classic model. One contentious question has been whether wetting-layer water molecules remain intact.

### *2.1.5 Are the Water Molecules Intact?*

In their 1987 review, Patricia Thiel and Theodore Madey suggested that dissociative adsorption of an $H_2O$ molecule as OH and H fragments is unfavorable on all the precious metals—with ruthenium and osmium being borderline cases [34]. Seven years later Georg Held and Dietrich Menzel published a low-energy electron-diffraction study of a periodic $D_2O$ layer on the hexagonal face of Ru, yielding what was, for years, the *only* quantitative structural information for water on a surface. Importantly, Held and Menzel found that the heavy-water layer's O atoms were virtually coplanar, confounding expectations based on the classic bilayer.

To explain coplanarity, a new idea was needed. After eight more years, a successful one emerged [35]: In the classic bilayer, there is no driving force to move an upper O atom toward the surface,

because an upper O atom's power to bind to the metal is consumed in forming its dangling O–D bond. Were that bond broken, the upper O atom would move down.

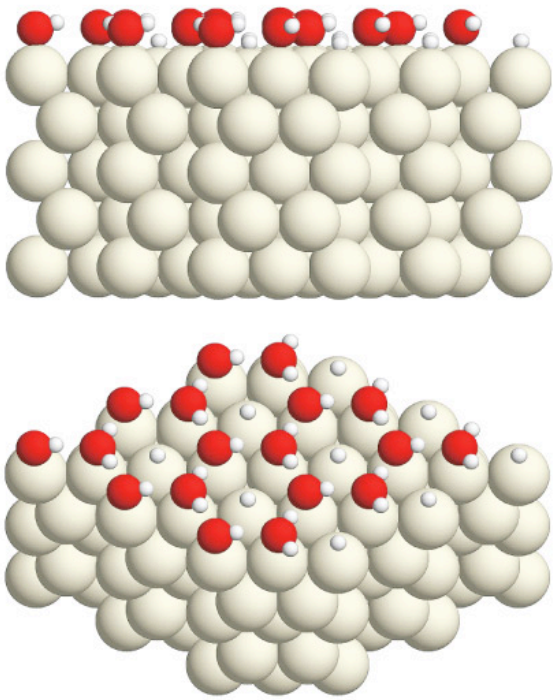

**Figure 3. A half-dissociated layer of water molecules on the close-packed surface of ruthenium, seen from side and oblique perspectives. The upper panel shows that the oxygen atoms (red) are almost coplanar. The lower panel shows that there are just enough metal-atom surface sites to accommodate the hydrogen atoms (small, white) dissociated from half the water molecules. Strong bonds between OH and Ru have pulled all O atoms closer to the metal than they were in the arrangement pictured in Figure 2. The O atoms of the OH fragments here are just 2.09 Å above the Ru atoms directly below them; the water-molecule O atoms lie 0.07 Å higher. (Adapted from ref. [35].)**

First-principles calculations supported that elementary chemical notion. Optimization of a water adlayer, with dangling O–D bonds replaced by Ru–D bonds, yielded a nearly coplanar O structure (see Figure 3), bound at least 0.2 eV per $D_2O$ molecule better than the paradigmatic bilayer. Zero-point motion, which favors breaking stiff O–D bonds, adds to the binding of the partly dissociated water layer and makes it thermodynamically favorable compared with a nonwetting arrangement of 3D ice droplets on the 100- to 120-K surface.

Thermodynamics notwithstanding, the dissociated-structure motif elicited much debate over a question that needs an answer in every high-vacuum, low-temperature experiment: Does an observed structure represent thermal equilibrium or kinetic hindrance? For heavy water on Ru, little doubt was expressed that the dissociated structure represents equilibrium. The worry was that the dissociation observed in the Held–Menzel electron-beam diffraction experiment could be an artifact of electron irradiation. Without irradiation, would dissociation have occurred or would a metastable wetting layer comprising intact water molecules have formed?

Realizing that all H bonds should be parallel to the metal surface in a structure with coplanar O atoms, Andrew Hodgson and coworkers offered a persuasive answer [36]. Using IR absorption spectroscopy to observe H-bond directions, they proved that a metastable, intact $H_2O$ layer forms below 150 K on Ru; at warmer temperatures dissociation occurs. The key is that dissociation occurs at a lower temperature than evaporation. If $H_2O$ is replaced by $D_2O$, both processes occur near 160 K. And absent a background pressure that compensates evaporation with the deposition of $D_2O$ molecules, a thermally dissociated heavy-water layer does not form. The electron beam, accordingly, was responsible for dissociation in the Held–Menzel, heavy-water experiment.

Recent STM images from Miquel Salmeron's group at Lawrence Berkeley National Laboratory confirm the existence of a low-temperature layer of intact water molecules. Thus, besides spectroscopy, the simulation of low-temperature, atomic-resolution images of adsorbed water is one way to approach the question, How can we make use of our favorite theoretical approaches when the energy differences they yield are indistinguishable from systematic error?

### *2.1.6 Density Functional Theory*

An elegant and ultimately Nobel Prize–winning theorem proven by Pierre Hohenberg and Walter Kohn in 1964 states that the energy of a condensed system is a functional of its electron density n(r) and that the correct energy density is the one that minimizes the system's total energy. The theorem means that, in principle, one can find the optimal arrangement of atoms in a solid by iterative solution of a nonlinear differential equation in three Cartesian coordinates—something of a saving compared with a Schrödinger equation. Nonetheless, the faithfulness of density-functional-theory results to nature depends on how well one approximates the a priori unknown functional. Certain aspects—for example, its asymptotic properties at high electron density and a variety of sum rules it must satisfy—are understood. Still, there is no systematic way to improve a functional, and newer versions are therefore judged purely according to how accurately they predict the structures and formation energies of suites of systems assumed to be representative. Hydrogen-bonded materials ought to present a relatively light challenge to functionals because the hydrogen bond is electrostatic and because we know Coulomb's law. In practice, the issue is to describe polarization accurately enough in relatively weakly bonded systems. A functional that does this well for water and also accurately describes metals and oxides remains to be developed.

Density functional theory is today's method of choice for first-principles estimates of the structural energetics of extended condensed-matter systems. Of DFT's many successes, however, most involve materials governed by strong chemical forces. When one compares candidates for their optimal atomic arrangements, energy differences are correspondingly large, and the unavoidably approximate functional (see box 2) produces errors of small consequence. With H bonds an order of magnitude weaker, however, the reliability of DFT energies in distinguishing more favorable wetting structures from less is unproven. Indeed, it raises the question of whether ab initio theoretical studies of wetting are timely at all.

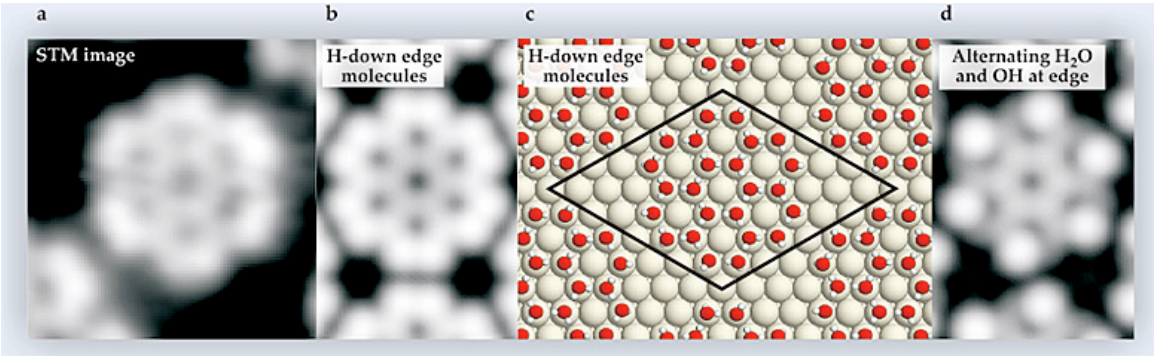


**Figure 4. (a) A water "rosette" adsorbed on the close-packed surface of palladium, as seen by scanning tunneling microscopy (STM). (b) An image simulation based on the density-functional-theory optimized model structure (c), in which one of the hydrogen atoms of each water molecule on the rosette periphery lies below its oxygen atom. (d) An image simulation based on the assumption that alternate peripheral water molecules have lost an H atom. Comparison to the STM image makes clear that the "H-down" model is the better representation of experiment. The black parallelogram delimits the unit cell used in the periodic DFT calculation. (Adapted from ref. [37].)**

In two recent studies, the problem was bypassed by comparing STM image simulations of DFT optimal structures with actual STM data—instead of relying on calculated energies. The first study [37] was an attempt to understand the appearance of "lace" and "rosette" islands of water on Pd(111). Both structures appear to comprise flat-lying water molecules in their interiors and molecules in another configuration, initially unknown, at their edges. DFT calculations for a rosette island implied only a small preference for edge molecules with O–H bonds dangling downward, toward the metal, versus edge molecules whose dangling H atoms are dissociated and bound to water-free regions of the Pd surface. Image simulation, nevertheless, left little doubt that the first picture is the correct one, as shown in Figure 4.

A second example of bypassing energy calculations in favor of STM simulation concerns 1D water islands observed on Cu(110) [38]. In the classic bilayer picture, a 1D island cannot be a low-energy structure, because of the cost of the many broken hydrogen bonds at its periphery and because the regular hexagons of the bilayer are a poor match to the long, narrow hexagons of the Cu surface. Javier Carrasco and his colleagues resolved the conflict last year with an unconventional idea—that the molecules of the 1D islands adopt a side-sharing pentagonal arrangement [39]. That idea, they showed, accounts for the STM images and the measured IR absorption spectrum. They explained that the pentagonal structure has most of its O atoms in what DFT implies are their preferred sites—coordinated to one metal atom—with reasonable O–O bond lengths and angle distortions. So, it allows for strong O–metal bonds without overly straining the hydrogen-bonding network.

Notwithstanding that success, and evoking a continuing issue for theorists, the calculations did not explain on the basis of energies, why 1D islands grow on Cu(110) in preference to 3D ice mounds. Just as for water molecules on low-temperature Pd(111), image simulation based on a DFT-optimized structure was needed to interpret the STM data because systematic error makes today's DFT energies unreliable in wetting problems.

### 2.1.7 Water on Silver Iodide

Worrisome examples are not limited to water on metals. In 1947 Bernard Vonnegut proposed using fine particles of silver iodide to nucleate ice in clouds, a necessary precursor to rainfall [40]. The idea was based on a survey of crystal lattice parameters, which revealed that the lattice constants of hexagonal ice Ih and $\beta$-AgI agree to about 1.6% at 0 °C. Admitting an AgI "smoke" to a humid container in the lab was then found to result in rapid formation of ice crystals on the walls. Subsequently, Irving Langmuir of the General Electric Co analyzed experiments conducted in New Mexico to learn if seeding with AgI could make southwest monsoon clouds drop rain. Establishing a causal relationship has not been possible—still, floods and downwind droughts following cloud seeding have been a healthy source of income to legal practitioners ever since.

The scientific question of interest is whether epitaxial match really is the key to ice nucleation efficiency on AgI. Over the decades, most researchers have dismissed that notion, although studies of ice formation in biological systems make the answer less clear. DFT calculations ought to help resolve the matter, but only if the approximate density functional that is used reproduces the epitaxial match found in nature. Otherwise, the functional imposes an unphysical strain on the nucleating ice structure. For water on AgI, I have found mismatches ranging from 4.2% to 7.9%, depending on which of eight semilocal functionals are used. Once again, it appears today's approximate functionals are not up to the task.

### 2.1.8 Water Multilayers

As noted earlier, knowing the structure of the first layer of water molecules on a surface is not an end in itself but needed for a general understanding of water's behavior in contact with a material. In many cases, first-principles calculations imply that instead of being ready to donate H atoms to form H bonds with a second layer of water molecules, the first water layer on a hydrophilic surface locates its H atoms either in that layer or between it and the solid. This suggests that the first wetting layer has a propensity to make the surface hydrophobic, a propensity most pronounced at low temperatures.

Two novel techniques have confirmed that theoretical result for water on the close-packed surface of Pt metal. Gregory Kimmel and colleagues approached the problem of multilayer morphology by studying the evaporation of krypton atoms deposited on the water layers [31]. The evaporation onset temperature is higher for Kr atoms that lie closer to the metal, and thus one can determine the surface area covered by a given number of water layers by measuring the number of desorbing Kr atoms in the corresponding thermal peak. In that way, Kimmel's group showed that although the first water layer on Pt wets the metal completely, additional water grows in 3D mounds, which leave parts of the first layer exposed even at rather high coverages.

Konrad Thürmer and Norman Bartelt drew the same conclusion in 2008 from an STM study [32]. Prior to their work, researchers had not imagined that enough electron current would tunnel through an insulating water layer to make imaging possible. Serendipitously, Thürmer discovered that at high bias (around 6V), ample current tunnels nondestructively from the Pt(111) crystal face through adsorbed water multilayers. This discovery allowed them to observe

the dewetting of water layers grown on top of the first to form 3D mounds. That amounted to direct evidence that the final configuration, expressing the hydrophobicity of the first layer, reflects thermodynamics and not kinetic hindrance.

### *2.1.9 Water Multilayers on Oxides*

To learn why minute particles of kaolinite nucleate ice crystals efficiently and thus seed clouds, a recent theoretical study extended from metals to oxides the notion of a first water layer hydrophobic to the second [33]. A first guess is that a good lattice match between the mineral and ice Ih is the key factor [40]. But the DFT results suggest that structural chemistry is more important.

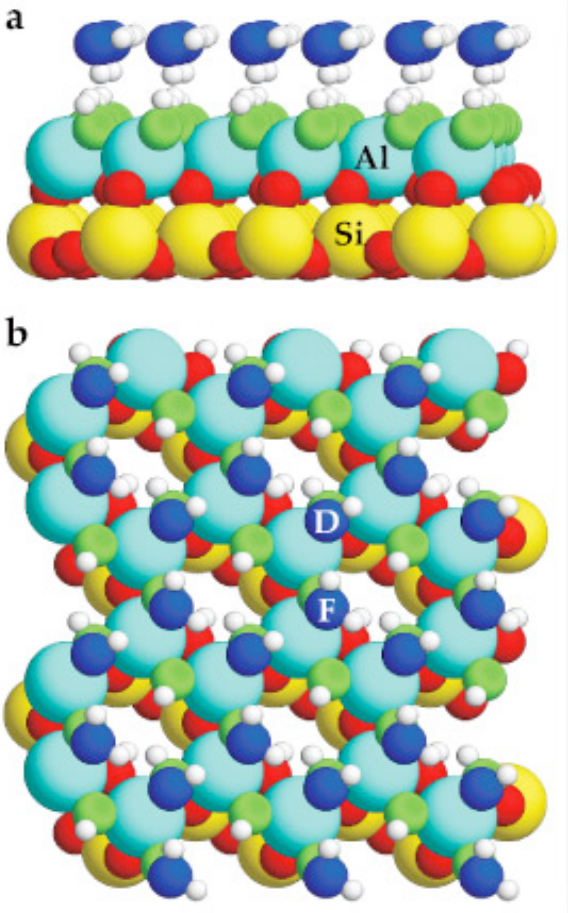


**Figure 5. Water on a clay. The positions and orientations of a simulated layer of water on a thin slab of the silicate mineral kaolinite ($Al_2Si_2O_5(OH)_4$) were calculated using density functional theory. Oxygen atoms of the water layer are shown in blue, and those that bridge aluminum atoms are green. The remaining O atoms are red. (a) In the side view, no H atoms (small and white) dangle into the vacuum above the water layer. (b) In the top view, water molecules either lie flat, as in the case labeled "F," or form a donor H bond to the solid, as in the case labeled "D" for "H- down." (Adapted from ref. [33].)**

Kaolinite is a stack of silica-alumina layers, with OH ligands hydrogen-bonding Al atoms of one layer to O atoms that bridge Si atoms of the next. Cleaving kaolinite thus exposes an alumina surface on which the OH ligands are available to form donor H bonds to water molecules and O atoms are also available as H-bond acceptors. That chemical environment and not the good lattice match, argue Xiaoliang Hu and Angelos Michaelides, is the basis of the hydrophilic behavior of kaolinite [33]. According to their calculations, the binding of deposited water is sufficiently strong that a 2D complete-wetting layer is thermodynamically favored. But the strong water–solid bond at zero temperature is achieved only by virtue of a molecular arrangement that leaves no OH bond dangling and thus available to bind a second water-molecule layer (see Figure 5). How water multilayers should grow on nominally hydrophilic kaolinite(001) is, accordingly, as unclear as it is on Pt(111). The boundary conditions these surfaces impose on water transport also need new understanding.

### *2.1.10 Transport of Confined Water*

That the structure of the first water layer on a material affects transport of adjacent water need not just be a matter of speculation. Direct measurements of resistance to shear should clarify not only how the structure and chemistry of confining surfaces affect the boundary conditions for flow but also the regime wherein continuum hydrodynamics—and specifically the concept of viscosity—is meaningful. They should tell the degree and nature of solute effects and whether incipient crystallization—the layering of water molecules—gives rise to oscillatory variations of friction with channel thickness. One day we will know the answers; for now, results conflict, sometimes spectacularly.

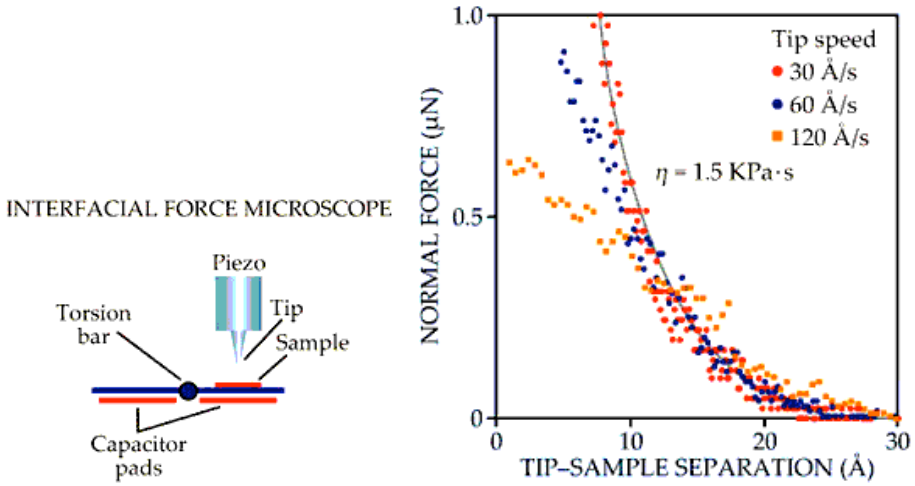


**Figure 6. The interfacial force microscope, shown schematically at left. The force between tip and sample is counterbalanced by delivery of charge to the capacitors, allowing a force measurement with no mechanical deflection. At right, data from an IFM experiment by Ryan Major and colleagues show the forces experienced by an OH-functionalized tungsten tip that approaches an OH-covered silica surface in water at different speeds. (Each plotted point is scaled by a factor of 30 Å/s divided by the tip speed.) Between 10 and 30 Å, the resistance of the water to being squeezed out of the tip–sample gap scales with speed, suggesting a viscous response. The gray curve is a prediction based on hydrodynamics at low Reynolds number. The viscosity η of water in the gap, derived by fitting the curve to the data, is some million times that of ordinary bulk water [41]. (Figure courtesy of Jack Houston.)**

The conflicts might involve inadequate surface characterization, but not a lack of appropriate instrumentation. For example, the interfacial force microscope (IFM), a cousin to the atomic force microscope (AFM), is designed to study adhesive and frictional forces in liquid or air between a probe tip and a flat sample [42]. The tip–sample forces are measured not by the bending of a cantilever spring but by observing how much charge must be delivered to appropriately positioned capacitors to counteract the force (see Figure 6). The design is advantageous in that the tip–sample spacing and approach speed are under the experimenter's control, even when strong adhesive forces would otherwise overcome the resistance to the bending of a soft spring or mica sheet and end the experiment with an abrupt "snap to contact."

The remarkable result of IFM studies of water confined to 1–2 nm between a tip and sample is that the measured force as a function of relative tip–sample speed implies a water viscosity roughly a million times that of water in bulk [10]. This result, obtained for a variety of hydrophilic tip and sample combinations and with the tip approaching the sample or oscillating parallel to it, is orders of magnitude larger than what has been found when water is confined between the hydrophilic mica sheets of a surface force balance [43]. (The SFB's design is discussed below.)

Locking water molecules into layers, as in a crystal, is a conceivable source of greatly enhanced shear resistance near a surface. But x-ray reflection measurements of water on hydrophilic oxide surfaces typically reveal only one or two well-defined water-molecule layers, largely within 0.5 nm of the interface [44]. Beyond that distance, layering should not affect forces much. And, indeed, neither the IFM nor the SFB shows evidence for oscillatory forces at tip–sample separations over a nanometer. That said, AFM measurements for water between a silica tip and a mica sample *do* show oscillations and a substantial enhancement to the viscosity at separations smaller than 2 nm [45].

### *2.1.11 Water on Mica*

Water on mica has been the subject of many transport studies that use either Jacob Israelachvili's surface force apparatus (SFA) or Jacob Klein's SFB [46]. The liquid is confined between two cylindrical mica sheets, with the cylinders at right angles. The distance between the sheets is measured interferometrically (in the SFA) or capacitively (in the SFB), and the force opposing their approach toward each other, or the sliding of one sheet relative to the other, by an arrangement of springs. Contrary to findings with the IFM, SFB results imply that confined water is not much more viscous than water in bulk. Neither technique, however, shows evidence for layering, even down to a fraction of a nanometer.

To understand how proximity to the mica surface affects the arrangement of water molecules, Salmeron and coworkers developed and applied a novel scanning probe technique; this (decade old) work is reviewed in reference [36]. Ordinary STM was not an option because muscovite mica is a very good insulator, and ordinary AFM would disturb the water layer too easily. To surmount these obstacles, they used the rather low resolution technique they dubbed scanning polarization force microscopy, in which an AFM tip retracted to a distance of a few hundred angstroms detects the presence of water by the degree to which an electric field affects the force the tip experiences. Using this tool, the LBNL group found that at 20–40% relative humidity and room temperature, water adsorbs as 2D crystals; that is, the water islands observed are faceted along the principal lattice directions of the underlying mica.

With the sense that crystallinity expresses underlying simplicity, several computational groups have hoped to account for the 2D crystal structure at the molecular level by using empirical force fields or DFT. But their efforts have been frustrated by several complexities. One is that surface potassium atoms, which bind mica's silica–alumina–silica layers to each other, are water soluble. Another is that the mica surface's Al atoms are, within certain rules, randomly located. Also, x-ray reflectivity measurements require that a model wetting layer have a certain fraction of water molecules lying low in the array of depressions intrinsic to the mica surface.

On the basis of a molecular dynamics simulation, Artur Meleshyn of the University of Hannover in Germany has proposed that the low-lying water molecules in surface holes are responsible for the observation of island facets aligned to the substrate and that K atoms rising out of their surface hollows to become fully solvated are what drive wetting energetically. One might hope this picture would stand the test of time. My own DFT optimization of a snapshot from the simulation, however, suggests that 3D mounds of water on mica are significantly better bound.

Does that result prove that the model wetting layer is missing a physically or chemically important feature? Given the level of systematic error in today's density functionals, one is hard put to say. Accordingly, water transport on mica is not yet a timely theory problem at the molecular scale.

### *2.1.12 Where We Stand*

Access to large, powerful computers and modern algorithms raises the appealing prospect that simulations will reveal how the first water layer guides epitaxy and governs transport and chemistry at water–solid interfaces. To achieve that level of understanding, theorists require a density functional that accounts reliably for the energy differences among hydrogen-bonded structures. Accuracy of DFT binding energies to 10 meV or better, per H bond, is needed. Until such is available, progress in deriving insight from data will remain fitful. Most needed from experiment is quantitative, atomic-scale information. Scanning probe images have been helpful in devising model wetting structures. Atomic coordinates from diffraction data, for example, would be better. They would constrain and thus help to improve the reliability of theoretical models.

Still, 21st-century research into the nature of the first wetting layer on a solid has borne important fruit. On the evidence, we have learned that adsorbed water can organize nonhexagonally. We have discarded the ideas that H bonds around a surface O atom must be arranged tetrahedrally and that water molecules must adsorb intact on precious metals. As a result, we have had to refine our considerations of what might be the molecular basis of the "no-slip" boundary condition for water transport and of how an ice crystal nucleates. The recent confrontation of theory and experiment has led to an understanding of wetting structures that is far richer than the imagined ideal, icelike bilayers—no longer a paradigm, at best a straw man.

### *2.1.13 Acknowledgements*

My many discussions with Norman C. Bartelt are gratefully acknowledged.

## 2.2 Surface Water: Pentagonal Ice in Chains

The following was published under the same title; see: P.J. Feibelman, *Nature Materials* **8**, 372–373 (2009)

### *2.2.1 Abstract*

One-dimensional islands that grow during ice nucleation at low temperatures on a copper(110) surface are identified as chains of water-molecule pentagons. This unexpected molecular

arrangement optimizes oxygen-atom proximity to preferred bonding sites on the metal, while minimizing strain in the hydrogen-bond network.

### *2.2.2 Discussion*

The role of water in many important natural and technological processes makes understanding the interactions between water and materials a high-priority research endeavor. The first water layer on a solid is of particular interest because it acts as a structural template for the layers that follow, it sets the boundary conditions for water transport, and it governs aqueous surface chemistry. A telling measure of the community's interest in this area is the list of 1,165 references in M. A. Henderson's 2002 review [4].

Since then activity in the field has intensified; nevertheless, surprise continues to mark the search for motifs that favor strong bonding between water and materials. The observation of one-dimensional water islands on a Cu(110) surface [47] is an excellent example, confounding the conventional expectation that the first water layer on a metal will be a hexagonal array of water molecules resembling a single layer of the naturally occurring ice crystal (known as ice *Ih*). How can one-dimensional islands be stable, and how can the low-energy arrangement of water molecules sustain broken hydrogen bonds? These are the concerns that Michaelides and colleagues have addressed and resolved on page 427 of this issue [22]: first by amassing evidence that the one-dimensional islands comprise lines of edge-sharing, water-molecule pentagons (Figure 7) — not the hexagons that characterize bulk ice; and then by explaining the preference for pentagonal rings in terms of an alternative bonding principle to perfect hydrogen bonding [38]. The authors reason that water molecules prefer structures where O atoms lie nearly directly above metal atoms and structures that do not involve high strain. On the anisotropic Cu(110) surface, these two principles conflict, and the compromise between them excludes the possibility of the conventional ice-like, perfectly hydrogen-bonded hexagonal molecular arrangement. The surface Cu atoms are not arranged in regular hexagons. Situating O atoms directly above them can therefore only produce highly distorted high-energy water-molecule hexagons. By contrast, the pentagonal arrangement of intact molecules, which, happily, accounts for both scanning tunneling microscopy images and the measured infrared absorption spectrum, has most of its O atoms in the desirable 'atop' metal atom sites, and more reasonable O–O bond lengths and angle distortions. Accordingly, it allows for strong O–metal bonds without overly raising the internal energy of the water-molecule rings. This compromise overcompensates for the broken hydrogen bonds at the island edges.

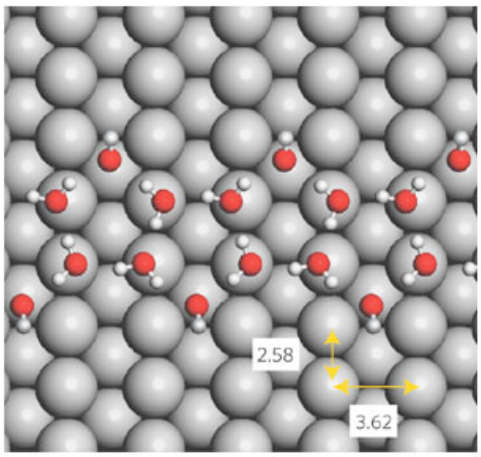


**Figure 7. Colored spheres represent different atoms: copper (grey), oxygen (red) and hydrogen (white). Interatomic spacings are given in ångströms.**

This logic exposes a long-standing piece of contradictory reasoning. Molecular layers of ice are often observed to wet (that is, lie flat on) surfaces. Yet thermodynamically this is only possible if water–surface interactions are as, or more, attractive than those between water molecules — otherwise, three-dimensional ice crystals will form. Thus, the common assumption that hydrogen-bond interactions dominate the structure of ice films is inconsistent with the existence of the films in the first place: the dominance of hydrogen-bond interactions is virtually the definition of water on a hydrophobic surface.

Michaelides and co-workers' results also exemplify another important lesson — given the current state-of-the-art in density functional theory, relying solely on computed energies is not an adequate way to predict arrangements of adsorbed water molecules. The collaboration finds their pentagonal island structures to be better bound than plausible hexagonal arrangements, and by a healthy 70 meV per molecule. Moreover, they support the inference that the pentagonal arrangements represent a thermodynamic minimum energy structure with evidence (from infrared spectroscopy) that the same structure can be arrived at both by direct adsorption and annealing, and by adsorbing water multilayers and evaporating down to the single layer.

Still, the computed binding energy of the optimal islands is some 50 meV less than that of water molecules in bulk ice *Ih*, at the same level of approximation [22]. Taking this binding deficit at face value, one should conclude that three-dimensional ice mounds on the surface represent the minimum energy structure, not flat, linear islands. Thus, until a more accurate version of density functional theory becomes available, reliance on computed energies may provide a less satisfactory interpretation of data than direct comparison with the data themselves.

Michaelides and colleagues tacitly adopt this approach. Simulations based on their pentagonal arrangement of water molecules provide an excellent account of the scanning tunneling microscopy images. Computed and experimental infrared spectra are also in close agreement. A similar approach was successful earlier, in deciphering the arrangement of water islands on a Pd(111) surface [37], another water-adsorption system for which comparison of calculated binding energies was inconclusive.

As is to be expected, Michaelides and co-workers' exciting new discovery suggests avenues for further study. The most important would be a comparison of the energies of two-dimensional, as opposed to linear islands on a Cu(110) surface; specifically, is the formation of two-dimensional islands disfavored by the impossibility of covering a surface with pentagons?

## 2.3 Water – From Interfaces to the Bulk

The following was published under the same title as concluding remarks in *Faraday Discuss.*, 2009, 141, 467-475, written by P.J. Feibelman

### *2.3.1 Discussion*

The organizers of Water – from Interfaces to the Bulk optimistically drew two disparate realms of water-related research, at very different stages of development, into a joint discussion. One area was biophysical—with its focus on how water behaves in the cellular environment. The other was the surface science of water, including the nature of the solid/water interface, and of that between liquid and vapor. This breadth of interests often made participation in the discussion challenging.

It is hard to disagree with the often expressed, by now virtually boiler-plate, notions that water is among the most complex of materials, and that because it is everywhere it is also among the most important. The joint discussion made clear that deciding how to deal with the complexity, *i.e.* which water research problems it makes sense to address in the here and now, is worthy of serious consideration. In particular, a frontal attack on the complexity may not be the most productive approach.

The $40^{+}$-year history of surface science [48], my area of expertise, provides a good example of patient development of technique before any serious attempt to fulfill more or less extravagant early promises. It speaks well both of careful problem selection by surface scientists and of the tolerant understanding of their funding agents.

In its first two decades, 1964–1984, surface science was largely about technique development. The primary goal was the ability to say with confidence that experiments done in two different apparatuses, or two different laboratories, referred to the same surface structure and composition. The main tools for this purpose were low-energy electron diffraction (LEED) and Auger electron spectroscopy (AES) and, far from attempting to apply them to real-world problems, surface scientists in this era were eager to study systems in which impurity levels were below detection limits and as many atoms as possible were in identical environments. In such ideal surface systems, experimental information content was understood to be minimal, a vital benefit when computer and algorithmic power were much less than today's. Interpreting data from, or making predictions concerning systems of numerous inequivalent atoms was simply not possible [49].

Even for ideal systems data reduction was a serious challenge, with the major obstacle that the experiments used to measure surface structure and composition derived their sensitivity from the strong interaction of probe and sample electrons. In the case of LEED, *e.g.* unlike X-ray structural analysis of bulk crystals, the first Born approximation cannot be used simply to invert

diffraction data and arrive at atomic positions. A lengthy period was therefore unavoidable, during which multiple-scattering analysis needed to be developed and proven reliable [50]. Fulfilling promises to speed up the invention of new catalysts was therefore not how surface scientists spent their days, even while they may have worried about what they would say to grant managers at renewal time.

It was discovered, early on, that surfaces can reconstruct, with Si(100)–2 × 1 [51] and Si(111)–7 × 7 [52] among the first non-bulk-like crystal faces contemplated. Thought was devoted to their nature, particularly that of Si(100)–2 × 1, because of both its technological importance and its not-overly-large unit cell. The 7 × 7 structure, though a tantalizing objective, was viewed by many as beyond technical capabilities, and left for another day, when new methods would and did, in fact, allow its structure to be deciphered (first by transmission electron microscopy [53], and later by scanning tunneling microscopy [54]).

Over the course of the first two decades of surface science, in summary, though far from loath to make promises on the important technological advances surface science would ultimately yield, surface scientists focused heavily on developing an alphabet soup of techniques, and on identifying benchmark systems where several techniques agreed on the surface atom arrangement.

The arrival of scanning tunneling microscopy (STM) [55], followed by another alphabet soup of complementary scanning probe techniques, changed everything. Once the STM existed it became possible to *image* the surface one was studying with atomic resolution, thus to appreciate how defective it might be and to see surface impurities. Scanning probe microscopies, largely, are what made real world surface studies timely.

The reason for these introductory remarks is not to set the stage for a review of the many phenomena surface scientists have successfully addressed since the mid-1980s, but to underline that in planning a research program, one needs to think not just about how to persuade granting officers and their referees that a particular project is important, and that manpower and equipment to complete it are at hand, but also about *timeliness*. A project becomes timely when technical advances make it relatively easy to realize. If deriving new insight will be too hard, it is likely that the project in question is premature. In that case, stepping back to the study of more idealized systems, or focusing on technique development in whatever the area of research, might be the best way to make progress.

Again harking back to the first two decades of surface science, practitioners were virtually blindfolded then, working with reciprocal space data from diffraction experiments, sensitive only to the likely-as-not-unrepresentative, ordered regions of a surface, and using measures of surface composition of good but still limited sensitivity. The Nobel-winning invention of the STM amounted to taking the blindfold off, and made studies of real-world systems timely. Projects that might have absorbed several man-years of working in the dark of the pre-STM era suddenly became straightforward.

From the theorist's perspective, it should be added that the continuing advance of computing (Moore's law [56]) and algorithmic power was also very significant. It allowed for a parallel computational effort to decipher the behavior of more real-world surface systems.

With this broad-brush history in mind, and a charter to offer a critical discussion of the presentations at Faraday Discussion 141, my view of the biophysical science discussed is that the efforts devoted to developing new or improving older techniques, and to attempting to extract information from the most ideal systems were of the highest interest. Thus the application of terahertz spectroscopy to protein solvation dynamics [57], NMR to water dynamics at proteins, peptides and in cells [58], and the reported studies of periodic purple membranes [59] appealed most to this surface scientist.

The very first discussion, revolving around the population of $H_3O^+$ as against $OH^-$ at the neat water surface was disturbing. Two experimental groups discussed plain evidence that the surface is negatively charged, by the presence of $OH^-$ ad-ions [60, 61]. In stark contrast, simulations conducted and discussed by plenary speaker P. Jungwirth [62] led to his conclusion that the same surface is positive, by virtue of the adsorption of $H_3O^+$. A contradiction like this is generally very valuable; one cannot fail to learn something by resolving it. Thus it was disappointing that neither side addressed a possible resolution.

Such was offered in the course of discussion by surface experimentalist Salmeron, who pointed out the lessons from decades of surface science that very small impurity concentrations in bulk can be greatly magnified at a surface by a segregation energy, and that impurities from the ambient atmosphere, hydrocarbons for example, can rapidly change the nature of a surface under study. That this might be a relevant issue was discounted at the discussion by practitioners of ellipsometry. But dismissing the *only* suggested resolution is not helpful. The discrepancy must have a source, and if it is not contamination, one needs to ask if it can be a failure of the highly developed force-fields used in the simulations, or the quantum chemical calculations that confirm them. A positive outcome of the discussion, one hopes, is that a serious effort to resolve the discrepancy will now be undertaken.

Several studies were debated at our Discussion aimed at determining the range over which cellular water near a protein differs from bulk water. With the foregoing surface-science history in mind, one wonders if it might make sense at this juncture to step back from the intra-cellular studies in favor of measurements in the more controllable and characterizable environment of a surface science experiment. One such study was discussed in paper 21 [63]. Another, allowing for examination of a broader range of surfaces, would be to use Houston's interfacial force microscope (IFM) [42], with which one can quantify forces between a tip of large curvature radius and a flat sample, both functionalized however the experimenter chooses, *i.e.* hydrophobic or hydrophilic, with or without self-assembled monolayers, *etc.*

The IFM is effectively a zero-compliance atomic force microscope (AFM). Instead of suspending a tip from a soft cantilever, whose deflection is a measure of the force between tip and sample, in the IFM the tip is mounted on one side of a stiff seesaw whose tendency to rotate in response to tip–sample interaction is balanced by delivering charge to capacitor pads on the seesaw's back surfaces. The amount of charge delivered measures the force.

The force balance approach has the advantage that force *versus* separation can be measured throughout the attractive region, without snap to contact which limits the range of separations over which AFM can generally be applied. (Snap to contact occurs when the derivative of the tip–sample attraction with respect to separation exceeds the cantilever spring constant. The IFM

seesaw is stiff enough that this essentially never occurs.) Force between tip and sample in a fluid, or connected by a meniscus, can be measured with the IFM *versus* approach or recession speed, or 90° out of phase with an imposed lateral oscillation, allowing measurements of viscosity *versus* separation. This capability has been used to quantify changes in viscosity attributable to confinement of water at the sub-nanometer level.

Figure 8, for example, shows the force experienced by an OH-functionalized W tip as it approaches an OH-terminated silica sample, in water. (Figure 8 was kindly provided by J. E. Houston (private communication). The data in the Figure are representative of work reported in detail by [10]). Note that resistance to drainage of the water between tip and sample is close to zero when the separation is 20 . But as the separation decreases toward 10 , the force rises, and it does so proportionately to the tip–sample approach speed, as it should if hydrodynamics is applicable to the observed behavior. From this data set, one can therefore extract a viscosity for the nano-confined water film. Remarkably (and controversially—compare *e.g.* ref. [63]), it is roughly a million times the viscosity of bulk water. Refining this methodology will doubtless eliminate issues of surface characterization. Extending the results to surfaces functionalized to mimic the intra-cellular environment should then produce ideas transferable to the analysis of bio-systems.

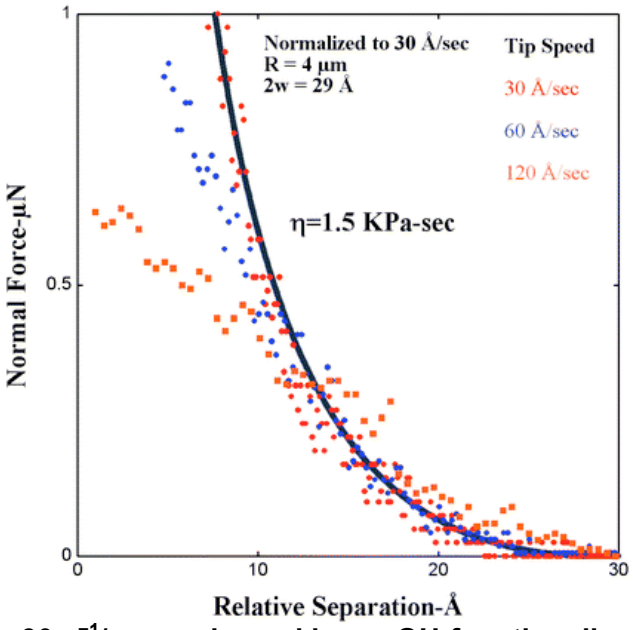


**Figure 8. The force × 30 $s^{-1}$/*v* experienced by an OH-functionalized W tip of curvature radius *R* = 4 m, immersed in water, as it approaches an OH-coated, flat silica sample at three different approach speeds, *v* (This figure was kindly provided by J. E. Houston (private communication); the data are representative of work reported in detail by [10].) For separations between 10 and 30 , the force is proportional to the approach speed, as a hydrodynamic model would predict. Pursuing this interpretation, the solid line represents a solution to the Navier–Stokes equation, (see ref. [41]) based on the assumption that tip and sample are each coated with a water interphase of thickness *w* = 14.5 and a viscosity = 1.5 kPa s. The latter is about a million times the viscosity of bulk water.**

It is worth expanding on the notion that what we should be about is producing *transferable* ideas (a.k.a. take-home messages). Several papers discussed succeeded in that, making them especially noteworthy and attractive for follow-up—whether or not one agrees with the conclusions. Here are some examples:

Tobias *et al.* [59] – The enhanced translational mobility of water above 200 K, seen in both the mean-squared amplitudes extracted from neutron data and the mean-squared displacements computed from the MD trajectories, can be attributed to an increase in the population of water molecules that escape their cages with increasing temperature.

Qvist *et al.* [58] – The hydration layer can be regarded as a defect in the predominantly tetrahedrally coordinated H-bond network of bulk water, induced by a protein surface that provides fewer and less flexible H-bonding opportunities for the adjacent water molecules. These constraints slow down water rotation because they interfere with the cooperative mechanism that facilitates rotation in bulk water.

Salmeron *et al.* [64] – We propose that the hydrophilicity of mica above 0 °C is related to the fact that dangling H from the water molecules are formed easily above the monolayer upon adsorption of additional water.

Also: All the examples discussed here support a mechanism for molecular-scale wetting by water that is strongly dependent on the ability of the surface to produce dangling H-bonds, from either molecular water (mica, Pd, Ru), or OH groups (oxides with defects).

Perkin *et al.* [63] – This study has allowed us to formulate two conditions which must be satisfied in order for hydration lubrication to take place: (i) ions must remain bound to the shearing surfaces under confinement; and (ii) the surface-bound ions must retain their hydration sheath under confinement and applied load.

Adding to the toolkit of big ideas for water–solid interactions has been the primary focus of my own efforts. To put the views I have expressed here in better perspective, I conclude with some brief examples.

The first involves my entrée into the science of water on surfaces, in which I aimed (a) to see whether density functional theory at the level of modern approximate functionals is up to the task of analyzing the structure of hydrogen-bonded systems, and (b) to explain what was, in 2001, the only water adsorption system for which atomic coordinates had been measured (in the LEED experiment and analysis of Held and Menzel[65]). Held and Menzel had expected that because of the small (4%) mismatch between the lattice repeat of the basal plane of ice Ih and that of Ru(0001), the first water molecules deposited would aggregate into a puckered hexagonal bilayer, similar to the water layers that stack to form the 3-dimensional ice-Ih crystal. To their surprise, the LEED data implied otherwise, specifically that in the wetting layer on Ru(0001), the O atoms are virtually coplanar.

Eight years later, a simple chemistry idea led to understanding [35]. It is that if the O atoms of the water layer are at roughly the same height above underlying Ru atoms, all of them must be forming bonds. In the ice-like bilayer, this is not possible for the half of the water molecules that have an H-atom dangling into the vacuum (see Figure 9, left panel). The reason is that bonding between that H atom and its O neighbor uses up the power of the O(2p$z$) orbital to bind, and this is just the orbital whose hybridization with the Ru d-band is needed to form an O–Ru bond. This argument immediately links coplanarity of the O atoms in the wetting layer to dissociation of the dangling H-atom, which then must (and easily does) find an alternative spot on the surface at which to adsorb.

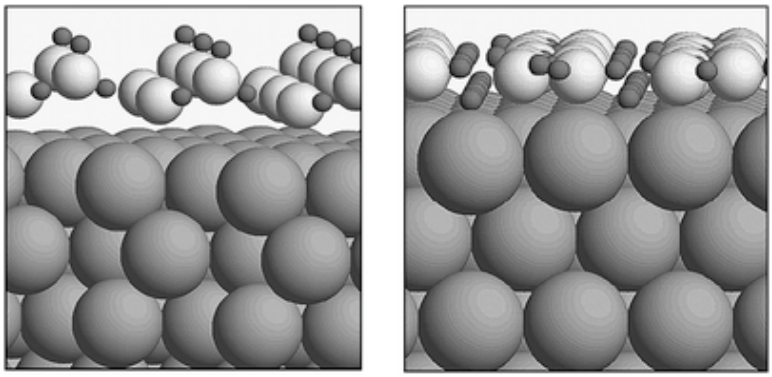

**Figure 9. Side views, after ref. [35], of an optimized, intact and a half-dissociated water adlayer on the Ru(0001) surface. Large, intermediate-sized and small balls represent Ru, O and H atoms respectively. Note, in the left panel, O–H bonds dangling into the vacuum above. In the right panel, formerly dangling H atoms are bound to the surface, and the O atoms to which they were attached have moved into chemical contact with underlying Ru atoms. The result is an adlayer with virtually coplanar O atoms.**

Subsequent density functional calculations showed that (a) the half-dissociated water adlayer does indeed have coplanar O adatoms (see Figure 9, right panel), and (b) the binding energy of the dissociated layer is substantially greater than one finds for a bilayer of intact water molecules. Thus, Held and Menzel's structural measurement ultimately yielded a simple and presumably transferable idea.

A follow-up study produced another important notion, this one more properly in the realm of physics. Although the half-dissociated layer was shown to be considerably better bound in the DFT calculation than an intact molecular layer, it was only *equally* well bound when compared to 3-dimensional ice Ih. Thus, there was still no explanation of why wetting should occur, thermodynamically. That emerged from a study of the zero-point corrections to water binding [66]. It made plain that zero-point energy favors dissociation, for a simple reason. The O–H bond is strong, short and stiff. Replacing it with an H–Ru bond that is weaker, longer and softer means substantially reducing ½. Thus, it is the quantum nature of the proton that, ultimately, makes the dissociated adlayer the thermodynamically preferred state. The thought that zero-point corrections are not just a minor numerical add-on, but can have important structural consequences, is surely an important and transferable one.

Research that helps us refine conventional wisdom is of great value. In water adlayers at low temperature, for example, one generally assumes that the best bound structures are characterized by a perfect H-bonding network, this despite the conflicting idea that wetting only occurs if the dominant energy involves water–substrate as against water–water bonding. Recent efforts on my part to explain the binding of water to Pt(111) suggest that relieving surface strain in a water adlayer may overcompensate the loss of binding associated with breaking H-bonds [67]. Consider, for example, the optimized, trial wetting structures illustrated in Figure 10. The lower panel shows the experimentally observed 39 × 39–R16.1° supercell [68-70] filled by 32 water molecules, as assumed to be the right number by Glebov *et al.*, [70] because that allows for a perfectly H-bonded, if seemingly compressed water layer. (Compression is defined here relative to the area density of water molecules in ice Ih. In reality, there is no way to define a natural

standard for the density for the first water layer on a metal. For example, in the H-down structures of Figure 10, bonding is not tetrahedral about the O atoms, unlike that in ice Ih. Standard or not, though, it is reasonable to assume that the constraint of pseudomorphism imposes a strain whose relief will benefit the binding of the wetting adlayer.) The upper panel shows a trial geometry in which one of the 32 water molecules has been removed, and the starting H-bond topology reorganized to allow the layer to remain fully H-bonded, albeit with two pentagonal water rings among the remaining hexagons.

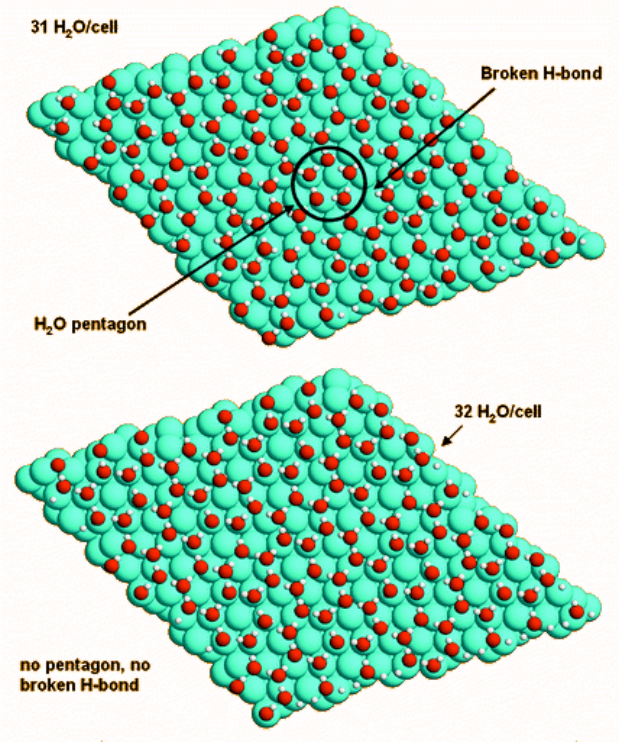


**Figure 10. Comparison of optimized 39 × 39–R16.1° $H_2O$/Pt(111) supercells containing 31 (upper panel) and 32 (lower panel) water molecules, with cyan, red and white balls representing Pt, O and H atoms. Note the broken H-bond and the $H_2O$ pentagon in the upper panel. Despite these defects, the binding energy per $H_2O$ is only 2 meV less than in the perfect wetting structure of the lower panel, an amount essentially in the noise. The structures were optimized with the VASP total energy computer code [71-74] using the PBE generalized gradient approximation [75], and electron–nucleus interactions treated in the projector augmented wave (PAW) approximation [76, 77]. The Pt(111) surface was modeled as a 3-layer slab, with the atoms of the lowest layer fixed at theoretical bulk separations, the water layer adsorbed on the top surface only, and the unphysical fields associated with this asymmetry compensated [78]. The plane-wave basis was cut off at 700 eV, and the surface Brillouin zone sampled by an equally-spaced, 3 × 3 mesh of k-vectors. Note that the water molecules whose O–H bonds are not roughly parallel to the surface are H-down. That is, one of their H atoms lies between the O atom and the metal.**

After optimization, as the panel shows, the 31-molecule layer has relaxed, such that one pentagon remains and one H-bond is broken. The binding of this structure is only 2 meV less than of the conventional 32 $H_2O$ molecule arrangement, perhaps showing the way to a wetting

motif quite different from what is anticipated based on our knowledge of the structure of ice Ih. Whether this is a valuable insight remains to be shown. In the high resolution images of Morgenstern *et al.* [79] one does not see pentagons or vacancies. On the other hand these images also do not manifest the 39 × 39–R16.1° supercell observed in the diffraction studies. Thus further experimental work may be the key to making pursuit of the strain-relief idea timely.

A last example concerning timeliness bears on whether the systematic error inherent in current approximate versions of density functional theory is confounding our efforts to understand water behavior near surfaces. Many efforts to find a first layer arrangement of water molecules on Pt(111), for example, including those represented in Figure 10, have failed to reveal one whose binding exceeds that of ice Ih, and thus would be a thermodynamic wetting structure at 0 K. Pt(111) is, after all, observed to be a complete wetting substrate [68-70]. Is this a failure of the imagination, or of simulations to find the deepest well in a many dimensional hyperspace? Or is it a symptom of the inadequacy of today's approximate functionals? The answer might be found by continuing to spin the surface theorist's roulette wheel, *i.e.* by continuing to dream up new, potentially better structural motifs. What may be at stake, however, is an issue of timeliness, *i.e.* that we would spend our time more fruitfully doing something else till a functional is developed whose accuracy is an order of magnitude better than what is available today.

A related example is the subject of my contribution to the themed issue of *Physical Chemistry Chemical Physics* accompanying this Discussion [80], on the relevance of lattice match to the effectiveness of a potential ice-nucleating nano-crystal. The use of AgI smoke to nucleate ice in clouds and thereby make it rain was suggested by Vonnegut, some 60 years ago, on the basis of his survey of lattice constants, which revealed that those of -AgI and of ice Ih match to within 1% [40]. In ref. [80], I report that the match is much worse in a survey of DFT approximations, making them a poor way to explore what physical phenomena might make lattice match a relevant parameter. A technical advance is needed, in other words, before the lattice match problem becomes timely. Perhaps it will involve an improved account of van der Waals forces [81]—just the sort of advance that could convert many problems involving water–materials interactions to timely ones for the theorist.

### *2.3.2 Acknowledgements*

Thanks to the organizers of Faraday Discussion 141 for the opportunity to present this overview. VASP was developed at T. U. Wien's Institut für Theoretische Physik.

## 2.4 Mechanics of Soft Interfaces Studied with Displacement-Controlled Scanning Force Microscopy

The following abstract and excerpts are from an article published under the above title in *Progress in Surface Science* (2010), doi:10.1016/j.progsurf.2010.07.003, by M.P. Goertz and N.W. Moore.

### 2.4.1 Review Abstract

The development of scanning force microscopes that maintain precise control of the tip position using displacement control (DC-SFM) has allowed significant progress in understanding the relationships between the chemical and mechanical properties of soft interfaces. Here, developments in DC-SFM techniques and their applications are reviewed. Examples of material systems that have been investigated are discussed and compared to measurements with other techniques involving nanoprobe geometries to illustrate the achievements and promise in this area. Specifically discussed are applications to soft interfaces, including SAMs, lipid bilayers, confined fluids, polymer surfaces, ligand-receptor bonds, and soft metallic films.

### 2.4.2 Excerpt Abstract

This section reviews several important contributions that displacement-controlled mode scanning probe microscopy (DC-SFM), of which IFM is one example, has made to understanding the structure and properties of fluids confined between surfaces separated by less than a few nanometers. In particular, we discuss examples where controlling the probe displacement with force feedback has revealed unprecedented detail about the interfacial forces created by the nucleation and transport of fluid between a probe tip and a substrate.

### 2.4.3 Crystallization of Nanoconfined Liquid Molecules

A variety of fluids have been shown to pack into liquid crystals at room temperature when confined between molecularly smooth surfaces, such as mica, when the confining surfaces are separated by a distance smaller than 5~10 diameters of the fluid molecule [82-88]. This has been posited to occur because of epitaxial nucleation of fluid molecules near the fluid-solid interface when there is strong attraction or bonding between fluid and solid molecules, or because of colligative effects, i.e., packing constraints [82, 88, 89]. That confinement can induce fluid structure has raised broad questions about how nanoconfined fluids structure near surfaces and respond to shear forces. Answering such questions is important for understanding thin film lubrication and molecular transport associated with chemical reactions at surfaces [4]. In particular, water-surface interactions drive many biological, atmospheric and geochemical reactions, the kinetics of which may be influenced by how tightly bound water is to a surface. The reviews of Henderson [4] and of Hodgson and Haq [90] on water / solid surface interactions, which together have a staggering 1,490 references, testify to the growing knowledge and interest in this area.

Fluid structuring in nanoconfinement has been explored in great detail both experimentally and theoretically for both aqueous and nonaqueous fluids (for reviews, see [82, 83]). Here, we compare just two examples—the experimental work of Horn and Israelachvili using a standard SFA [91], and that of Stewart and Parker using an SFA modified to allow feedback-controlled displacements [92]. In both experiments, a droplet of octamethyltrichlorosilane (OMCTS) was placed between two mica sheets and slowly squeezed until the mica plates touched. Figure 11(a,b) shows an example of the force (F) that was measured with each technique, normalized by the effective contact radius (R), as a function of the intersurface separation (D). The intersurface force was oscillatory as fluid molecules were packed into a liquid crystal and made discrete changes in their fluid density at discrete levels of confinement. The results were consistent with

other findings that the decay length of the magnitude of this oscillatory force scales in distance as ~1.2–1.7 molecular diameters for a wide range of fluids [82]. Frantz, et al., [93] obtained a similar result using an SFA modified to measure the intersurface separation by monitoring changes in the capacitance of silver films deposited underneath the opposing mica substrates. Operating the SFA in open-loop (without feedback-control of the probe position), they found that the oscillations in the force-distance profile closely resembled the molecular diameter of OMCTS (7.5–8.5 Å).

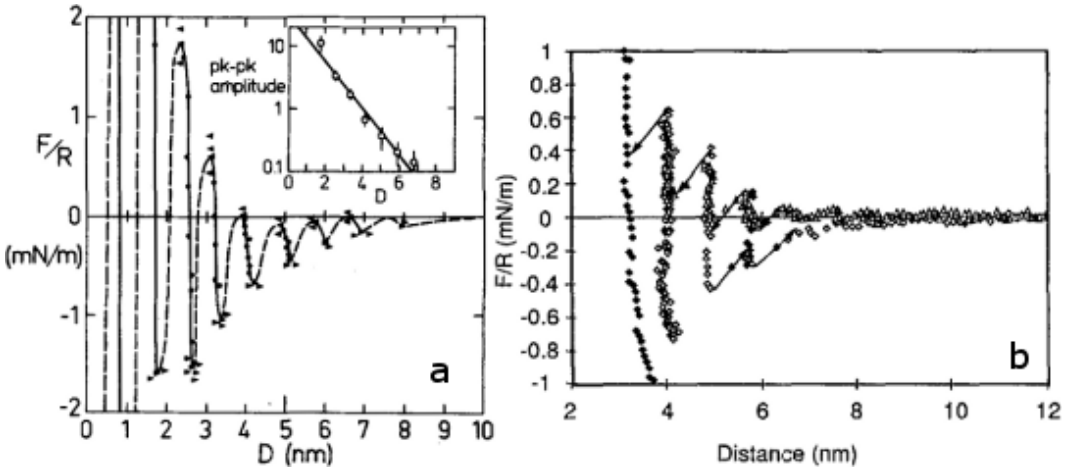


**Figure 11. Oscillatory forces measured during the compression of OMCTS (a) in a conventional SFA without displacement control [91] and (b) in a modified SFA using electrostatic displacement detection and feedback actuation [92]. In (a), the data are shown as dots, while the line is a fit to a sinusoidal model of variable amplitude, provided as a guide to the eye [91]. The inset in (a) shows the peak-to-peak amplitude of the force as a function of the interface separation. In (b), different symbols indicate different measurement runs; arrows indicate force jumps during inward and outward runs.**

While both techniques show the same general features, the exact form of the force-distance relationship could only be guessed at when displacements were not controlled with feedback (Figure 11a). The displacement-controlled SFA measured many fine features directly. For example, from Figure 11b, it is clear that the force gradient prior to each yield point was nearly vertical upon compression. Upon decompression, the force showed a nonlinear adhesive force prior to each discrete change in crystal density. Comparing the two methods in Figure 11(a,b) shows that the sinusoidal model shown in Figure 11a using the standard SFA measurements only approximated the real material behavior.

### *2.4.4 Liquification at the Surface of Ice*

As shown above, the crystallization of nanoconfined fluids is an example of a phase change that depends strongly on the extent of confinement. A striking example of interfacial phase change that is induced by a *lack* of confinement is the premelting of ice to form a liquid-like layer (LLL) at the air interface below the melting temperature of ice. Premelting occurs because atoms or molecules near the solid surface are less constrained, so that the upper few epitaxial layers assume a less-ordered structure. The structure and thickness of the LLL is then a strong function

of the thermodynamic conditions (temperature and pressure), as well as kinetic growth processes and the concentration of salts or other impurities near the interface (for reviews, see [94-97]. The general consensus is that the LLL exists on the ice surface at temperatures higher than approximately -35 ºC and that its thickness increases with temperature. While premelting is common to many solids, for ice, with a melting point of 0 ºC, it has broad consequences, ranging from geological and atmospheric sciences to daily life. More broadly, the debate over why ice is so slippery has been ongoing for over a century and a half and, while much is now known, the question is not entirely resolved [28, 94, 95].

IFM has recently been used by Goertz, et al., to investigate the thickness of this LLL layer with respect to temperature [28]. In the experiment, a glass tip was moved rapidly toward the ice surface, which sublimates (or evaporates) rapidly at these temperatures, while the interfacial force was recorded. Figure 12a shows examples of five such force-displacement profiles measured at temperatures ranging from -10 to -30°C. The initial contact between the tip and the LLL was signaled by the onset of attractive force (negative values), far from the bulk-ice surface, the latter being identified by where the force rises steeply toward positive values. The distance between where these transitions occur was used to define the thickness of the LLL, as marked in Figure 12a. It should be noted that the LLL may flow and neck onto the tip, akin to when a tip touches the surface of water and forms a meniscus. This would extend the range of the force interaction between the tip and ice surface. Thus, the thickness of the LLL defined in this manner may be somewhat larger than the thickness of the LLL before it is perturbed by interaction with the probe. Nonetheless, the LLL thickness showed a logarithmic dependence on the temperature ($T$) relative to the melting point ($T_m$) though $\Delta T \equiv T_m - T$ (Figure 12b), consistent with earlier observations and theory [97]. For example, Döppenschmidt and Butt [98] conducted a nearly identical study using relatively soft AFM cantilevers, and inferred the LLL thickness from the distance from the surface at which the jump-to-contact occurred. They found the same temperature dependence as the IFM measurements, and LLL thicknesses of the same order (e.g., a few tens of nanometers at -10ºC) [98].

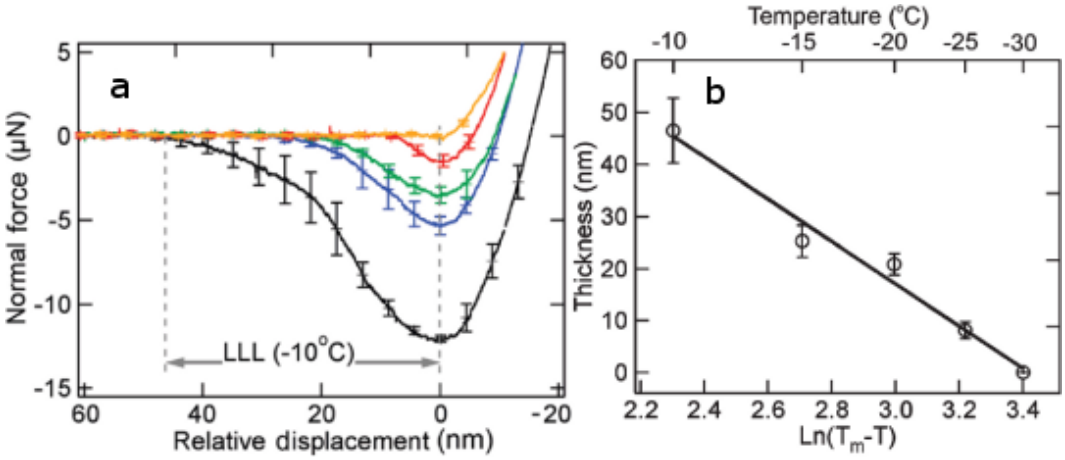


**Figure 12. (a) Force between an IFM tip and the liquid-like layer (LLL) on ice at various temperatures (bottom to top curves: -10, -20, -30, -40, and -50 ºC, respectively). (b) Temperature dependence of the LLL thickness. Error bars represent the standard deviation over five measurements. The temperature (T) is plotted as the logarithm of its deviation below its normal melting point (Tm).**

It is interesting to note that the persistence of the LLL well below the melting point of ice has important implications for understanding why ice is so slippery. Friction between macroscopic bodies always involves contact between multiple asperities, which can deform under stress, and channel the flow of lubricating fluid [99]. Thus, the LLL acts in part as a lubricant, but also affects the effective area of contact between the ice and another contacting surface. The situation can be complicated by frictional heating and/or pressure melting, which change the quantity of fluid near the solid-ice interface [97]. Thus, while many of the fundamentals are understood, applying these concepts to realistic situations has remained a challenge [99].

### *2.4.5 Nanobubble Nucleation Between Hydrophobic Surfaces*

Another dramatic example of phase change at interfaces where DC-SFM has been applied is in measuring the forces and distances at which a nanobubble will spontaneously form between opposing hydrophobic surfaces immersed in water, creating a strong attractive force between the two surfaces. Debate persists regarding the origin of this so-called "hydrophobic force" that drives this transition, which can operate over far distances (up to several microns) compared to other forces that arise between surfaces (e.g., van der Waals, electrostatics, osmotic repulsion), which typically operate over length-scales of tens of nanometers or fewer [82, 100]. It is now recognized that the range of cavitation is sensitive to the amount of dissolved gases in the water, as well as the roughness and energies of the surfaces used to create the confinement (for reviews, see [101-103]).

Singh, et al., [104] was the first to examine this phenomenon with DC-SFM, and termed the replacement of liquid by vapor a "drying transition". The experiment was performed by placing a roughened, superhydrophobic silica sphere (contact angle with water ≥170º) onto an IFM sensor as a probe tip, and slowly moving it toward a Si surface functionalized to be superhydrophobic, with both tip and surface immersed in water [104]. Consistent with prior work, they observed that the hydrophobic force can extend several microns, even when the liquid was meticulously

degassed [101-103]. More unique was the use of IFM, which uses electronic feedback to create high effective stiffness (~400 N/m) of its sensing element. This allowed the stiffness of an air-water interface to be measured using the same hydrophobic tip. Indenting the air-water interface is similar to the action performed by the hydrophobic feet of water striders. Singh et al., measured the interfacial stiffness to be ~0.15 N/m, or about four orders of magnitude less than the steepest force gradient measured during the cavitation of a nanobubble when the tip was submersed in water near a hydrophobic surface. This demonstrates a unique ability of DC-SFM that, in general, it can measure a very broad range of interfacial stiffnesses with the same tip configuration [105]. That is, performing the same experiments with a open-loop cantilever-based method, such as AFM, would require using multiple cantilevers to avoid the jump-to-contact instability and maintain suitable force resolution for the entire range of material stiffnesses of interest.

### *2.4.6 Hydration Repulsion Inside a Nanoconfined Meniscus*

An example of interfacial phase change analogous to the prior example is the spontaneous condensation of water vapor between two hydrophilic asperities in humid air and separated by less than a critical distance (~nanometers). The formation of a nanoscale liquid meniscus is essentially an inverse process of the drying transition discussed above (for reviews, see [82, 106]). The active control of the probe position in DC-SFM affords high accuracy in determining the relevant thermodynamic variables. We briefly show two examples where DC-SFM has been used to infer the structure of water near such hydrophilic surfaces. These examples also highlight how DC-SFM has been used to show the connection between surface chemistry and wettability in nanoscale geometries.

Several authors have used IFM to study the range of formation, the interaction force, and the viscoelastic properties of nanomenisci [8, 10, 29, 107]. These studies have shown unprecedented detail in the force that evolves between a probe and nearby surface as vapor condenses into liquid and is displaced beneath the approaching probe. An example is the work of Xu, et al. [107], who measured the interaction between W and mica surfaces at various humidity levels. An example of their results is shown in Figure 13a. As their W tip approached the mica surface, at first a liquid meniscus condensed from the vapor (Point A in Figure 13a), creating a strong attractive force, in analogy with the drying transition discussed above. The near-linear shape of the force-distance profile just after Point A is consistent with a large body of theory for capillary forces between two smooth asperities of identical material that are perfectly wetting (e.g. [108]). However, the W tip surface is not atomically smooth, and neither the W nor mica are identical or perfectly wetting, which may explain the nonlinearity in the force after the meniscus initially forms [109]. The adsorption isotherm of each surface is now known to contribute to the humidity dependence of the capillary adhesion force [110]. Xu et al., also note that the atomic steps of the W-oxide probe may cause the many sub-nanometer, step-wise changes in force as the meniscus spreads along the approaching tip and as more water vapor condenses.

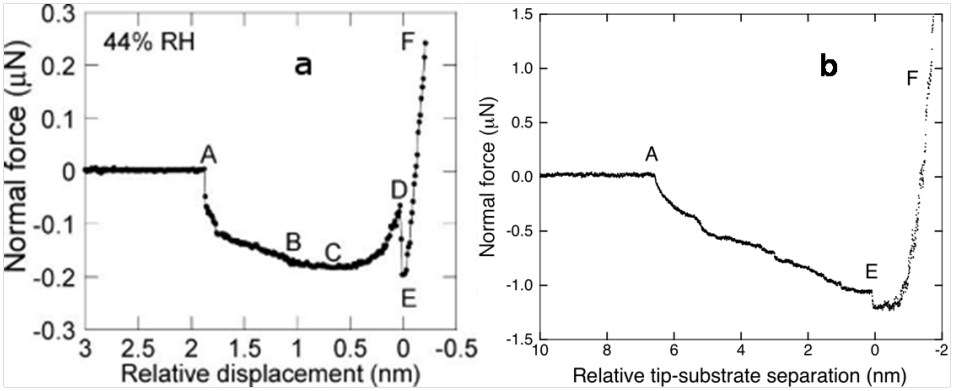


**Figure 13. Comparison of force profiles measured in humid air with IFM as a W tip approached surfaces of (a) mica (44% RH) [107] and (b) Si(111) (50% RH) [111]. Points labeled A−E represent positions for the initiation of water nucleation and condensation, the formation of a complete water bridge, the maximum attractive force before tip−substrate contact, the sudden force drop, and the tip−substrate contact, respectively.**

An even more striking feature in Xu's data appears above 20% RH. At about 0.5 nm before the tip and mica contacted, a repulsive force evolved that increased with relative humidity (Figure 13a, Points C-D). They attributed this repulsive force to that required to squeeze out "ice-like" water nucleated at the mica-liquid interface. This interpretation is consistent with oscillatory force-displacement curves that have been observed when AFM tips have approached mica surfaces submerged in water (e.g. [112]). Fitting the data to an appropriate contact mechanics model, the authors inferred a reduced elastic modulus of ~7 GPa for the ice-like film, of the same magnitude as that for bulk ice (~11 GPa) [107]. Another finding was that above a critical stress, the structured film near the mica surface collapsed (Position D), and thereafter the force was dominated by compression of the W and mica surfaces (Position E). From this yield force and the assumed tip geometry, the authors estimated that the ice-like film had a yield strength of about one-tenth of the theoretical strength of bulk ice.

Xu's interpretation of these data is consistent with a growing body of probe-based and spectroscopic evidence that water assumes an "ice-like" structure near certain hydrophilic surfaces at room temperature, where it may form a solid or semi-solid film a few molecules thick [10, 11, 107, 113]. Few theoretical investigations have been able to justify this view, however, owing to the incredible complexity in modeling water-solid interactions [11]. The term "ice-like" has been used liberally to distinguish the properties of interfacial water from those of bulk water. Though the use of this term elicits images of its structure that may differ considerably from the structure of bulk ice, and may differ near different substrates [11, 22]. In particular, mica contains a high density of $K^+$ ions that are exposed at its surface, the hydration of which can be expected to strongly influence water structuring [4]. This idea was recently demonstrated by Perkin, et al. [114], who used SFA to show differing lubrication properties for solutions of different salts confined between mica surfaces separated by only a few nanometers.

To show that water may structure quite differently near silica surfaces, Moore repeated Xu's experiment using nearly identical materials and conditions except for the substrate, which was a surface of native oxide terminated Si(111) [111]. This surface was made rich in hydroxyls by treating it with strong acid [10], and was therefore very hydrophilic (contact angle ≤10º). The

result, shown in Figure 13b, was qualitatively similar to Xu's, except that no repulsion was observed prior to the tip-substrate contact. If Xu's interpretation that ice-like water forms at the mica-water interface is correct, then either its structure could not be resolved near Si(111), or ice-like water does not form on that particular surface. If the latter is true, it would seem that hydrophilicity is not the only requirement for establishing long-range order in water near surfaces. One clue comes from the surface structure of the hydroxylated oxide of Si(111), which may be less ordered than the cleaved mica surface in Xu's experiment. Asay and Kim [113] used ATR-IR to examine isolated silica surfaces in humid air, and concluded that water bonds near the Si(111) surface, forming an "ice-like" network with a thickness of several monolayers. However, how such structuring might differ when water is confined between two surfaces has by no means been established experimentally [115].

A further illustration is the work of Bonander and Kim [84], who studied the structure of water near silica surfaces entirely submerged in water using their "CO-IFM". Bonander and Kim showed that the CO-IFM's active control of the probe position reduced the noise in the force signal by over an order of magnitude compared to using the same AFM tip without the feedback control enabled (Figure 14a). The small tip geometry and careful control of the AFM tip position allowed them to observe an oscillatory force when the probe approached to within a few nanometers of a silica substrate immersed in water (Figure 14b. inset). As expected from earlier work with SFA (see Section 3.2.1), the period of this oscillation (3.2±1.3 Å) was ~1.7 times the molecular diameter of a single water molecule [84]. Surface charges and dissolved ions produced a repulsive electrostatic interaction that superimposes upon these smaller oscillations (Figure 14a). That oscillations in the force-distance profile were observed with W probes submerged in water near atomically-smooth mica (Figure 13a) and with smaller AFM-like tips near silica (Figure 14b), but not with micron-sized W tips on Si(111) (Figure 13b) could arise from epitaxial considerations, viz., differences in roughness on the probe tip or substrate, and/or from differences in chemical structure of the surface [83]. As yet, a careful determination of this has not been made, however.

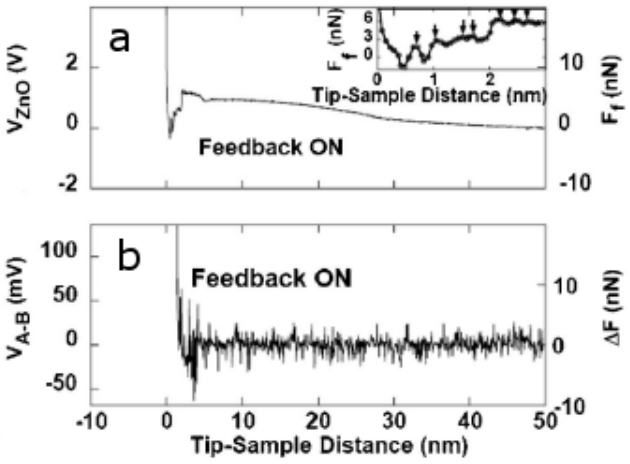


**Figure 14. Force-displacement curves obtained with Bonander and Kim's CO-IFM [84], for a tip submerged in water near a silicon surface: (a) without and (b) with a force activated voltage feedback system. The voltages of the monitoring and control circuits (left-hand ordinates) correspond to the interaction (Fi) forces between tip and substrate. Inset in (b) shows an enlarged force-distance curve between 0 and 3 nm.**

### *2.4.7 Viscosity of Molecularly-Thin Hydration Layers*

In addition to structure, understanding the viscoelastic properties of interfacial water is important for developing a universal understanding of how water-solid molecular interactions affect molecular transport in biological and environmental processes [82, 116]. Whether water has a different viscosity near surfaces has been debated since the early 1900s and remains controversial [11, 99, 117-119]. Measuring the viscoelastic properties of a hydration layer only a few molecules thick [11] is an extraordinary challenge. This is evidenced by reports of the effective viscosity of nanoconfined fluids ranging from one to over one billion times their bulk counterparts—for a wide variety of fluids, confining materials, experimental techniques, and assumptions made in analyzing the data [8-10, 45, 114, 120-130].

Among these works, IFM is the only DC-SFM tool that has been used. This has been accomplished either by dithering the probe tip laterally along a surface submerged in water, or by pushing the tip toward the surface at different speeds. In both cases, the component of the force that is speed dependant can be related to the rate of energy dissipation, and thus related to the fluid viscosity using suitable fluid dynamics models [41, 131]. Based on IFM measurements, viscosity values for interfacial water have all been inferred to be on the order of a million times greater than that of bulk water [11, 99, 117, 118]. This result has been achieved whether water was confined between a hydrophilic tip and oligo-poly(ethylene glycol) [9], carboxyl-terminated SAMs [8], hydroxylated silica [10], or ice [28]. Measurements by Li et al. with AFM have also measured high shear forces between a probe and interfacial water near mica and silica surfaces that can be interpreted as an exceptionally large viscosity for the hydration layer [45]. Hydration layers have also been shown to have exception viscosity when confined between mica sheets and silica using SFA [124] and a custom shear device [125], respectively. The idea that interfacial water may have elevated viscosity is not unreasonable in light of the aforementioned

spectroscopic studies of interfacial water and because of the observation of oscillatory forces during its compression under certain conditions (e.g., Figure 11).

Extraordinary viscosity in confined fluids has not always been observed, however. A few examples include: 1) measurements by Lee, et al., who used an AFM-like configuration to measure the viscosity of nanoconfined water nearer to 10 times the bulk value [126]; 2) SFA measurements by Israelachvili of tetradecane and water, which showed <10% deviation from their bulk viscosities [132]; SFA measurements by Raviv et al. suggesting fluidity of the hydration layers down to at least 1 nm of confinement [129, 133], and 4) computer simulations by Leng and Cummings [127] of water confined between mica surfaces, which suggested viscosities *less* than or equal to the bulk value, and shear thinning behavior. Similarly, molecular dynamics simulations have been used to show that water confined between hydrophilic SAMs separated by only a few nanometers showed a reduction in diffusivity less than 2 orders of magnitude compared to bulk water at the same densities and pressures (e.g., [27, 115]). This arose, in part, from the geometry itself, which approximates a two-dimensional pore as the intersurface gap was made smaller, as well as from temporal structuring of fluid molecules between and around the hydrophilic SAM termini, via hydrogen bonding and orientational constraints within the confined geometry. If one assumes the Stokes'-Einstein relation is valid at this scale, so that viscosity and diffusivity are inversely proportional, then one might guess that this reduction in molecular mobility may result in a larger effective viscosity by perhaps at most 2 orders of magnitude. It is also important to recognize that relating the measured lateral force against a scanning probe tip to fluid viscosity requires making an assumption about the presence or absence of hydrodynamic slip at the fluid-tip and fluid-substrate interfaces, which adds an additional degree of freedom that must be accounted for in modeling the data [87, 134]. As well, the curved probe-on-substrate geometry can only indirectly measure the effect of a viscous interphase only a few molecules thick, as the majority of the force on the probe arises from drag of bulk fluid that is much farther than a few molecular distances from either surface [135].

A challenge of measuring thin film viscosity that is unique to DC-SFM is the necessity of deconvoluting the internal damping of the force-feedback sensing mechanism from viscous forces created by the tip-sample interaction [105]. As both can be dissipative, they cannot always be easily distinguished without a unified model for the flexure and dissipation/dynamics of the entire measurement train (i.e., substrate, fluid, tip, mechanical elements of the sensor, and the detection/feedback electronics) [105, 136]. In general, the dynamic response of each of these components is frequency dependant, so that the rate of energy storage and loss in each component may have different dependencies on the gradients of force in displacement and time. Developing an accurate instrument model is nontrivial, but has been performed for an early-generation IFM [136], and for two low-force nanoindentation systems [105]. Whether or not dissipation within the IFM sensor could singly account for the extraordinary viscosity values measured for interfacial water with IFM remains unsettled, however.

### *2.4.8 Acknowledgements*

We thank Bruce Bunker for reviewing this section, and J.E. Houston for his extensive work developing and applying IFM, which has stimulated so much work in this field.

## 2.5 Viscosity of Nanoconfined Fluids

Table 1, below, lists viscosity values for fluids confined at the nanometer lever using a variety of (mostly) experimental and theoretical methods, for a variety of fluids and chemistries of the confining surfaces. The measurement direction refers to the direction with which one of the confining surfaces was moved relative to the other.

**Table 1. Recent measurements and simulations of the viscosity of nanoconfined fluids**

| Method [1] | Confined fluid | Substrate(s) or exposed surface chemistry | Viscosity relative to bulk (approx.) [2] | Measurement direction relative to interface | Ref. |
|---|---|---|---|---|---|
| FFM | water | HOPG | $10^{10}$ | lateral | [120] |
| IFM | water | Si–OH | $10^{9}$ | lateral | [137] |
| IFM | water | SAM–$CO_2H$ | $10^{7}$ | lateral & normal | [8] |
| SFA | salt solutions (various) | mica | $10^{7}$ | lateral | [124] |
| SFB | organic solvents | mica | $10^{7}$ | lateral | [129] |
| SFA | $MgCl_2$ solution | mica | $10^{7}$ | lateral | [122] |
| AFM | water | mica | $10^{7}$ [2] | lateral | [123] |
| IFM | water | Si-oxide | $10^{6}$ | | [10] |
| IFM | water | OEG | $10^{6}$ | normal | [9] |
| SFM | water | mica | $10^{4}$ | lateral | [125] |
| AFM | water | Si / mica | $10^{3}$–$10^{4}$ | normal | [138] |
| SFA | polymer thin film melts | mica | $10^{2}$–$10^{4}$ | lateral | [139] |
| SFB | water | mica | $10^{2}$ | lateral & normal | [43] |
| MD | water | SAM-$CO_2H$ | < $10^{2}$ [3] | --- | [27, 115] |
| AFM | OMCTS | Si / HOPG | < $10^{2}$ | normal | [140] |
| MD | Water | mica | 90 (D <1 nm)<br>1 (D >1 nm) | --- | [127] |
| SFA | hexadecane, decane, OMCTS | mica | 75 | lateral | [121] |
| AFM | water | glass | 50 | lateral | [45] |
| AFM | water | mica | 35 | lateral | [45] |
| AFM | water | mica | 10 | lateral | [126] |
| SFB | water | mica | <3 (D >1 nm) | normal | [43, 141] |
| MD | Water | DLC-OH | 2–4 | lateral | [142] |
| SFB | salt solutions | mica | 1 | lateral | [114] |

[1] SFB = surface force balance; SFM = shear force microscopy; SFA = surface forces apparatus; IFM = interfacial force microscope; AFM = atomic force microscope; MD = molecular dynamics

[2] Where not explicitly stated, estimated from the author's data as either the loss modulus divided by the oscillation frequency (assuming linear viscoelasticity), or by fitting their data to one of the models of Refs.[REFS-Feibelman].

[3] Based on changes in diffusion coefficient relative to bulk, assuming validity of Stoke's-Einstein relationship.

# 3. THEORETICAL DISCOVERIES

## 3.1 Pentagons and Heptagons in the First Water Layer on Pt(111)

The following was published under the same title; see: S.Nie, P.J. Feibelman, N.C. Bartelt, and K. Thürmer, Physical Review Letters, 105, 026201 (2010)

### *3.1.1 Abstract*

Scanning tunneling topography of long-unexplained √37 and √39 periodic wetting arrangements of water molecules on Pt(111) reveals triangular depressions embedded in a hexagonal H2 O-molecule lattice. Remarkably, the hexagons are rotated 30º relative to the ‘‘classic bilayer’’ model of water-metal adsorption. With support from density functional theory energetics and image simulation, we assign the depressions to clusters of flat-lying water molecules. 5- and 7-member rings of $H_2O$ molecules separate these clusters from surrounding ‘‘H-down’’ molecules.

### *3.1.2 Introduction*

The broad importance of water-materials interactions in nature and technology underlies substantial literature devoted to wetting [4, 90]. Numerous metal single-crystal surfaces are known to support a two-dimensional water layer. According to Young’s equation, that proves they are more attractive to water than water is to itself.

Nonetheless, wetting is understood in only a few cases [13, 90]. One reason is that experimental determinations of wetting-layer molecular arrangements are difficult, and correspondingly rare. Another is that systematic error in state-of-the-art modeling tools, whether first principles or semiempirical, leaves their structural implications open to question, more so when energy differences are relatively small—as in wetting.

With Pt electrodes at the heart of many electrochemical applications, notably fuel cells, the affinity of $H_2O$ for Pt(111) is of particular interest. Still, although the $\sqrt{37} \times \sqrt{37}$-R25.3º and $\sqrt{39} \times \sqrt{39}$-R16.1º periodicities of the low-energy complete-wetting phases on this surface have been known for more than a dozen years [70], their molecular structure has remained a mystery.

New, high-resolution scanning tunneling microscope (STM) images of these structures now provide clues. Following them, with the use of density functional theory (DFT) energy minimization and STM image simulation, we propose $H_2O$-molecule arrangements for both the √37 and √39 wetting phases unlike any previously imagined. The common bonding motif is a cluster of flat-lying molecules enabled to lie especially close to Pt atoms by $H_2O$-molecule pentagons and heptagons surrounding them.

Conventionally, the first wetting layer on a close-packed metal surface (the ‘‘classic bilayer’’) is a single (0001) sheet of ice-Ih, strained to achieve $\sqrt{3} \times \sqrt{3}$-R30º periodicity. Of the two water molecules in its unit cell, one lies almost parallel to the metal surface, binding to it through an oxygen lone-pair orbital, and the other lies several tenths of an Å higher, contributing one O-H bond to the layer’s H-bond network, while the other dangles into the vacuum [4]. To account for

their first observation of the √37 and √39 periodicities on Pt(111) with He diffraction, Glebov et al. modified this picture only slightly [70]. They attributed their observations to icelike sheets of water molecules, rotated and compressed to fit in √37 × √37-R25.3º and √39 × √39-R16.1º supercells.

Why, however, should the structure of Glebov et al. have low energy? The unrotated, uncompressed √3 phase is in itself not a particularly low-energy state. Rotation and compression to form a √37 or √39 moiré make matters worse because now only a relatively small number of flat-lying molecules can be in a low-energy configuration atop a Pt atom [143]. Logic or not, there is also no experimental evidence for such moiré structures. One might hope to find it in high-resolution images, but previous STM experiments [79] did not turn up √37 and √39 wetting phases—hence, our own study.

### *3.1.3 Methods*

We conducted ice growth and STM characterization in an ultrahigh-vacuum chamber with base pressure 4 Â 10À11 mbar. Films were grown by directing water vapor onto Pt(111) at 140 K. The pressure during deposition was typically $2 \times 10^{-9}$ mbar. STM measurements were performed at T < 115 K. To avoid tip-induced damage, we kept the tunneling current <1 pA. Tip voltage was between 0.2 and 1 V. We determined the crystallographic directions of the Pt(111) substrate by evaluating the registry of atomic positions on both sides of an atomic Pt step [32, 144]. All STM images presented herein are oriented in the same way relative to the substrate.

### *3.1.4 Results and Discussion*

Figure 15(a) shows the structure of two-dimensional wetting-layer islands, which form at low coverage (with islands covering about half the Pt surface.) The striking feature is the disordered arrangement of dark triangular regions. The depressions appear to lie 0.3 Å below the bright water rings, compared to an apparent step height of 1 Å at the step edges of the water layer under the same imaging conditions. Surrounding the triangular depressions are hexagonal rings of water molecules, which are rotated approximately 30 relative to expectation based on the classic √3 bilayer. The rotation is evident in Figure 15 (b) in where (at the upper right) a small domain of √3 oriented water appears.

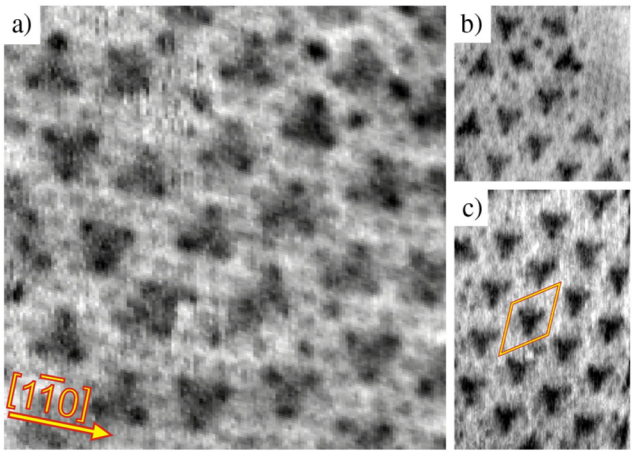


**Figure 15. STM images of submonolayer water deposited on Pt(111) at 140 K. (a) Disordered arrangement of triangular depressions (8 nm × 8 nm, $V_{tip}$ = 0.5 V, $I_t$ = 1 pA), (b) region adjacent to disordered triangles (7 nm × 7 nm, $V_{tip}$ = 0.2 V, It = 1 pA). (c) An ordered region (7 nm × 10 nm, $V_{tip}$ = 0.2 V, $I_t$ = 1 pA).**

Although the disordered structure in Figure 15a is typical of as-grown films, occasionally we find ordered patches of the triangular features (see Figure 15c), whose periodicity and rotation are precisely that of the √37 phase. Understanding the √37 structure thus amounts to deciphering and interpreting the structure of the dark triangles.

The very center of each triangular depression is particularly dark, whereas a continuation of the outer hexagonal network would place a water molecule there. Thus a complete network of hexagonal rings as proposed in previous models [70] cannot be correct.

A satisfactory alternative should adhere to the basic principles that a wetting structure is better bound if the O atoms of more of its flat-lying water molecules are in or near atop sites, if its flat-lying molecules are clustered, so that their O atoms are minimally hindered from approaching the metal (cf. Haq et al. [145]), and if few, or optimally no, H bonds are broken.

With a complete hexagonal network inconsistent with experiment, the last constraint forces us to attribute the dark triangles to topological defects. The area of the triangles suggests they contain 6 $H_2O$ molecules. If these molecules can lie flat, such that their O atoms lie directly above 6 metal atoms, then the 1st and 2nd constraints are also satisfied. Thus, energetic constraints guide us to interpret the dark triangles as di-interstitial defects (cf. Figure 16a), wherein a six-molecule hexagonal ring, rotated relative to the surrounding ones, replaces four molecules of the undisturbed hexagonal mesh [146].

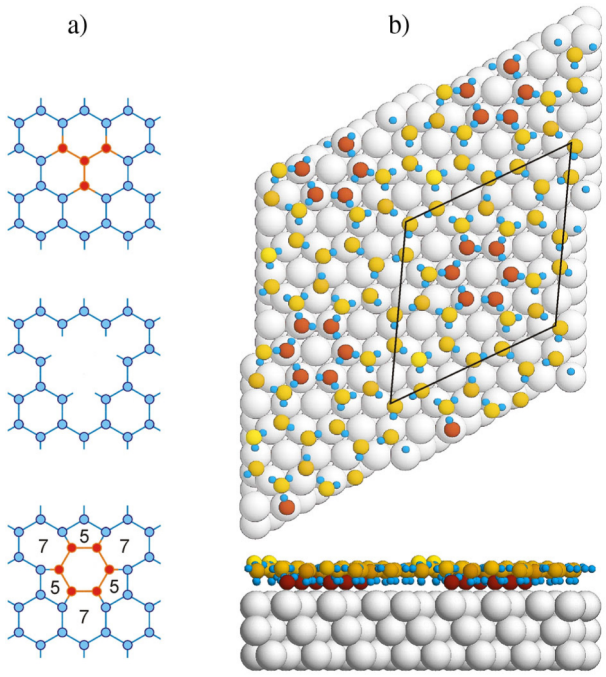


**Figure 16. (a) Schematic showing the formation of a "575757" di-interstitial defect in a hexagonal lattice. (b) Model for the √37 phase of water on Pt(111) incorporating this defect. The atomic positions have been relaxed with DFT. Shades ranging from light (yellow) to dark (brown) indicate the relative heights of the oxygen atoms.**

The ring's empty center and the center of a triangle depression coincide. Thus, the dark spot in STM is explained naturally. The dark vertices of the triangles seen in Figure 15 correspond to heptagon centers. There are two possible orientations of the triangle, corresponding to those of the substituted four-molecule cluster drawn as dark (red) dots in Figure 16a. Triangles of both orientations are observed experimentally in Figure 15a.

Figure 16b makes clear how all three principles are also satisfied. Twelve of the 13 flat-lying H2 O molecules in the √37 unit cell are clustered in a central hexagon with O atoms in atop sites, and another hexagon surrounding it. No H bond is broken. The puzzle of the 30º rotation is resolved because the rotated hexagons consist primarily of H-down molecules, which experience corrugation of the substrate only weakly. Thus, rotation of the H-down region of the wetting phases relative to the central flat H ring is not a serious impediment to formation of the defect structure.

Remaining issues require support from calculations. One is why only the molecules in the central hexagonal ring seem close to the metal surface. Another is whether the strain-energy price is prohibitive of accommodating the di-interstitial with relatively short inter-$H_2O$ separations at the borders of the depressions.

We addressed these concerns with first-principles binding-energy calculations, and STM image simulations, using the VASP DFT code [73, 74], the Perdew-Burke-Ernzerhof (PBE) version of the generalized gradient approximation [75], and the projector-augmented wave approximation [76, 77]. We modeled the Pt(111) substrate as a 3-layer slab, with water adsorbed on top of it.

Atoms of the lowest metal layer were fixed in theoretical bulk Pt relative positions ($a_{PBE}$ = 3.98 Å); all other atom positions them were relaxed till forces on them were <0.045 eV/Å in magnitude. For accuracy, we used a 700 eV plane-wave basis cutoff, and sampled the √37 × √37-R25.3º surface Brillouin zone with a 3 Â 3 set of equally spaced k vectors. We accelerated electronic relaxation through Methfessel-Paxton Fermi level smearing [147] (width = 0.2 eV). Neugebauer-Scheffler [78] corrections canceled unphysical fields associated with the periodic slab repeats. Generally, dangling H bonds were started pointing toward the metal prior to optimization. Flipping them up always increased the system energy.

The relaxed √37 unit cell with the di-interstitial is shown in Figure 16b. This structure is superimposed on the STM images in Figure 17(a and b). A STM image simulation based on the DFT electron density is shown in Figure 17c. Plotted there, for comparison with STM images acquired with a 0.2 V bias, is the height above the Pt surface of a constant electron-density contour ($3.2 \times 10^{-7}$ $e$/Å$^3$) attributable to electrons from the Fermi level to 0.2 eV below.

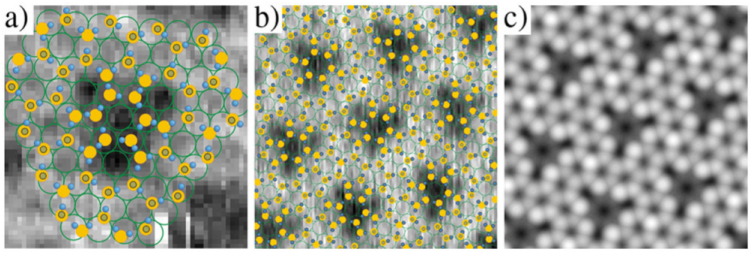


**Figure 17. Overlay of the molecular model on STM images of (a) a single triangle and (b) an ordered √37. Panel (c) shows a simulated STM image based on DFT charge densities.**

There are 26 $H_2O$ molecules in the unit cell, with 12 in a central hexagon and another hexagon surrounding it. Remarkably, the molecules of the outer hexagon are rather high, consistent with experiment, and tilted out of the surface plane. They thereby bridge the central hexagon and the remaining water molecules, whose dangling H bonds force them to lie higher. The result is that the O-Pt separations of the central molecules optimize to just 2.24 Å. That betokens strong binding, compared to the 2.68 Å we find for the flat-lying molecules in a classic √3 H-down bilayer (or 2.87 Å for H-up). Notice that the O-O distances in the "575757" defect projected onto the surface plane are shorter than those in the surrounding hexagons. This result is consistent with experiment, as the overlay in Figure 17a shows. Also consistent is that all the O atoms away from the low hexagon lie roughly at the same height above the metal (apart from the slightly higher isolated flat-lying molecule).

Note the good correspondence between the simulated image and the STM images of Figure 15, and, in particular, of the size of the dark triangles. The charge contour shown has the H-down $H_2O$ molecules 0.6 Å above the central flat-lying molecules and 1.5 Å above clean Pt, roughly consistent with experiment. Contours of smaller charge density would likely improve agreement but are problematic for DFT.

So, DFT shows that the relaxed defect structure agrees with experiment. But is it lower in energy than competing structures with no defect? Indeed yes: our calculations for the di-interstital

arrangement yielded a lattice binding energy of 0.55 eV/$H_2O$ (Footnote: "Lattice energy" excludes zero-point contributions). This is higher (i.e., more stable) than for any hexagonal $H_2O$ network we have considered. Specifically, it is 0.10 eV higher than for the conventional √3 H-down bilayer and 23 meV per molecule higher than for a version of the moiré structure proposed by Glebov et al. rearranged so that as many as possible of its flat-lying water molecules occupy near-atop sites.

Importantly, the di-interstitial structure has much lower energy than arrangements in conflict with even just one of the three constraints mentioned earlier. For example, if the H-bond arrangement is altered so that six H-down (instead of flat-lying) molecules surround the central hexagonal ring, violating the clustering constraint, the energy rises by 34 meV per water. For another, if the dark triangles are attributed to tetravacancies [148], there are six broken H bonds per unit cell (see Figure 16a, middle panel). The binding energy of such a low-coverage arrangement is accordingly 70 meV per molecule worse than that of the di-interstitial structure.

Consider now the higher coverage √39 phase, which exists in equilibrium with 3D ice islands [68, 149]. A √39 unit cell incorporating the "575757"defect is shown in Figure 18a. Slightly denser than the √37 (26 over √37), as required, it contains 28 water molecules over 39 Pt atoms. There are now two flat-lying molecules not directly linked to the "575757" structure. Positioning them together, as in Figure 18a, allows one to relax into an energetically preferred atop site.

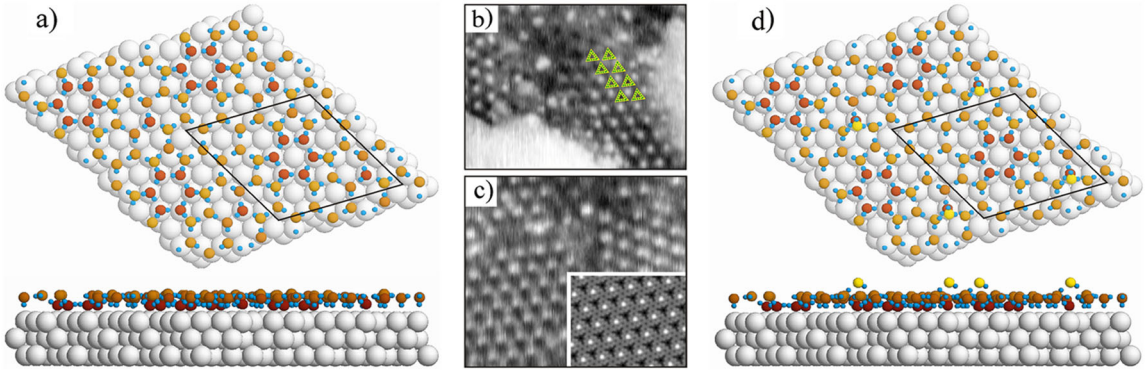


**Figure 18. (a) Schematic of the √39 structure. (b) STM image showing the coexistence of 3D crystallites with √39 (22 nm × 17 nm, $V_{tip}$ = 0.5 V, $I_t$ = 5 pA). Yellow triangles mark the triangular depressions. (c) STM image showing the two rotational domains (20 nm × 17 nm, $V_{tip}$ = 0.5 V, $I_t$ = 1 pA). (d) Relaxed configuration of a water molecule added on top of the structure in (a). Inset in (c) is an STM image simulation of the structure containing this molecule.**

DFT calculations for this phase imply an adsorption energy just a few tenths of a meV below that for the √37 and, again, significantly higher than the competing moiré proposed by Glebov with 32 molecules per unit cell. The relaxed configuration (see Figure 18a) is similar to the √37, except that the isolated flat-lying water molecule over the atop site now lies low, only 2.21 Å above the Pt.

It is more difficult to compare this computed structure directly with STM measurements because the conditions for high-resolution imaging destroy the 3D islands that coexist with the √39 phase

[32, 144], scattering their water molecules nearby. The scattered water molecules tend to obscure the wetting-layer structure. Still, we did obtain images with √39 periodicity and dark triangular features, as shown in Figure 18(b and c). Notice the adjacent footprints of 3D islands, disrupted during scanning.

Between the triangular depressions in the STM images, note bright areas of various sizes in apparent conflict with the model of Figure 18a, which has a low-lying molecule in the same position and thus ‘‘should be’’ dark (Footnote: Such low-lying flat molecules explain the small dark features away from the triangular depressions in Figure 15a). Might they represent water molecules adsorbed on top of the 39 arrangement of Figure 18a, near its isolated flat-lying molecules? To check (cf. Ref.[150]), we optimized such ‘‘2nd-layer’’ molecules. In the postrelaxation configuration of Figure 18d, their adsorption energy, 0.55 meV, equals that of the first layer, suggesting they could be part of the equilibrium structure that coexists with the 3D islands. (Experimentally, it is difficult to distinguish an equilibrium feature from one produced by 3D island disruption.) The simulated image in the inset of Figure 18c, made by integrating the DFT charge density from the Fermi energy to 0.5 eV below, and plotting a charge contour of $5\times10^{-7}$ $e/\text{Å}^3$ , reproduces the general appearance of the bright features seen experimentally.

In assessing the foregoing, note that although our DFT calculations do provide reasonable STM image simulations, and do account for the low energies of the observed structures compared to the classic bilayer, they do not yet explain two-dimensional wetting [149]. Specifically, the calculated lattice energy per molecule in the wetting layer is some 90 meV less than for bulk ice. Thus, $H_2O$/Pt(111) is yet another example showing that the accuracy of today’s DFT needs improvement before we can rely on it to predict water-solid interactions.

### *3.1.5 Conclusions*

Notwithstanding this caveat, we have offered herein evidence that the first wetting layer on Pt(111) is a mixture of 5-, 6-, and 7-membered rings of water molecules, favored by the energy gained when a perfectly H-bonded array of water molecules allows a significant fraction of them to lie close to 1st layer metal atoms. This structural difference compared to the classic, icelike bilayer has consequences for further water growth; notably, it suggests that 3D islands will not grow on top of the wetting layer, without substantial molecular rearrangement. More broadly, it underlines the importance of directly characterizing the first stages of water adsorption before claiming that one understands how water interacts with solids [22].

### *3.1.6 Acknowledgements*

This work was partially supported by the DOE Office of Basic Energy Sciences, Division of Materials Sciences and Engineering, under Contract No. DE-AC04-94AL85000. P.J.F. acknowledges useful discussions with the group of T. Michely and the receipt of high-resolution STM images of the √37 and √39 phases after the model presented here was developed.

## 3.2 Lattice Match in Density Functional Calculations: Ice Ih *vs.* -AgI

The following was published under the same title; see: P.J. Feibelman, *Phys*. *Chem*. *Chem*. *Phys*. **10**(32): 4588–4691 (2008).

### *3.2.1 Abstract*

Density functional optimizations of the crystal parameters of ice Ih and -AgI imply lattice mismatches of 4.2 to 7.9%, in a survey of eight common, approximate (non-hybrid) functionals, too large to allow a meaningful contribution from Density Functional Theory to the discussion of the significance of lattice match in ice nucleation.

### *3.2.2 Introduction*

Based on wide experience, Density Functional Theory (DFT) calculations are expected to yield binding energies of modest accuracy (in Generalized Gradient Approximations) [75, 151-160] or worse (in the Local Density Approximation [161]), while optimized, condensed-matter structures are predicted in good correspondence with nature. This, for instance, is how one justifies performing Quantum Monte Carlo calculations—designed to incorporate many-electron interactions very accurately—with atoms in sites predetermined *via* DFT optimization [162].

Depending on the intended application, however, the presumption of reliable DFT structures can be inappropriate. A good example is heterogeneous epitaxy, where the film thickness beyond which pseudomorphic growth no longer occurs is strain-dependent [163]. This relationship means that the calculated stability of an epitaxial film must differ from reality to the extent that the theoretical lattice mismatch does—a rather stringent, though largely disregarded, test of DFT structural predictions.

An example for which, by definition, an accurate account of lattice mismatch is indispensable is an assessment of Vonnegut's decades-old suggestion that AgI smoke might provide nuclei in clouds for rain-inducing ice crystallization (Figure 19) [40]. This suggestion was based on a survey of crystal parameters, which revealed a mismatch of only about 1% between the lattice constants of hexagonal -AgI, and of ice Ih. Post experiments in the field, it has been vigorously debated whether cloud seeding with AgI actually does induce rainfall [164]. Whether or not, the undisputed laboratory observation that AgI nanoparticles are very effective ice nuclei remains to be understood [40].


**Figure 19. Bernard Vonnegut making a silver iodide smoke c.a. 1949**

The need for improved understanding is suggested by literature up to the present, where the role of lattice match is both discounted [33, 165] and underlined [166]. Can DFT calculations help evaluate its relative importance, compared to surface chemistry, or the existence of key surface defects [144]? Such a quest only makes sense if DFT lattice mismatches conform reasonably accurately to those in nature.

Adopting the widely used Perdew, Burke, Ernzerhof (PBE) Generalized Gradient Approximation for the DFT calculations [75], however, the predicted ice Ih lattice constants (see below) are $a$ = 4.42 and $c$ = 7.24 at 0 °K, compared to the experimental [167] 4.497 and 7.321 , at 10 °K. Thus, at low temperature, where standard DFT calculations provide answers straightforwardly, the PBE ice Ih lattice constants are 1.6 and 1.2% too small compared to nature. The PBE functional lattice constants of AgI, however, are $a$ = 4.68 , and $c$ =7.66 , each 2.0% *greater* than the corresponding experimental value [168]. Thus, in the PBE universe, the low temperature epitaxial mismatch of ice Ih and AgI is 5.9%, in both $a$ and $c$. Had Vonnegut seen a mismatch of this magnitude, he would certainly have looked for an alternative to AgI.

Instead of concluding that the PBE functional is therefore unhelpful for understanding the role of AgIs lattice parameters in ice nucleation, one might wonder if the strain energy cost of compensating for the DFT mismatch is small enough, because ice is soft [The bulk modulus of polycrystalline ice is 0.89 GPa, at 257 °K, according to Ref. [169]], that pseudomorphic growth will remain favorable, *i.e.*, that mismatch is not structurally or energetically important for ice, and the search for a lattice-matched ice nucleating surface is meaningless. This idea, however, begs the question, favorable compared to what?—to which water adsorption on Pt(111) provides a cautionary answer from nature. Experimentally, 3 times the spacing of Pt atoms on the Pt(111) surface exceeds the $a$ = 4.5 lattice repeat of ice Ih(0001) by 6.6%. Still, diffraction measurements show that the first layer of $H_2O$ does not form the 3×3–R30° structure one would expect if relatively easily distorted H bonds compensated the mismatch. Instead the wetting layer on Pt(111) is rotated, giving rise to a 39 × 39–R16.1° diffraction pattern [68-70].

At a minimum, accordingly, one should be aware of the artificial lattice mismatches produced by approximate DFT functionals, and I therefore provide in what follows, a survey of the lattice constants of ice Ih and of hcp -AgI, as predicted by a sample of eight currently popular functionals. Hybrids [170] are not among them, on the grounds of prohibitive computer cost in addressing large problems. A similar survey, for ice only, was published over a decade ago by D. R. Hamann, based on use of an adaptive-coordinate method [171]. Since then, several potentially improved functionals have been introduced. They, together with the general importance of water–materials interactions, motivate the present update.

The comparison to calculations of the AgI lattice constants shows that the DFT mismatch of 6% to ice Ih is not just a property of the PBE functional, but comparable to what is found with most other GGA implementations. If we wish to contribute to resolving questions on how AgI does and does not nucleate ice, we will therefore need a functional more faithful to nature.

In the next section of this article, I review the numerical methods used to optimize structures and energies. Results are presented for ice Ih in section III, and compared to those for AgI in section IV.

### *3.2.3 Numerical Methods*

Structures and energies reported herein were obtained by applying the VASP total energy computer code [71, 72], with electron–nucleus interactions treated in the projector augmented wave (PAW) approximation [76, 77]. Eight approximate density functionals were considered, including the Ceperley–Alder, Local Density Approximation (see Ref.[161], as parameterized by Ref. [159]), (CA-LDA), the new PBEsol [158] and AM05 [157] functionals, the more widely used Perdew–Wang91 (PW91) [152, 153] and Perdew–Burke–Ernzerhof (PBE), [75] Generalized Gradient Approximations, the BLYP functional [151, 160] favored by many who work on water-related problems, and lastly, the RPBE[156] and revPBE [155] functionals. The ability to use all these functionals is a feature of version 5 of VASP, soon to be released widely, which recalculates the exact core-valence exchange corresponding to the selected functional at run time [172].

Ice-Ih was modeled using Hamanns, proton-ordered, twelve water-molecule unit cell, and corresponding four special-point sample [173] of the irreducible wedge of the corresponding Brillouin zone (the IBZ) [171]. For the sake of high accuracy in the face of short O–H bonds, I used the hardest PAW potentials available for H and O atoms, optimized for a plane wave basis cutoff 700 eV, and then optimized ice crystal geometries using an actual cutoff of 1400 eV, more than large enough to provide meaningful values of the stress tensor. I relaxed atomic positions for each set of lattice constants, $a$ and $c$, until all forces were less than 0.005 eV $^{-1}$. Using computed stress values, I surrounded the minimum energy lattice constants in the $a$–$c$ plane with 9 to 17 points, then located the parameters of the lowest energy cell *via* a polynomial fit to the computed energies. For each functional, I verified that the predicted best values of $a$ and $c$ yielded a lower energy than any already computed, and that the predicted lowest energy for the 12-molecule cell agreed with the value produced by the VASP code for the same $a$ and $c$ to 0.2 meV or better.

In the AgI optimizations, I used a primitive wurtzite-structure cell, with lattice vectors $a = (a,0,0)$, $b = a(-1/2, 3/2, 0)$, and $c = (0,0,c)$, Ag atoms at the origin and at $(2a + b)/3 + c/2$, and I atoms at $(4 + \zeta)c/8$ and $(2a + b)/3 + c\zeta/8$. The PAW potentials used for Ag and I atoms were optimized for plane wave basis cutoffs 250 and 176 eV. The plane-wave basis set cutoff actually used for AgI was 400 eV, again chosen rather large to produce helpful stress tensor values. In a convergence test with the PBE functional, increasing the cutoff to 500 eV lowered the calculated cohesive energy of the AgI crystal by 1 meV, without any appreciable geometric effect. The Brillouin zone was sampled with a $6 \times 6 \times 2$ set of equally spaced $k$-vectors, amounting to 12 points in the IBZ. Optimization of the values of lattice constants $a$ and $c$ was carried out in the same manner as previously for Ice Ih. The structural parameter, $\zeta$, always optimized to a value near one, consistent with tetrahedral bonding.

### *3.2.4 Ice Ih Lattice*

Optimized lattice parameters and lattice energies of Ice Ih for the various functionals are compared to experimental values in Table 2. The table shows that whereas the calculated $c/a$ ratio is within a few tenths of a percent of experiment in all cases, the computed lattice energy and volume per water molecule vary widely. The volume per $H_2O$ of the CA-LDA ice lattice is some 21% too small, while using the RPBE functional it is almost 8% too large. Correspondingly, the CA-LDA Ice Ih lattice energy is 80% larger than the experimental value, while in the RPBE world it is 30% too small. The calculated lattice energy is best when the PBE functional is used, only 5% larger than experiment, but the volume per $H_2O$ is closest to experiment, only 2.8% too large, with the BLYP functional. Given that PBE and BLYP are among the oldest GGA functionals examined, one must conclude that inclusion of ice Ih lattice constants in the suite of tests used to judge whether a new functional represents an improvement would be a good idea.

**Table 2. For Ice Ih, and a suite of approximate density functionals, a comparison of the calculated ratio of lattice constants *c* and *a*, the volume of the unit cell per water molecule (at 0 °K) and the lattice energy (L.E.), defined as sublimation energy with no correction for the quantum nature of the proton. Experimental, low temperature values of these quantities are also given.**

| Functional | c/a | Volume ($Å^3$)/$H_2O$ | L.E. (eV)/$H_2O$ | Ref. |
|---|---|---|---|---|
| CA-LDA | 1.632 | 25.47 | 1.10 | [159, 161] |
| PBEsol | 1.633 | 27.74 | 0.79 | [158] |
| AM05 | 1.639 | 28.62 | 0.66 | [157] |
| PW91 | 1.635 | 30.39 | 0.68 | [152-154] |
| PBE | 1.636 | 30.65 | 0.64 | [75] |
| BLYP | 1.635 | 32.95 | 0.52 | [160] |
| revPBE | 1.635 | 33.76 | 0.46 | [155] |
| RPBE | 1.635 | 34.48 | 0.47 | [156] |
| Experiment (10 °K) | 1.628 | 32.05 | 0.61 | [144] |

A common criticism of DFT calculations involving closed shell systems, including crystalline $H_2O$, is that approximate functionals treat Van der Waals (VdW) interactions poorly [174]. GGA functionals, in particular, are thought to underestimate VdW attraction [175, 176]. Table 2 suggests that a subtler picture is needed to explain the deficiencies of DFT regarding ice structural energetics. The obvious problem is that several of the GGA functionals produce ice Ih lattices that are too dense and, correspondingly, lattice energies that are too large. Accordingly, correcting them by adding a more attractive dispersive term will only exacerbate the poor comparisons to experiment. The BLYP, revPBE and RPBE functionals are more hopeful from this perspective. Adding an attractive correction in these cases would improve agreement between the calculated and experimental lattice volumes and energies.

For completeness, I compare the present results to those of [171] in Table 3. The newly calculated lattice volumes are 3 to 4% smaller, and the lattice energies are 10 to 20% larger. In the PW91 case, improved adaptive coordinate methodology [177] has essentially eliminated the discrepancies, and the same can be expected for the other functionals [178].

**Table 3. For Ice Ih, and three approximate density functionals, a comparison of the volume of the unit cell per water molecule (at 0 °K) and the lattice energy (L.E.), defined as sublimation energy with no correction for the quantum nature of the proton. Experimental, low temperature values of these quantities are also given.**

| Functional | Vol. ($Å^3$)/$H_2O$ (Ref.[171]) | Vol. ($Å^3$)/$H_2O$ (Present work) | Vol. ratio | L.E. (eV)/$H_2O$ (Ref.[171]) | L.E. (eV)/$H_2O$ (Present work) | L.E. ratio |
|---|---|---|---|---|---|---|
| CA-LDA [159, 161] | 26.43 | 25.47 | 1.038 | 0.99 | 1.10 | 0.90 |
| PW91[152-154] | 31.35 | 30.39 | 1.032 | 0.55 | 0.68 | 0.81 |
| PBE [75] | 31.82 | 30.65 | 1.038 | 0.53 | 0.64 | 0.83 |

### *3.2.5 Ice Ih Lattice Match to AgI*

In Table 4, I survey the computed Ice Ih and AgI lattice constants, and compare them to experimental values. The DFT results all pertain to 0 °K, but this makes little difference compared to the systematic errors incurred by using any of the eight functionals. The reason is that neither the AgI nor the ice Ih lattice constants change by more than a fraction of a percent between 0 and 273 °K. AgI is celebrated for its negative thermal expansion. But the effect between absolute zero and 270 K is very small, less than 0.1% in the *c* direction [168]. Ice Ih expands by about 0.5% between 10 and 265 K [144]. Thus, the experimental mismatch between AgI and ice Ih at 0 °C is 1.6% in the lattice constant [165], whereas, as quoted in the last row of the table, it is 2.2% at low temperature.

**Table 4. For Ice Ih and -AgI, and for a suite of approximate density functionals, a comparison of calculated lattice constants, *a*, and *c*/*a* ratios. Experimental, low temperature values of these quantities are also shown.**

| Functional | a(ice) | a(β-AgI) | Mismatch | c/a (ice) | c/a (β-AgI) |
|---|---|---|---|---|---|
| CA-LDA [159] | 4.16 | 4.50 | 7.9% | 1.63 | 1.64 |
| PBEsol [158] | 4.28 | 4.56 | 6.4% | 1.63 | 1.64 |
| AM05 [157] | 4.32 | 4.69 | 6.2% | 1.64 | 1.64 |
| PW91 [152-154] | 4.41 | 4.68 | 6.0% | 1.64 | 1.64 |
| PBE [75] | 4.42 | 4.68 | 5.9% | 1.64 | 1.64 |
| BLYP [151] | 4.53 | 4.83 | 6.6% | 1.64 | 1.63 |
| revPBE [155] | 4.57 | 4.77 | 4.3% | 1.64 | 1.64 |
| RPBE [156] | 4.60 | 4.80 | 4.2% | 1.64 | 1.64 |
| Experiment | 4.497 (10 °K) (Ref.[167]) | 4.594 (30 °K) (Ref.[168]) | 2.2% | 1.628 | 1.635 |

Table 4 implies that none of the approximate functionals in common use is well-suited for a study of the role of lattice match in ice nucleation. The best case, the RPBE functional [156], misses the experimental lattice match by almost a factor of two, but, as reported in Table 2, produces an ice lattice energy too small by 0.14 eV (or five times the Boltzmann constant times the melting temperature of ice). The very latest functional, PBEsol [158], does slightly worse than the widely used PBE, producing a lattice mismatch too large by about a factor of three. Given the vast importance of water–materials interactions in technology, in biology, and in atmospheric and geophysical phenomena, one awaits the development of a functional that treats such interactions faithfully with a measure of impatience.

### *3.2.6 Acknowledgements*

I am grateful to A. Michaelides for encouraging me to undertake this survey, and to G. Kresse for supplying a pre-release version of VASP.5.1. I am pleased to acknowledge A. E. Mattssons timely incorporation of the AM05, revPBE and PBEsol density functionals into VASP.5.1, and thank T. R. Mattsson for numerous helpful discussions. VASP was developed at T. U. Wiens Institut für Theoretische Physik.

## 3.3 Large Scale Molecular Dynamics Simulations of Vapor Phase Lubrication for MEMS

The following excerpts are from a manuscript that has been accepted for publication under the same title; see: Lorenz, C.D., M. Chandross, and G.S. Grest, *Journal of Adhesion Science and Technology* (2010), in press.

### 3.3.1 Abstract

While alkylsilane monolayers reduce both adhesion and friction in MEMS, experiments and simulations have shown that they are easily damaged by momentary contact even at low loads. Vapor phase alcohols appear to provide a potential solution to this problem, reducing friction in MEMS with no noticeable wear, and allowing devices to run for billions of cycles without failure. The underlying mechanisms behind both the reduction in friction as well as the healing of damage are however unclear. We report on the results of large scale molecular dynamics simulations aimed at understanding the tribology of vapor phase alcohols in contact with amorphous silica substrates. The healing mechanism is investigated by simulating asperity contact with a model AFM tip in contact with a monolayer of propanol on an amorphous silica substrate. We find that because of the low vapor pressure, alcohol molecules removed by shear contact remain close to the substrate, moving around the contact region to replenish molecules removed from the damage site. For comparison, the tribology of propanol and water confined between two opposing flat silica surfaces is also studied.

### 3.3.2 Introduction

The impact of microelectromechanical systems (MEMS) on all sectors of manufacturing has been enormous. MEMS are currently in use in car airbags, digital light projectors, ink jet printers, accelerometers in video games, cell phones and digital cameras, and many other consumer and industrial products. There are still, however, no commercial products with MEMS devices that contain contacting, moving parts. The ma jor, unresolved issue is the frictional contact between the silica substrates that are generally used to fabricate MEMS.

MEMS can be (and indeed have been) made out of many different materials, but the most popular by far is silicon, both because of the far-reaching infrastructure already in place for manufacturing and processing silicon, but also because of the attractive potential of including the actuation from a MEMS device on the same chip as the logic circuit that controls it. Silicon, however, has many undesirable material characteristics. Silicon oxidizes upon exposure to air, generating a highly reactive, hydrophilic oxide layer (hereafter referred to as silica), which is primarily responsible for the adhesion and friction issues that are so problematic in MEMS devices with contacting, moving surfaces. Because the surface-to-volume ratio is small in MEMS devices, surface forces dominate. At a separation of approximately 10 nm, van der Waals interactions between two smooth μm pieces of silicon are approximately two orders of magnitude greater than the typical restoring forces that MEMS actuators can provide [179].

Silicon MEMS initially had failure issues due to parts sticking upon release (stiction) because of the presence of residual water in the system. This adhesion problem in MEMS was essentially solved with the use of alkylsilane self-assembled monolayers (SAMs), which passivate the silica surface and provide hydrophobic coatings. This allowed parts to be freely separated, and even MEMS with intermittent contact could operate e*ff*ectively. While alkylsilane SAMs are also reasonably e*ff*ective boundary lubricants [180], providing a far better frictional response than bare silica, the unfortunate reality is that they are an exceptionally fragile lubricant layer, and are easily damaged with both normal and shear contacts of even nominal loads.

Recent experimental work with a MEMS tribometer has shown that changes to the physical and chemical nature of surfaces occurs almost immediately after both normal and sliding contacts [181]. With repeated impact loading at a contact velocity of 2 mm/s at 750 nN applied load, the coating was severely damaged within 50,000-100,000 cycles after an initial run-in period that lasted from 0 to 100,000 cycles. For sliding contacts degradation was seen to occur extremely quickly, after just 800 cycles with the same applied load.

Our previous simulation work has demonstrated that normal loads on the order of 50 nN are sufficient to remove alkylsilane chains from the monolayer with a single insertion of model atomic force microscope (AFM) tip with radius of curvature of 10 nm. Under shear, the performance is worse with less than 10 nN applied normal load necessary to cause severe damage to the monolayer [182]. This damage has been shown both by these simulations and by experiments [183] to be irreversible. Damage provides preferential sites for water adsorption and penetration, which quickly leads to further debonding of monolayer chains [184], indicating that SAMs are not an adequate long-term solution for tribological coatings in MEMS devices.

Recent work, however, has demonstrated that gas-phase alcohols may provide a solution to the friction problem, in that when MEMS devices are exposed to low vapor pressures of short chain alcohols, devices with contacting, moving parts can run for billions of cycles without failure and with no visible wear [185]. While this appears to be a successful lubrication strategy, in order to move towards applications, a number of questions still need to be addressed. Perhaps, most importantly, the fact that there appears to be some mechanism of damage/wear recovery at work in these alcohol systems is still an open issue. Additionally, the mechanism behind the frictional properties of the alcohols is still unknown, and in particular the fact that short chain systems are expected to lead to disordered monolayers with poor coverage does not explain the good tribological response. Experimental studies have also found evidence of long-chain hydrocarbon species forming on the surface in the contact region [185]. It is as yet unknown whether these reactant products are beneficial or even important to the frictional response.

The shear response of confined fluids has been the focus of several simulations studies over the course of the past 20 years. Thompson and Robbins [186, 187] first observed stick-slip motion in atomically thin, fluid films confined between two solid plates. Thompson et al. [188] were the first to observe stick-slip behavior for short chain polymers. Since these pioneering studies, many other studies have been conducted. Bitsanis et al. [189]found that fluid inhomogeneity in a Lennard-Jones liquid causes the shear stress and e*ff*ective viscosity to be smaller than for the homogeneous fluid. Khare et al. [190] found that confined bead-spring polymer fluids exhibit a much stronger tendency for slip at the wall/fluid interface than simple fluids and the amount of slip increased with shear rate. They also found that the amount of slip increases with chain length until it reaches an asymptotic value at approximately the entanglement length of the polymer. Stevens et al. [191] and Jabbarzadeh et al. [192] both studied the shear behavior of a united-atom model of hexadecane and found that as the strength of the wall/fluid interaction increases the amount of slip decreases but the slip always occurs at the wall/fluid interface. Koike and Yoneya [193] studied the effect of molecular chain length on frictional behavior of confined liquid films of bead-spring polymers under shear. They found that at high pressure an interfacial slip appears between the wall and the film, and the shear stress does not depend on chain length, while at low pressure they observed interlayer slip within the polymer film for long chain lengths and that shear stress does depend on chain length. Gao et al. [194] have found that surface roughness

reduces the ordering found in thin hexadecane confined films, which suppresses the solvation forces and results in liquid-like dynamic and response characteristics. They also found that at high shear rates the interfacial layers of the hexadecane films stick to the rough surface causing partial slip within the film, while with flat surfaces the slip occurs at the film boundary with the surface, and there are small shear stresses in the film. Cui et al. [195] found that dodecane films confined between mica surfaces display shear-thinning starting at shear rates that are orders of magnitude lower than the transition point for bulk fluids. In addition, they found that the relaxation time of the confined liquid is seven orders of magnitude larger than that of the bulk fluid. Priezjev and Troian [196] found that at low shear rates, the slip length calculated from velocity profiles of confined bead-spring polymers is strongly correlated to the slip length calculated from Green-Kubo analysis. Also, they found that molecular weight dependence of the slip length of chains of length greater than 10 is dominated strongly by the bulk viscosity. Priezjav [197] studied the shear rate dependence of the slip length in thin bead-spring polymer films confined between atomically flat surfaces and found that there is a gradual transition from no-slip to steady-state slip flow that is associated with the faster relaxation of the polymer chains near the wall.

While all of the previously mentioned studies have focused on the shear response of confined polymers, there have also been several recent simulation studies of the behavior of nanoconfined water under shear. Leng and Cummings [198] have found that hydration layers on mica surfaces with thickness ranging from 0.92 nm to 2.44 nm demonstrate fluidic shear responses, but for what they call ’bilayer ice’ which has a thickness of 0.61 nm they report significant shear enhancement and shear-thinning over a wide range of shear rates. They report that the water molecules in the ’bilayer ice’ have a rotational relaxation time of 0.017 ms and an effective shear viscosity at least 10 times larger than the bulk value. Sendner et al. [142] have studied the dynamics and structure of water under shear near hydrophobic and hydrophilic diamond surfaces. They found that near the hydrophobic surface there is a finite surface slip and near the hydrophilic surface there is no slip but the water viscosity is found to be increased within a thin surface layer. There have been other studies of the shear response of ultrathin films of confined water between crystalline substrates [199-202]. While the main focus of these studies was the structure of the water film under shear, they have also found extremely low friction coefficients for the water, and they have observed stick-slip motion within their systems.

Here we have performed molecular dynamics (MD) simulations of a model AFM tip in contact with an amorphous silica substrate initially coated with a propanol monolayer. Our results show that even for low applied loads, the alcohol molecules are squeezed out of the contact region. This is partially a result of the lack of chemical bonds between the alcohol molecules and the substrate that occur experimentally. The low vapor pressure of the alcohol results in the alcohol molecules strongly favoring adsorption on the substrate. Therefore, molecules that are squeezed out of the contact region by the shearing of the tip move around the tip itself and re-form the monolayer to ”heal” the damage where molecules had been removed. Because our model tips are small and have perfect curvature, it is essentially impossible to trap any small lubricant molecules in the contact region, even for extremely low loads. It is therefore difficult to measure the frictional properties of the propanol molecules using these tip-based simulations as even nominal contact pressures lead to the removal of all lubricant as described above. For larger tips it is possible to trap the alcohol molecules between the tip and the substrate, which could lead to different results. To study this case we also performed MD simulations of propanol confined

between two flat, amorphous silica substrates and compared the results to water, a prototypical short chain, non-hydrocarbon molecule that strongly adsorbs on the silica substrate. We find that the propanol molecules adsorb on the silica in much the same manner as alkylsilane or alkoxyl molecules, albeit without a chemical bond, and provide a reduction in friction with a similar friction coefficient. The calculated friction coefficient of the water system is generally lower than that of the alcohol system, possibly due to the orientation of the water molecules upon shear. We have also recently performed shear simulations of water confined between hydrophilic self-assembled monolayers and found that, because of the low viscosity of the water even under confinement, it is necessary to perform shear simulations at high velocities (in the range of 100 m/s) in order to measure any appreciable shear stresses and friction forces [203]. A similar mechanism is relevant for the low friction forces measured in the simulations here.

In the section, *Model and Methodology*, we briefly review the model and simulation methodology. In the section, *AFM Tip*, we present our results for a model AFM tip in contact with an amorphous silica substrate coated with a monolayer of propanol. In the Section, *Confined Fluids*, we present our results for propanol and water confined between two flat substrates. In the Section, Summary and Conclusions, we briefly summarize our results and discuss future work.

### *3.3.3 Summary and Conclusions*

Our simulations indicate that vapor phase alcohols can indeed provide a robust lubrication solution for MEMS devices. While the introduction of alkylsilanes, in general, had previously solved the adhesion problem in MEMS, they have been shown to be too fragile and easily damaged by asperity contact [204]. Such contact removes chains from the monolayer and these chains are not redeposited. The vapor phase alcohols, on the other hand, provide a similar reduction in adhesion and friction but have the added benefit of redeposition after any damage, likelybecause of the low vapor pressure of alcohol molecules, as indicated by our simulations.

Our work is currently unable to encompass all these effects in a single simulation demonstrating both the tribological properties as well as the response to damage, so instead we focused on a two-prong approach in order to study the practicality of vapor phase alcohols as lubricants for MEMS devices. We studied monolayer damage from asperity contacts through the use of an ideal AFM tip contacting the surface. Rather than a liability, the fact that no lubricant molecules remain trapped in the contact region can, in some ways, be considered an advantage of this aspect of the simulation as it allows us to model the most severe scratch tests possible with total removal of all lubricant molecules. Even in this case we find that because of the extremely low saturation pressure of the propanol, molecules do not enter the vapor but instead accumulate in regions of increased density due to the plowing of molecules from the shearing contact. Density gradients lead to diffusive motion of molecules around the contact region to areas of lower density, which replenishes molecules at the damage sites, allowing for lubrication of future contacts.

The second aspect of our simulation method involves infinite flat plate simulations in which the lubricant molecules are unable to escape the contact region. These simulations allow us to measure the tribological properties of an ideal contact without the added complications of damage or wear. In this case we find that, much like the longer alkylsilane SAMs [205], short

chain alcohols provide quality lubrication with a microscopic friction coefficient of 0.14. Even though these short chains are disordered, our previous findings on the irrelevance of chain length (and the stronger dependence on monolayer order) hold [205], likely because the physical makeup of the two systems is similar in that the head group of the alcohol molecule is located close to the silica substrate while the hydrophobic tails point away, with disorder at the sliding surface.

Experiments have found indication of the formation of long-chain hydrocarbon species upon repeated shearing of silica substrates treated with alcohol vapor [185]. While our simulations are unable to investigate these processes, our initial results tend to indicate that such a process is unnecessary for either the friction or healing mechanisms. Further simulations with reactive potentials would be necessary to study this process and elucidate both the formation and effects of these long-chain hydrocarbon molecules. In addition to the inclusion of chemistry, future directions for this work should include increasing the length of the alcohol molecules, varying the thickness of the confined fluid layers, and combining water and alcohol in the same system to study the effects of competitive adsorption on the tribological response.

### *3.3.4 Acknowledgments*

CL acknowledges the KCL Division of Engineering Start-Up funds for supporting this pro ject. This work is supported by the Laboratory Directed Research and Devel- opment Program at Sandia National Laboratories. Sandia is a multiprogram laboratory operated by Sandia Corporation, a Lockheed Martin Company, for the United States Department of Energy under contract DE-AC04-94AL85000.

## 3.4 Molecular Dynamics Simulations of Water Confined between Matched Pairs of Hydrophobic and Hydrophilic Self-Assembled Monolayers

The paper cited below was partially funded by this LDRD project; however, for brevity, only the reference and abstract are included here:

> Lorenz, C.D., J.M.D. Lane, M. Chandross, M.J. Stevens, G.S. Grest, "Molecular Dynamics Simulations of Water Confined between Matched Pairs of Hydrophobic and Hydrophilic Self-Assembled Monolayers", *Langmuir*, 2009, 25(8), 4535–4542.

### *3.4.1 Abstract*

We have conducted a molecular dynamics (MD) simulation study of water confined between methyl-terminated and carboxyl-terminated alkylsilane self-assembled monolayers (SAMs) on amorphous silica substrates. In doing so, we have investigated the dynamic and structural behavior of the water molecules when compressed to loads ranging from 20 to 950 MPa for two different amounts of water (27 and 58 water molecules/nm$^2$). Within the studied range of loads, we observe that no water molecules penetrate the hydrophobic region of the carboxyl-terminated SAMs. However, we observe that at loads larger than 150 MPa water molecules penetrate the methyl-terminated SAMs and form hydrogen-bonded chains that connect to the bulk water. The

diffusion coefficient of the water molecules decreases as the water film becomes thinner and pressure increases. When compared to bulk diffusion coefficients of water molecules at the various loads, we found that the diffusion coefficients for the systems with 27 water molecules/$nm^2$ are reduced by a factor of 20 at low loads and by a factor of 40 at high loads, while the diffusion coefficients for the systems with 58 water molecules/nm2 are reduced by a factor of 25 at all loads.

# 4. EXPERIMENTAL DISCOVERIES

## 4.1 Superplastic Nanowires Pulled from the Surface of Common Salt

The following was published under the same title; see: N. W. Moore, J. H. Luo, J. Y. Huang, S. X. Mao, and J. E. Houston, *Nano Letters* **9**, 2295-2299 (2009).

### *4.1.1 Abstract*

Superplastic nanowires were formed by touching the NaCl(100) surface with a Au tip in a Transmission Electron Microscope. The nanowires were stretched ≤ 2.2 μm, or 280%, and bent >90º upon compression, when showered with the electron beam. More surprisingly, no dislocations were observable during the elongation due to fast diffusion. Mechanical measurements in humid atmospheres suggest that salt nanowires also form in ambient environments.

### *4.1.2 Introduction*

Superplasticity, or elongation to failure >100%, is a rare material property at room temperature, and even more rare for ionic crystals, having only been seen for a few compounds [206]. That common salt—sodium chloride—can be superplastic at the nanoscale comes as a surprise, because we are accustomed to the tiny salt crystals that we shake onto food, which appear brittle and shatter like glass into small pieces upon crushing. Further, other materials that neck into nanowires far below their melting point have all been metals (e.g., Au, Pb, Al, and Na) [207-210]. Neither have other low-temperature deforming, one-dimensional nanomaterials, such as carbon nanotubes and ceramic nanowires, predicted this behavior in ionic nanowires (e.g., [211-215]). . . Understanding the deformation of NaCl is particularly important for relating laboratory-scale measurements to geotechnical problems [216, 217], and for understanding the physicochemical reactions of sea salt aerosols. The latter have been implicated in problems as broad as cloud nucleation, smog formation, ozone destruction, and triggering asthmatic responses in humans [218, 219].

Atomic-scale imaging has revealed that NaCl crystal surfaces transform dramatically in moist environments (e.g., defect repair for relative humidity, $RH$ > ~10%; step diffusion and hillock growth for $RH$ > ~50%) [220, 221]. These deformations, as well as those that lead to bulk plasticity, are driven by atomic diffusion, which is faster near defects such as steps, kinks, buried dislocations, and the crystal surface itself [222, 223]. For this reason, large, underground rock salt deposits can bend plastically [216, 217, 224]. Here we demonstrate that common salt can also deform plastically at the nanoscale and in the relatively dry, but electron-filled, environment of a Transmission Electron Microscope (TEM), where we pulled superplastic nanowires from the crystal surface. We find that the superplasticity is enabled by atomic diffusion, which allows rapid migration and healing of defects created by strain and by electron irradiation. That the nanowire might be stabilized by a partial reduction of Na+ to Na is also discussed.

### 4.1.3 Materials

Cubic NaCl crystals were purchased from SPI Supplies (Lot#1110821, ~1-$cm^3$, purity > 99.9%). The manufacturer reports the largest impurties to be $CaSO_4$ (< 0.1%), $CaCl_2$ (<0.01%), $MgCl_2$ (<0.01%), and water (<0.01%). Bulk sample water content was found to be in line with the manufacturer's report (<0.010 wt%), as measured by massing a ~1 $cm^3$ sample every 24h while drying at 180ºC until the mass stopped changing within the measurement resolution (±0.003 wt%), after ~5 days.

### 4.1.4 Methods

*IFM sample handling and environment:* Three freshly cleaved (100) crystal faces were evaluated in 3–17 flat locations using a pyramidal diamond tip with an effective (macroscopic) radius of ~1 μm. Our cleaving procedure produced surfaces with local roughness ≤ 1 nm rms as measured over an ~1 $\mu m^2$ area, which was the imaging resolution of the IFM [42, 225] used in these measurements, and therefore an upper bound for the surface roughness. It is not uncommon for simple cleaving to produce atomically-flat surfaces, punctuated only occasionally by steps and other defects (e.g., [220, 221]). Sample air exposure was < 1 min at $RH$ < 30% to minimize atmospheric reactions [226] prior to loading the sample into a measurement chamber filled with filtered, dry $N_2$. Thus, cleaving was performed below the 40% RH threshold for single-monolayer adsorption of water vapor from the atmosphere [227]. To reduce residual surface charge or trace water adsorption, tips and surfaces were grounded and annealed *in situ* at 120±1ºC for 1h. Humidity in the test chamber was stabilized to ±0.1% RH before measurement by adjusting the flow of dry nitrogen through a bubbler filled with deionized water. Humidities were varied over 0.1–60%, below the deliquesce point of the salt surface ($RH$~75%) [227]. All measurements were made at 25ºC.

*Distance definition*: The relative tip-substrate separation ($D$) was normalized by fitting the force-distance curves to the JKR model for the compression of linear elastic solids [228]. For sphere-on-flat contact geometries, this places the reference distance ($D$ = 0) at the substrate surface. However, because the contact may not behave as an ideal solid [229], this choice of distance reference serves only as a rough guide. The JKR model also provided the estimate of the contact (Young's) modulus measured in the normal direction. Precision was ±0.1 nm in $D$ and ±1 nN in force.

*Capillary condensation:* occurs spontaneously in many small pores when water vapor is present in the atmosphere [82]. The Kelvin radius ($r_K$) is often used to describe the thermodynamically stable range of capillary interactions for smooth, hydrophilic surfaces. Specifically, capillary condensation is thermodynamically unstable when the tip-substrate separation is greater than $2r_K$, where $r_K = \gamma V/[R^* T \, \mathrm{Ln}(RH/100)]$, $\gamma$ and $V$ are the surface tension and molar volume of condensed vapor, $T$ is temperature, $R^*$ is the ideal gas constant, and $RH$ is the relative humidity in percent [82]. With these definitions, stable capillary formation at a distance of 7.6 nm (the interaction range measured under dry conditions) would require a relative humidity of 72% if the interaction were driven only by capillary condensation, near the deliquescence point of NaCl [227].

*Lateral force ($F_L$):* was measured by oscillating the tip parallel to the crystal plane and separating the amplitude and phase of the sensor response at the dither frequency (90 Hz) with a lock-in

amplifier [230]. The oscillation amplitude ($l$ = 7±1Å, or about the width of three NaCl pairs) was kept small to minimize surface damage. At $D_C$, the phase lag in the force response was $\theta$ = 6±1º, indicating contact with a material more elastic ($\theta$ = 0º) than fluid ($\theta$ = 90º). The lateral stiffness was defined as $k=(F_L/l)\mathrm{Cos}\theta$. This lateral stiffness was used to estimate a characteristic width for the bridge material, $\lambda \approx 2(4kD_C^3/3\pi E)^{1/4}$, by assuming a cylindrical shape and a modulus equal to that measured for the NaCl surface ($E$=39 GPa) [231]. This estimate ignores that material properties may be size-dependant, and is therefore highly approximate.

*TEM sample handling*: NaCl crystals were cleaved along the (100) direction, glued to a 250 μm diameter Au rod, and inserted into one end of a TEM-STM platform. After cleaving, samples were ~1 mm on each side. The TEM (FEI Tecnai F30) was operated at 100 kV at a dose rate of 1 A/cm$^2$ at room temperature.

*TEM image interpretation*: Surface roughness appears exaggerated due to the transverse imaging direction, which contracts the image (see Figure 22). Dislocations generally create contrasts that are resolvable under our experimental conditions (observations on other materials at similar magnification show clearly resolved dislocations). The entire nanowire showed similar gray contrast; that is, no dislocations could be seen. Unlike the nanowire, the STM tip showed different image contrast, and was also stable under the e-beam, confirming that the nanowire was not composed of the tip material. The Movie M1 shows this strong contrast between the nanowire, which is composed of NaCl and Na, and the Au tip. The Au tip has a much larger scattering power and therefore appears darker in the phase-contrast image.

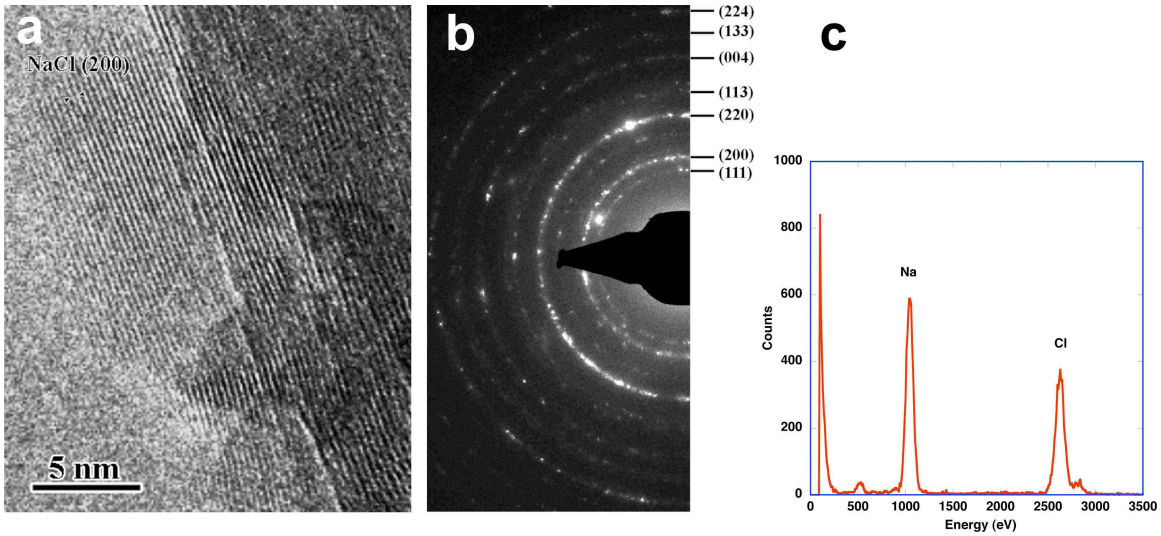


**Figure 20. Structural analyses showing degradation of the NaCl surface into nanocrystals after electron-beam irradiation comparable to those in Figure 22. (a) HRTEM image showing typical NaCl nanocrystal dimensions and lattice parameters (b) Typical EDP indicating polycrystallinity at the NaCl surface (c) A typical EDX spectrum of NaCl nanocrystals, from which a composition of 65% Na and 35% Cl can be determined. Extended irradiation reduced the amount of Cl to as little as 10%, but did not alter the overall crystalline structure. Peaks with energy < 1000 eV are artifacts of the incident electron beam.**

*Nanowire length:* was defined as the portion of the quasi-cylindrical structure that changed diameter, orientation, and/or microstructure, either temporally or "permanently", during the nanowire elongation or compression. This length includes portions of the nanowire that may or may not have changed uniformly with respect to other regions of the nanowire during the deformation, but were nonetheless distinct in structure from the substrate or tip. With these views, nanowires extended the entire distance between substrate and tip. To understand how the initial nanowire length is chosen, one has to understand how nanowires were formed with the TEM-STM experiments. We first pushed the STM probe into the salt surface. Then as we pulled the STM probe back, a "trunk" of NaCl was pulled out. As long as we saw a uniform segment with a nanowire morphology (such as that shown in Figure 22a), we considered that to be the initial state of the nanowire. With our definitions, the estimated elongation is a lower bound for the true elongation.

*Movie M1.mov* is available free of charge via the Internet at http://pubs.acs.org. The movie shows an example of nanowire elongation in the TEM. Image width is 3.1 μm; played at 100× speed (~2 frames/sec.).

### *4.1.5 Results and Discussion*

Initial measurements suggesting nanowire formation were performed with Interfacial Force Microscopy (IFM) [225], a scanning probe technique that avoids the snap-to-contact problem of cantilever force sensors (see Supporting Information). Figure 21 shows an example measurement of the force between a diamond tip and the NaCl surface in dry nitrogen ($RH$ < 0.1%). During

approach, no force was detected until $D_C$, where an attractive force was suddenly born within < 75 ms, or the space of just 0.1 nm. As the tip continued from $D_C$, the attractive force increased linearly until the repulsive compression of the bulk crystal began to dominate near the relative distance, $D$ = 0. The discontinuity at $D_C$, long-range attraction, and linearly increasing force as $D \rightarrow 0$ are established signs of wetting by both fluids [108] and solids [232]. Evidence for a bridge between the tip and crystal surface also comes from the linear, long-range, attractive force during the tip's withdrawal (Figure 21) [108]. Unlike brittle solids, here the bridge stretched monotonically until rupturing at $D_R$ , 14 nm farther than where contact first occurred at $D_C$.

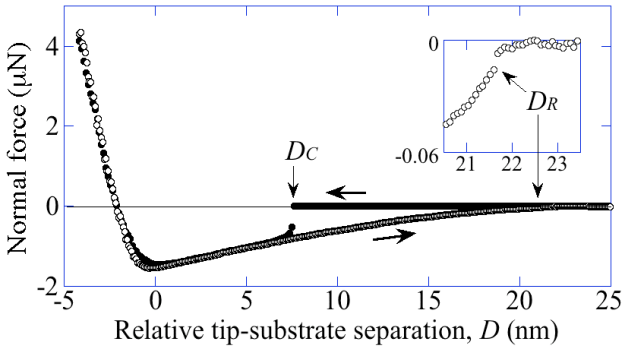


**Figure 21. Example measurement of the normal force between the NaCl(100) surface and a diamond tip as a function of their relative separation, *D*. Nanobridges were created during approach (●) at $D_C$ and ruptured at $D_R$ during retraction (○). Inset shows an enlarged view near $D_R$.**

The behavior of the force is characteristic of both liquid bridges and semi-crystalline necks filling the gap between a tip and surface [108, 232]. Both show a linearly increasing attraction with reduced distance, because of a balance between the capillary pressure and surface energies, including the substrate-tip adhesion [82]. For example, in a similar experiment by Kuipers and Frenken [208], attraction between Pb(110) surfaces and Au or W tips caused local surface melting, directed diffusion and growth of a massive Pb neck between the two surfaces, when the tip was within ~1 nm of the crystal surface. Simulations verified that wetting by the Pb surface atoms caused a meniscus-like attraction (negative force), that increased as the tip approached [233] (c.f. Figure 21). Similarly, it is well known that water vapor in the atmosphere can condense into a liquid capillary between a tip and a surface [82]. However, under our relatively dry conditions ($RH$ <0.1%), the expected height of this capillary is only 0.36 nm, or 21× smaller than $D_C$ = 7.6 nm (see Supporting Information).

Either capillary condensation or solid necking could be rationalized if salt debris on the tip extended the interaction. Such debris would have intriguing properties. Ordinarily, debris on a scanning probe tip either accumulates or is removed by abrasion, resulting in measurements that change over time. Instead, repeatedly touching the salt surface with the IFM tip did not alter the contact distance, the measured forces, or the contact modulus. The latter was 39±6 GPa, within 8% of theoretical values for the bulk crystal [234], again showing no significant accumulation of material at the crystal surface. This consistency implies that salt between the tip and crystal surface must be able to quickly organize into a repeatable structure, and disappear when compressed. That such a deformable bridge might be mostly solid is suggested by the lack of a

humidity dependence ($0.1<RH<60\%$) and by the lateral stiffness measured at $D_C$, $k$=1.5±0.4 N/m. This stiffness could be explained by a string of salt debris just 2.9±1.6 nm, or ~10 NaCl pairs, wide (see Supporting Information).

To show that the NaCl surface is capable of such radical transformation, we conducted similar experiments in a TEM operated at 100 keV with dose rate 1 A/cm$^2$, and fitted with a Nanofactory TEM-STM (scanning tunneling microscopy) platform (see Supporting Information). Pressing and then retracting a Au STM probe into a freshly cleaved NaCl(100) surface produced "debris" that had the shape of nanowires (henceforth called nanowires). Figure 22(a) shows an example of a nanowire, initially ~580 nm long, pulled by a large block of salt adhered to the STM probe. (The STM probe is not shown in Figure 22or Figure 23, but can be seen in Movie M1.) The left side of the nanowire shows a single crystal contrast, and the single-crystal was heavily strained. As we pulled, the nanowire elongated uniformly in its middle (Figure 22(a,b)) until two surface steps with a height of ~30 nm appeared near each of its ends (Figure 22(c)). Upon further pulling, only the segment between these two steps elongated significantly, until a final length of ~2190 nm was reached without breaking. We could not pull the nanowire farther, owing to the manipulator's limited range; consequently, the elongation of ~280% is a lower bound.

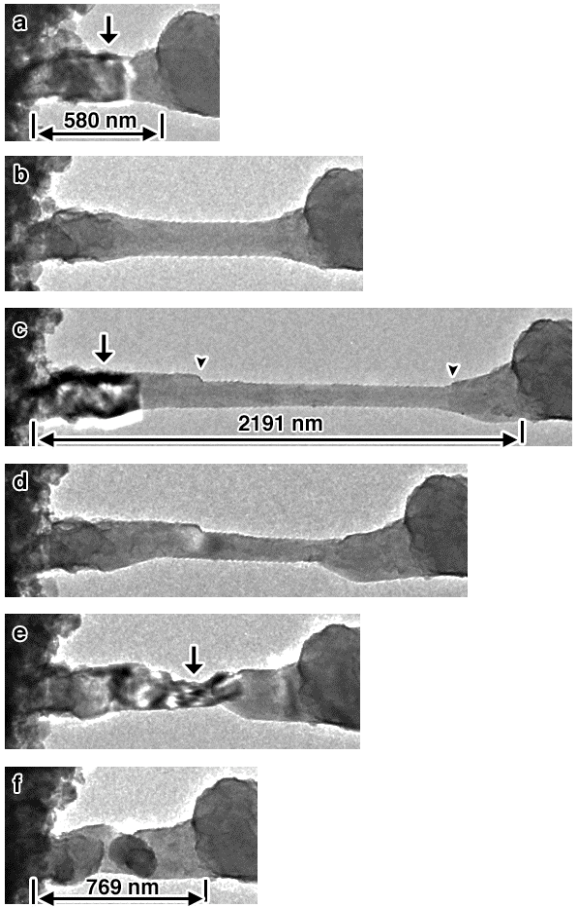


**Figure 22. Time-lapsed TEM images showing superelongation (a→c) and compression (c→f) of a nanowire. The time lapse from a→f is 0s, 256s, 502s, 583s, 684s, and 744s, respectively. The Au STM tip (not shown) is adhered to the NaCl grain at the right side of these images (see Movie M1 in Supporting Information). The nanowire was elongated from a length of 580 nm (a) to 2191 nm (c). The average tensile and compression strain rates are $5.5 \times 10^{-3}$ $s^{-1}$ and $2.4 \times 10^{-3}$ $s^{-1}$, respectively. Arrowheads point to examples of steps on the nanowire surface. Arrows mark crystalline contrast. Roughness of the NaCl surface (left) appears exaggerated by the transverse imaging direction, which contracts the image.**

Although the superelongation reduced the nanowire's diameter from 210 nm (Figure 22(a)) to 100 nm (Figure 22(c)), its volume actually increased by 75%. This increase in volume again indicates transport of NaCl to the nanowire. Atomic flow is necessary to explain the crystalline contrast that we frequently saw (e.g. Figure 22(c)), which may arise from deformation-induced recrystallization. Those recrystallized areas appear heavily strained; however, during elongation we did not see dislocation generation or propagation, as the nanowires showed uniform gray contrast. If there was stable dislocation activity during the elongation, one should see strong diffraction contrast at our imaging conditions. Dislocations may have nucleated and vanished too quickly to be seen with TEM, e.g., as occurs during the plastic extrusion of Au nanocrystals from graphitic capsules, because of fast atomic diffusion [235, 236]. As we pushed the STM probe back, the nanowire contracted (Figure 22(d,e) until the final stages, where it buckled more than

90º (see overlapped nanowire in Figure 22(f)). During this compression, crystalline contrast appeared intermittently (Figure 22(e)), also pointing toward atomic diffusion as a deformation mechanism. The deformations described above can be seen more clearly in a TEM movie (M1), available as Supporting Information.

We also found that electron beam irradiation enhances the ductility. It is well known that electron irradiation introduces a variety of defects, and can disintegrate bulk NaCl into nanocrystals [237, 238]. Consistently, NaCl nanocrystals were formed at the edge of the initially smooth bulk samples after imaging for a few minutes. The beam may also enhance ductility by warming the nanowire. To minimize these effects, we repeated the same experiments without the electron beam. After forming a nanowire, we blanked the beam and pulled the nanowire farther, taking images by intermittently turning on the beam for only ~1 s every ~5 min. Even without the electron beam, superelongation was still observed. Figure 23 shows a nanowire that was elongated from ~210 nm (Figure 23(a)) to ~440 nm (Figure 23(b)), a total elongation of ~110%. A crystalline contrast was also observed during the elongation. The nanowire necked before failing, characteristic of ductile fracture.

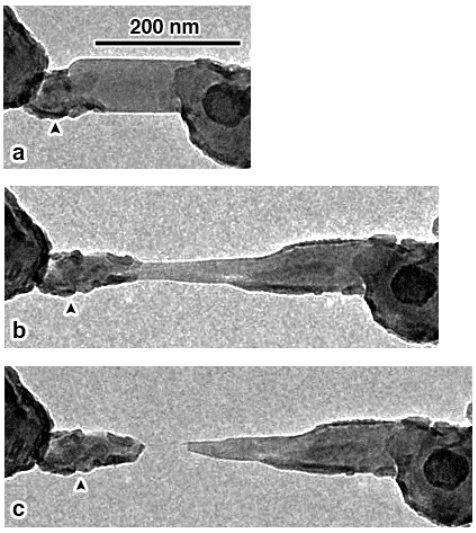


**Figure 23. TEM images showing nanowire superelongation when the electron beam was blanked during the pulling process. The time elapse from a→c is 0s, 420s, 480s, respectively. The Au STM tip (not shown) is adhered to the NaCl grain at the right side of these images. The strain rate is $2.6 \times 10^{-3}$ $s^{-1}$.**

To measure the composition of the nanowire, electron energy loss spectroscopy (EELS) was conducted before and after pulling. Figure 24(a,b) shows superelongation of another nanowire that elongated ~256% with the e-beam on; Figure 24(c) shows the area where the EELS spectra were collected. Figure 24(d,e) shows the EELS Na-L2,3 and Cl L-2,3 edges. The Na-L2,3 and Cl-L2,3 edges from the pristine NaCl region agrees excellently with that from a standard EELS spectra [239]. The results show that the nanowire contains both Na and Cl before and after pulling; however, with prolonged elongation, the Cl content continues to decrease. Furthermore, the Na-L2,3 edge from the superelongated nanowires shows additional peaks (e.g. peaks e, f, and g in Figure 24(d)) in addition to the Na peaks, as might arise from plasmon oscillation or Na

precipitation. Similarly, energy dispersive X-ray spectroscopy (EDX) shows that the Cl content can be less than 10% in the superelongated nanowires. Because the nanowires were not stable under higher electron fluxes, we were unable to probe its atomic structure using high resolution TEM (HRTEM). However, applying HRTEM and EDX to larger areas of the crystal substrate under similar irradiation revealed nanocrystals with grain sizes <20 nm and crystal structures recognizable as NaCl, but with a ~23% reduction of surface Cl (Figure 20).

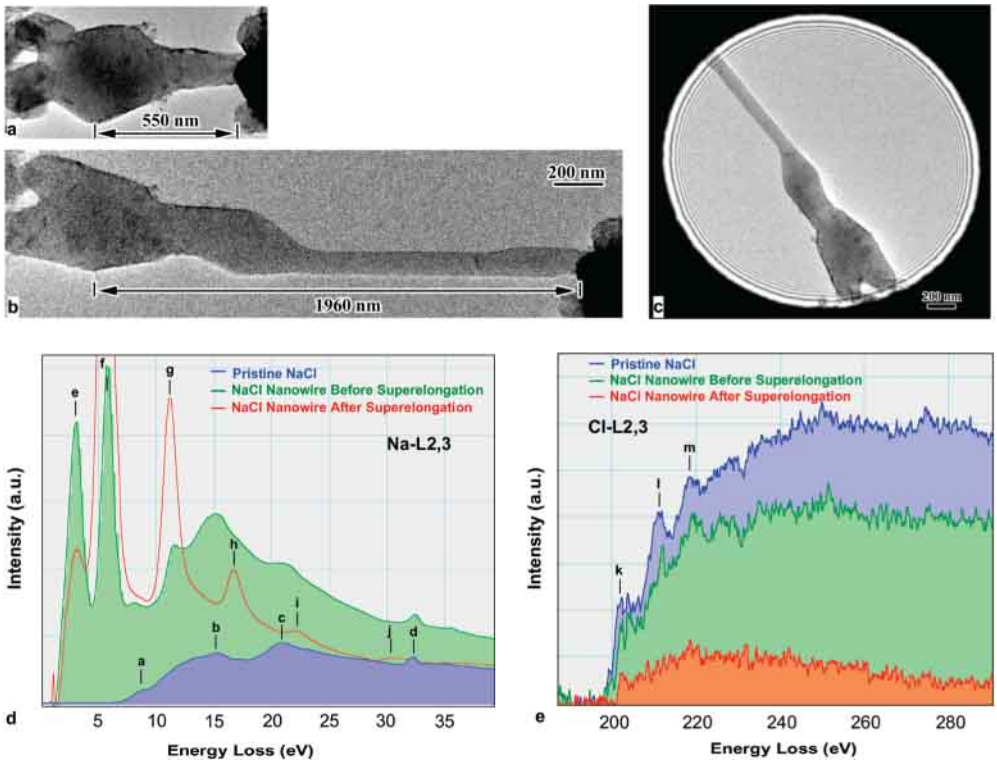


**Figure 24. (a,b) TEM images showing superelongation (~256%) of a nanowire. (c) TEM image showing the area where EELS spectra were collected. (d,e) EELS spectra of the Na-L2,3 edge and Cl L2,3 edge from the pristine NaCl, and from the nanowire before and after pulling. EELS peak energies (eV): a-9.1, b-15.3, c-20.9, d-32.1; e-2.8, f-5.4, g-11, h-16.4, I-21.8, j-30.6; k-199.7, l-208.5, m-215.7.**

These results consistently show an incomplete, but significant, loss of $Cl^-$ and precipitation of Na in the elongated nanowire. We emphasize that alkali halides are relatively sensitive to electron dosing [240], and even the reduced exposure in the blanked experiment may have significant effects. The threshold displacement energy of NaCl is ~25 eV, corresponding to an electron energy >350 keV, and much larger than the bond energy (~8 eV) [241]. Still, it is well known that electron irradiation creates halogen interstitials and vacancies, which can rapidly migrate to the surface [238]. Coupled with diffusion of atoms from the supporting bulk phase, this may allow the rapid healing of defects, similar to self-healing in superplastic carbon nanotubes [214].

The loss of $Cl^-$ may also decrease grain size, which, together with the high density of vacancy/interstitial defects, may contribute to the nanowire's unusual ductility. For example, Karch et al., reported that brittle ceramics become ductile (~100% elongation) at relatively low

temperatures when the grain size is reduced to a few nanometers, due to diffusion of atoms along grain boundaries [242]. The presence of metallic Na may also enhance ductility. Although the Na-Na bond is significantly weaker (0.76 eV) than a NaCl bond (~8 eV), Na-Na bonds are not stoichiometrically constrained, and their conductivity may help dissipate charge from the electron beam. An excessive material loss rate [240], relative to any healing processes, likely caused the instability at higher TEM magnifications. However, additional studies are needed to quantify the critical size and deformation rates, as well as the irradiation dependence and grain sizes associated with the nanowire superplasticity.

The highly deformable nanowires seen with the TEM demonstrate that smaller, deformable nanowires adhered to the IFM tip could account for the anomalously long interactions seen in the IFM experiment. Although both experiments show bridging behaviors in environments largely devoid of water, several factors besides the irradiation condition preclude a direct comparison. First, surfaces examined with TEM in high vacuum are expected to have extremely low water content compared to those examined with IFM at <0.1% *RH*. Measurements with macroscopic rock salt (~centimeters) have shown that, while dry salt is not absolutely brittle, wet salt is very plastic [216]; consequently, even trace amounts of water may have important effects. Also important is the contact geometry: those used in the TEM produced nanowires with presumably higher aspect ratios and therefore greater extensibility than what might have been formed with larger IFM tips. Differences in applied stresses and contact sizes could also account for these differences [243-245]. Geometry, stress, surface chemistry, water content are also highly variable in the atmosphere and geosphere where NaCl crystals interact with other matter. That nanowires might form in these varied conditions remains an intriguing possibility. Consistently, macroscopic (~mm) whiskers have been grown from NaCl vapors and solutions [246, 247]. Their decorative spiral and zigzag shapes have been attributed to surface impurities, perhaps in much the same way that touching a tip or applying charge creates a defect on the salt surface.

In summary, forces measured between the NaCl(100) surface and a diamond tip show an anomalously long bridging behavior between the two surfaces in humid atmospheres. TEM imaging aimed at discovering the origin of this bridging shows that superplastic nanowires can be extracted from the salt surface by touching it with an adhering tip in the TEM. Several mechanisms may cooperate to produce the superplasticity, namely, small grain size, small linear dimension, diffusion along defects, and Na precipitation. While different environmental conditions preclude a direct comparison between the two experiments, these results raise the possibility that nanowires form between sliding rock salt or between colliding sea salt aerosols. Deformation between surfaces and grains are known to influence the rich network of chemical and physical reactions that drive lithification, the flow of underground sediments, and many atmospheric reactions [216-219, 224]. More fundamentally, the idea that common salt, which crushes brittlely between one's fingers, can be superplastic is a striking and unexpected example of how material properties can change when viewed at the nanoscale.

### *4.1.6 Acknowledgements*

We thank Norman Bartelt and Brian Swartzentruber for useful discussions.

## 4.2 Exploring the Liquid-like Layer on the Ice Surface

The following was published under the same title; see: M. P. Goertz, X.-Y. Zhu and J. E. Houston, *Langmuir*, 2009, *25* (12), pp 6905–6908.

### *4.2.1 Abstract*

Using interfacial force microscopy and a spherical glass probe, we investigate the adhesive and mechanical properties of the so-called liquid-like layer (L-LL) on the surface of ice at various temperatures over the range from −10 to −30 °C. We find that the layer thickness closely follows that predicted on thermodynamic grounds, while the adhesive interaction has the behavior of a "frustrated capillary", strongly suggesting that the layer is viscoelastic. This viscoelasticity is directly probed using a lateral-dither technique to obtain information on the layer's viscous response as a function of both temperature and interfacial separation.

### *4.2.2 Introduction*

The debate on why ice is so slippery has been going on for almost 160 years and is presently thought to be the result of a thin, lubricating water layer on the ice surface even at temperatures well below the melting point [94, 95]. This water film, termed a "liquid-like layer" (L-LL), is the result of premelting and is expected to possess physical properties between those of water and ice. The presence of the L-LL has been verified by a wide range of physical techniques, including optical spectroscopy [248], scattering [249], proton channeling [250], ellipsometry [251], wire regelation [252], calorimetry [253], and scanning probe microscopy [98, 169, 254-256]. Several review articles have summarized previous work in this field [94-96]. The general consensus is that the L-LL exists on the ice surface at temperatures higher than approximately −35 °C and that its thickness increases with temperature. While premelting is common to many solids, only for ice, with a melting point of 0 °C, does it have broad consequences, ranging from geological and atmospheric sciences to daily life.

Despite all the physical measurements, surprisingly little is known about the mechanical properties of the L-LL when one brings a solid surface into contact with ice. For example, does the L-LL wet a hydrophilic surface? If so, does the resulting interaction create a meniscus-like attractive force and what are its viscoelastic properties? To shed light on these questions, we carry out quantitative measurements of the ice surface using interfacial force microscopy (IFM) [225]. We find that the L-LL is responsible for a thickness dependent adhesive-force behavior, whose general appearance is similar to that of a meniscus formation but, in detail, does not fit the behavior predicted, for example, by a simple Laplace-pressure analysis. In addition, friction measurements, obtained synchronously by imposing a small lateral-dither displacement on the probe, shows a rapid rise in the friction force within 20 nm of repulsive contact with the solid−ice surface, indicating a viscous near-surface "interfacial" film within the overall L-LL.

### *4.2.3 Methods*

The interfacial force microscope is a scanning force microscope, similar to the atomic force microscope, but is distinguished by a self-balancing, force-feedback sensor. The unique sensor allows the full range of adhesive and repulsive forces to be measured from 1 nN to 350 μN,

without the typical jump-to-contact instability of spring-based sensors. The probe used here was a pulled glass rod with a 150 μm spherical-tip radius. The probe was cleaned in piranha solution (3:1 conc. $H_2SO_4$/30% $H_2O_2$) to remove any adventitious adsorbed organic contaminants, resulting in a clean-glass surface having a water contact angle of 0°. (***Caution!*** *Piranha solution is a strong oxidant and reacts violently with organic substances.*) Ice samples were grown from drops of Millipore ultrapure water (18 MΩ·cm) on a metal substrate cooled by a Peltier cooler to a temperature as low as −30.0 ± 0.1 °C. The ice samples were annealed through multiple thaw/freeze cycles to attain an optically smooth surface. All measurements were carried out in dry $N_2$ to minimize condensation at low temperatures.

In the IFM measurements, the sample stage was cooled, while the glass tip was not. However, we carried out thermal transport modeling using a finite element code within the COMSOL software package and found that the temperature of the glass tip, while in the vicinity of the ice surface, should be <1 °C higher than that of the ice surface. For each force profile, the probe approached a freshly annealed ice surface at a constant rate while recording the normal force. Friction forces were simultaneously obtained by driving the sensor laterally with a 3 nm peak-to-peak, 50−200 Hz dither and synchronously detecting the force signal with a lock-in amplifier. The dissipative or friction component of the lateral force signal was obtained by recording that portion of the signal in quadrature with the dither drive signal.

### *4.2.4 Results and Discussion*

The presence of a L-LL is evident in the normal force profiles shown in Figure 25a as the spherical glass probe approaches the ice surface from left to right. The most prominent feature is an attractive region (negative forces) shrinking in both width and magnitude as the temperature decreases. At −30 °C, the attractive force is essentially negligible. The rapid rise in normal force at displacements to the right of zero indicates tip contact to the solid−ice substrate. Initial contact with the L-LL is signaled by a very small but sudden increase in the attractive force only visible in the profiles when viewed on an expanded force scale. As the tip continues its approach, the attractive force takes on an appearance similar to that of a growing "meniscus", with the depth and range of the adhesive interaction decreasing with decreasing temperature. We take the displacement from the initial attractive force onset to the bottom of the attractive well to be the thickness of the L-LL, as shown by the vertical dashed lines for $T = -10$ °C in Figure 25. Using values obtained by this approach, we plot in Figure 26 the thickness of the L-LL as a function of temperature. We find that the thickness scales logarithmically with temperature, that is, $D$ (nm) = $A - B \ln(T_m - T)$, in agreement with previous reports [98]. Here, $T_m = 0$ °C, the ice melting point. The fit (solid line) in Figure 26 gives $A = 140 \pm 10$ (nm) and $B = 41 \pm 4$ (nm). These thickness values agree well with those found by proton channeling [250] and are about twice those reported in an atomic force microscopy (AFM) study [98].

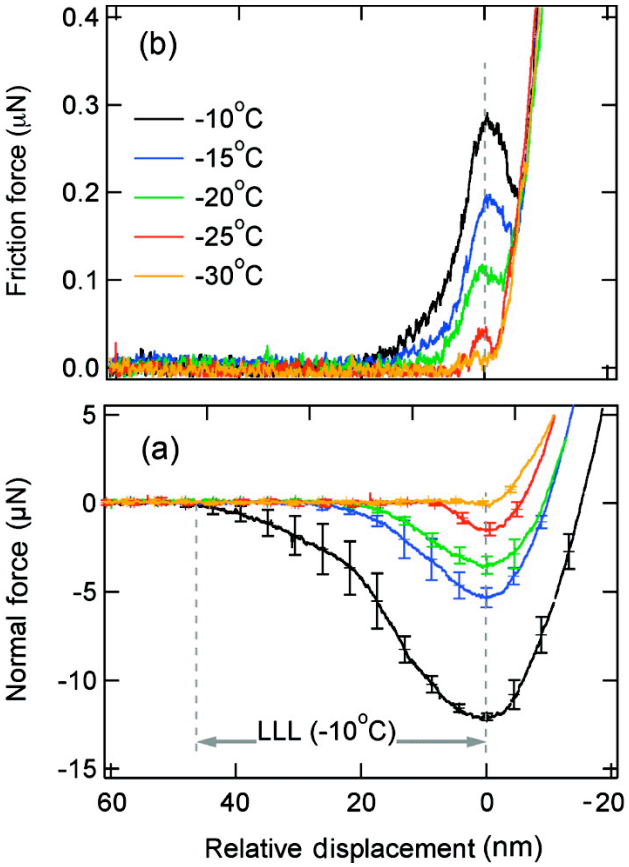


**Figure 25. Temperature dependence of the normal (a) and frictional (b) force profiles on ice. Gray dashed lines are the approximate points of contact with the L-LL and the underlying ice surfaces.**

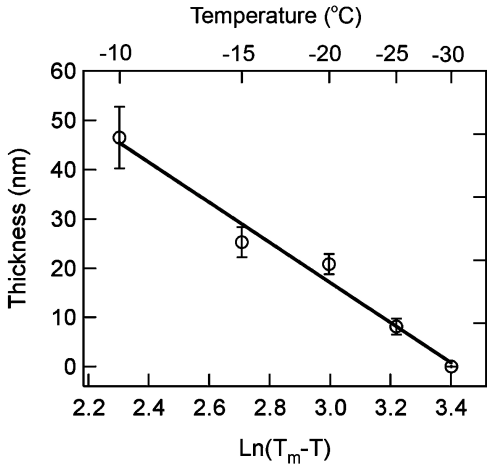


**Figure 26. Temperature dependence of the L-LL thickness on ice. Error bars represent the standard deviation over five measurements.**

To quantify the adhesion interaction, we integrated the approach curves in Figure 25a to obtain the work of adhesion at different temperatures. Scaled in absolute magnitude, these values agree

very well with those obtained from the separation of two ice surfaces by Hosler et al. [257]. Of course, both measurements have in common the interaction with the ice L-LL. The attractive force must result from the wetting of the hydrophilic tip by the L-LL, as was suggested earlier in AFM measurements [98, 169]. As a first approximation, the behavior of the peak attractive force, commonly referred to as the "pull-off force" when measured by an unstable force sensor like that of the atomic force microscope, would be expected to behave as described, for example, by a Laplace-pressure analysis. For the tip making contact with a liquid surface, the force should be described by the relationship [82]

$$F = -4\pi R\gamma_{LV}\cos\theta\,,$$

(1a)

where $\gamma_{LV}$ is the surface energy of the liquid−vapor interface, θ is the contact angle of the liquid with the tip, and $R$ is the tip radius. We do not have an accurate value for the L-LL/glass tip contact angle, but assume that it should to be close to 0°.

Under this assumption, Eq. 1a predicts a meniscus attractive force more than 1 order of magnitude larger than those shown in Figure 25. However, Eq. 1a is not appropriate to the present situation. We are not making contact with a liquid surface, where the meniscus is formed by shear flow along the tip surface from the bulk of the liquid. Rather, in our case, we can only have lateral flow along the ice surface involving a very thin L-LL, and the ratio of the tip radius to the layer thickness is almost a factor of 4000 for the thickest film at −10 °C. Thus, achieving the equilibrium "Laplace" force of Eq.1a would require the flow of L-LL molecules very far from the tip contact. In addition, this flow would involve a "liquid" film only tens of nm thick, both of which seriously limit the growth rate of the contact area, a situation aptly described as the formation of a "frustrated" capillary.

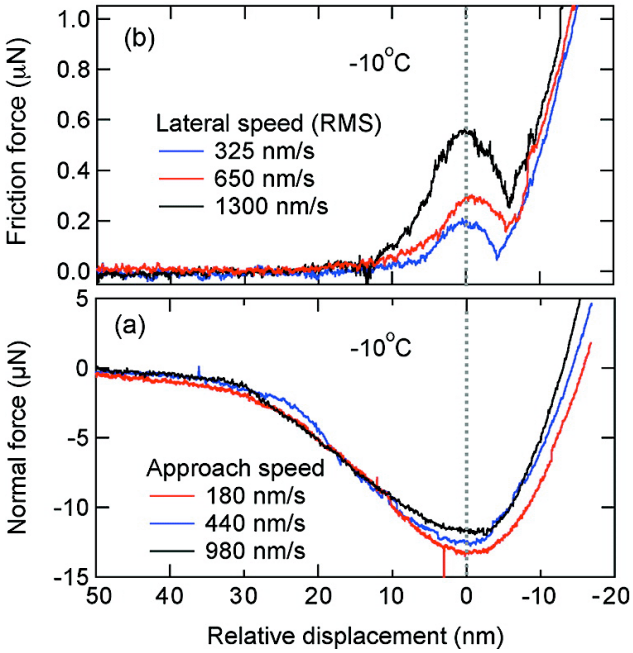


**Figure 27. (a) Approach speed dependence on the adhesion of the L-LL at −10 °C. (b) Lateral tip speed dependence of friction forces on ice at −10 °C. Gray dashed line is the approximate point of contact.**

The formation of such a frustrated capillary is also revealed in the dependence of force profiles on tip speed. Figure 27a shows the normal force behavior as the tip approaches the surface at speeds varied by a factor of 5. As expected, the slower speed shows the largest adhesion force, since it allows the accumulation of more L-LL in the frustrated capillary. The changes are rather small, but the time that the tip is in contact with the L-LL, even in the slowest case at −10 °C, is only about 200 ms. Unfortunately, we were not able to do a true "creep" measurement to obtain accurate relaxation times for the L-LL because of the rapid recession of the ice surface due to sublimation. Under our experimental conditions, the ice surface recedes at a rate of approximately 10 nm/s, which also creates a certain amount of surface instability. This instability at the junction gives rise to a significant noise level in the normal force signal. Attempts to stabilize the rate of surface recession by raising the relative humidity resulted in the rapid micrometer-level growth of a complex array of interconnected crystallite structures, further interfering with the sensitive measurements of the interfacial mechanical properties. In addition, efforts to stabilize the ice recession by covering the surface with various organic liquids also proved unsuccessful.

We now turn to the behavior of the lateral friction force for the interfacial layer as a function of temperature, as summarized in Figure 25b. First, note that the friction force begins its rise at a point well within the overall L-LL, reaches a peak very near the adhesion-force maximum, and then rapidly decreases as the normal force begins its repulsive rise. This behavior is reminiscent of that found in several earlier studies involving the interfacial water layer confined at the nanometer level between various hydrophilic surfaces [8, 10]. The decrease in friction force is accompanied by a rapid fall in the phase of the synchronous signal, implying that the tip compliance is coming into play. As the repulsive normal force rises, the tip begins a "stick−slip" type behavior as it burrows into the ice surface, giving rise to a falling phase toward 0°.

As in the earlier studies, viscosity values for the "interfacial" water can be approximated through the use of an equation tailored for such conditions by Feibelman [131]:

$$F_\eta = 2\pi\eta\omega x_0 R \ln(\frac{D}{2w}), \quad (2a)$$

where η is the viscosity, ω is the angular dither frequency, $x_0$ is the dither amplitude, $R$ is the tip radius, $2w$ is the total interphase-layer thickness, and $D$ is the level of tip penetration into the interfacial layer. It is assumed in deriving Eq.2a that the viscosity does not vary with distance from the solid−ice surface and assumes the no-slip boundary condition at both interacting surfaces. Again, notice, in comparing panels a and b in Figure 25, that the rise in friction involves an interfacial layer that is thinner than the L-LL itself and both thicknesses decrease as the temperature is reduced until at −30° it is difficult to delineate the two. Fitting the Feibelman equation to the −10 °C friction results in a viscosity value of 220 Pa·s, almost $2.5\times10^5$ times larger than that of bulk water or a little over $6\times10^4$ times that of supercooled water [258]. These figures are, of course, rough estimates because of the inherent noise level created by the unstable ice surface and become even worse at the lower temperatures. However, it would appear from the general rate of friction-force increase in this area that the value of viscosity is remaining essentially constant with temperature. Previous attempts at measuring the viscosity of the L-LL include using shear rheology techniques, which yielded viscosity values of 1.5−70 mPa·s [259], as well as approach speed dependent AFM measurements, which found the viscosity of the L-LL to be at least a factor of 300 greater than that of water (0.89 Pa·s). These measurements are not without detractors, as many previous authors have assumed that the upper limit of the viscosity of L-LL is that of supercooled water, which is, at most, 4 times the viscosity of bulk water [256]. The viscous nature of the L-LL is more clearly revealed in the lateral force measurements taken at several lateral-tip speeds, Figure 27b. The lateral force increases with tip speed, although not exactly according to the linear relationship expected from a pure viscous response. However, the accurate characterization of this "frustrated-capillary" behavior involves a rather sophisticated hydrodynamic model and is certainly beyond the scope of this contribution.

The lateral force, after contact with the solid−ice substrate, rises in direct proportion to the normal force and, in fact, appears in direct proportion, confirming that the behavior is attributable to the properties of the solid−ice surface itself. At the maximum applied force of 5 μN in the −10 °C data, the stress applied to the "solid" ice surface is approximately 800 GPa. At this stress, the tip penetrates the solid surface by about 10 nm, while the lateral force has a peak value of 0.4 μN. The situation is a nanoscopic version of the artic explorer's use of crampons for climbing on ice, where multiple asperities penetrate the L-LL and deform the substrate ice, resulting in greatly increased traction. In the present case, we have a crampon with only one asperity and the lateral force increases in direct proportion to the normal force. This behavior is often seen in multiple asperity situations and results in the commonly encountered "Amonton" behavior, that is, with the friction force directly proportional to the normal force and the proportionality constant defined as the coefficient of friction.

### *4.2.5 Conclusions*

We have directly shown that a L-LL exists on the surface of ice, with a thickness that varies with temperature as described by a thermodynamic model [260]. This layer gives rise to an attractive force characteristic of a "frustrated capillary", since the water source to build the capillary involves the axial flow along the ice surface of a very thin, viscous layer. We also find that this layer has a viscosity significantly larger than that of bulk water varying only slightly with temperature. In conclusion, it is compelling to speculate on what the present results contribute to the age-old question as to just why ice is so slippery [261].

Faraday was the first to suggest the existence of a L-LL on the surface of ice but was voted down in favor of pressure melting, which held sway for almost a century. At present, it is widely accepted that friction heating is the origin of the effect [262]. However, the existence of the L-LL has been well established in many careful experiments and is clearly present at the surface in the absence of friction. In addition, the common experience of walking on glare or smooth ice clearly shows that presliding is not necessary in order to discover that the erect position can be unstable.

Friction at general interfaces normally involves multiasperity contacts which extends to the atomic level, as illustrated by the slip friction seen in the shear motion between atomic planes in, for example, graphite or mica [99]. The effect results from the lateral force required to overcome both the adhesion interaction and the mechanical interlocking of the asperity−asperity contacts [99]. This is dramatically demonstrated by the fact that the static coefficient of friction is always greater than that of the "dynamic coefficient"; once the lateral motion sets in, the interaction is more limited and involves contacts between the asperity *peaks* reducing both the adhesion and interlocking effects. It is also the root cause of the commonly observed "Amonton" behavior, where the friction force is directly proportional to the normal force [263].

Lubricants for most surfaces are generally viscous, thin-film liquids, able to separate the asperity surfaces with a viscous force that depends on sliding velocity. With respect to this general model, ice with its naturally occurring, viscous L-LL is perhaps the premier example of a "self-lubricating" material, when supporting contact with ordinary surfaces, for example, ice skates. Contact with these surfaces further encourages the maintenance of the L-LL due to the effect of ice creep, where a weight placed on the ice slowly penetrates the surface [264]. In addition, the L-LL has a smoothing effect on the ice surface [257] and sublimation (strictly speaking, evaporation from the L-LL) adds an additional water-vapor boundary layer, concentrated near the surface by the surrounding atmosphere, that could further aid in separating the sliding surface from that of the bulk-ice substrate.

Finally, our results indicated only a very thin L-LL at −30 °C and leaves open the question as to what the ice surface is like at very low temperatures. A strong hint can be found in the writings of Edward Wilson, Robert Falcon Scott's chief scientist during his final visit to the Antarctica. Scott had earlier described skiing easily at −30 °C, while Wilson described the snow surface as "sand like" at −46 °C, presumably resulting from the complete absence of the L-LL [261].

### *4.2.6 Acknowledgments*

We thank Nathan Moore for help with analysis of the friction data and the DOE Office of Basic Energy Sciences for partial support.

## 4.3 The Pull-Off Force and the Work of Adhesion: New Challenges at the Nanoscale

The following was submitted for publication for the Special Issue, "Adhesion in MEMS and NEMS" of the Journal of Adhesion Science and Technology, c.a. 2010, authored by N.W. Moore and J.E. Houston.

### *4.3.1 Abstract*

The pull-off force required to separate two surfaces has become a convenient metric for characterizing adhesion at the micro- and nano- scales using cantilever-based force sensors, such as an atomic force microscope (AFM), e.g., as a way to predict adhesion between materials used in MEMS/NEMS. Interfacial Force Microscopy (IFM) provides unique insight into this method, because its self-balancing force-feedback sensor avoids the snap-out instability of compliant sensors, and can estimate both the work of adhesion and the pull-off force that would be measured using a compliant cantilever. Here, IFM is used to illustrate the challenges of determining the work of adhesion from the pull-off force in a nanoscale geometry. Specifically, adhesion is evaluated between a conical, diamond indenter and three surfaces relevant to MEMS/NEMS adhesion problems: silicon, a model insulator, and a compliant polymer surface.

### *4.3.2 Introduction*

Adhesion at the nanoscale and between MEMS/NEMS components can be unique both physically and in the manner in which it is measured [265]. Unpredictable topographies, size-dependent deformation mechanisms, compliance of surface coatings, and the statistical nature of device/surface fabrication are just a few complexities that lead to a rich diversity of adhesion behavior at the nanoscale [109, 265-271]. An equal challenge is that nanoscale adhesion is often most conveniently measured with scanning probe microscopies, which can measure very small forces but provide only limited information about the contact geometry [272, 273], thus making difficult the validation of suitable contact mechanics models.

Given the above, it is not surprising that classical theories, such as the JKR [228] or DMT [274] theories for single-asperity contacts, sometimes fail to describe adhesion at the nanoscale [267, 269]. Nonetheless, this framework is frequently used to relate the pull-off force required to separate surfaces to the work of adhesion of the contacting materials, using either the original JKR or DMT models or their many variants [275]. This method seems practical, first because the work of adhesion can be reasonably estimated with minimal calculation for many types of adhesion interactions, particularly at the macroscale [82, 269, 275-280]. Second, in measurements with a cantilever-based force sensor (e.g., atomic force microscopy or MEMS cantilever), the pull-off force is often the only adhesion metric available [265, 272]. It is well recognized that cantilever force sensors are inherently unstable, as the cantilever will snap into or

out of contact with a surface whenever the gradient of the force between the tip and the sample exceeds the cantilever spring constant [82, 265]. Replacing a weak cantilever with a stiffer one can avoid this problem, but the reduction in force sensitivity may be unacceptable.

Growing recognition of these challenges makes timely a perspective based on measurements with Interfacial Force Microscopy (IFM) [42, 225, 281]—a scanning probe technique that is perhaps best known for its ability to avoid jump-in and jump-out instabilities, and thus provide a more complete view of the surface forces that drive nanoscale adhesion. The IFM's unique sensor design maintains stability in a force gradient by tracking the tip's displacement in response to a force, as a differential change in the capacitance of two capacitors mounted on each side of a teeter-totter to which the tip is attached (Figure 28). The DC voltage on the capacitor pads is continually adjusted using a feedback controller to eliminate the tip displacement, with the applied voltage allowing a simultaneous measure of the force encountered by the tip. With this scheme, the IFM sensor is noncompliant, yet can measure attractive and repulsive forces at all tip-sample separations.

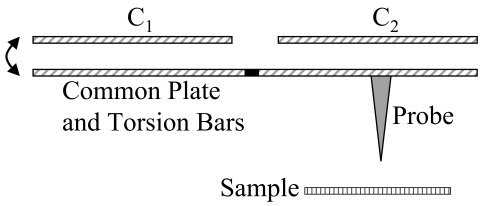


**Figure 28. Schematic of the IFM's differential-capacitor force-feedback sensor, showing the capacitor gaps on each end of the common plate, with capacitances $C_1$ and $C_2$.**

In this work, we utilize the IFM's ability to measure the work required to separate two surfaces, as the integral of the force-displacement curve. Then, we approximate the corresponding pull-off force that would be measured by a weak (infinitely compliant) cantilever based on the maximum adhesion force value. Estimating the work of adhesion from each method provides a framework for comparing the strengths and weaknesses of each approach to characterizing nanoscale adhesion. Specifically, we compare the work of adhesion estimated from each method for three model surfaces with properties relevant to MEMS/NEMS adhesion problems: a silicon surface, an insulator ($BaF_2$), and a polymer surface [poly(vinyl acetate)].

This work follows an earlier IFM study of adhesion between surfaces decorated with self-assembled alkanethiol monolayers terminated in either $CH_3$ or $CF_3$ end groups [282]. There it was shown that the pull-off force was the same within ~10%, but that the work of adhesion differed by nearly a factor of 2. This discrepancy was attributed to the complex mechanics of the adsorbed films under the influence of the long-range Debye component of the van der Waals attraction. We expand on this observation by showing that a convolution of van der Waals and electrostatic forces, capillary attraction, elastic deformations, and/or viscoelastic deformation can lead to a rich variety of adhesion behavior at the nanoscale that can be masked when only the pull-off force is measured. These interactions are particularly relevant to MEMS/NEMS, as there has been considerable effort to develop thin-film coatings to eliminate capillary adhesion between components, and to reduce corrosion and wear [283].

### *4.3.3 Methods*

The idea of relating adhesion properties to a pull-off force originates from the theory developed by Johnson, Kendall, and Roberts (JKR) [228], which has the key assumptions: 1) the two interacting solids are isotropic, linear elastic materials; 2) attractive forces act over an infinitesimal distance; and 3) the contact is frictionless. Because only a few materials meet these requirements, many refinements have been made, such as the DMT model [274], which addresses assumption (2), and various "transition" models that are valid over larger parameter spaces (for reviews, see [82, 265, 275, 284]). Of the extensive work in this area, the JKR and DMT models are perhaps the most widely used [285], owing to the simple result that the pull-off force ($F_{PO}$) is linearly related to the work of adhesion ($W$) by:

$$F_{PO} = -\xi \pi R W \tag{1b}$$

where $R$ is the asperity radius and $\xi = 3/2$ and 2 in the JKR and DMT theories, respectively [228, 274]. Which model is more appropriate depends on the magnitude of the adhesion relative to the contact's composite modulus ($K$). This is usually decided by evaluating the Tabor parameter, $\mu_T = (16RW^2/9K^2z_0^3)^{1/3}$ [286], where $z_0$ is the range of the interatomic potential, for which 3Å may be a good estimate [82]. The choice of models is JKR for $\mu_T > 5$, DMT for $\mu_T < 0.1$, and a transition model for intermediate values [82].

More recently, Yang developed a model appropriate for adhesion between a conical indenter on a flat sample of the same material, which, apart from geometry, follows the same assumptions as the JKR model [287]. For frictionless contact, the Yang model gives the work of adhesion as

$$W_{PO} = [F_{PO}\, \pi\, K \,\mathrm{Cos}^2(\theta)\, \mathrm{Tan}^3(\theta) / 54(1-\nu^2))]^{1/2}, \tag{2b}$$

where $\nu$ and $\theta$ and are the Poisson's ratio and indenter half-angle, respectively. The elegance of Eqs.1 and 2 is that these predict a simple relationship between the work of adhesion and the pull-off force ($W_{PO} \propto F_{PO}$ or $W_{PO} \propto F_{PO}^{1/2}$). More difficult is the frequent need to relate the work of adhesion, which is defined on an areal basis, to the work that would be required to separate two real asperities. In general, this requires accurate values for the energies required to create two solid surfaces, their interaction with the intervening medium, and their interaction with each other [82]. For the materials we consider, this is further complicated by the fact that the intervening medium may not have uniform properties throughout the contact, as is true for nanoscale liquid capillaries, which may not occupy the entire region over which attractive forces are important [288, 289]. Further, one may need to consider surface roughness, chemical inhomogeneities at or near the opposing surfaces, viscoelastic deformation, and surface contamination—complications that can play exaggerated roles at the nanoscale [265]. As we show here, the numerical result can also be quite sensitive to the probe shape.

Rather than address all possible scenarios, we restrict our analysis to the minimum required to show key trends. Specifically, in the pull-off method, we use Eq.2b to estimate the work of adhesion that would be required to separate two parallel surfaces. Also, because the IFM does not experience a pull-off point, we take $F_{PO}$ to be the minimum of the force-well in the force-displacement curve measured with IFM. This corresponds to the pull-off force that would be

measured had the measurement been done with an infinitely complaint cantilever. Although no cantilever is infinitely compliant, this method approximates the pull-off force that would be measured in experiments wherein soft cantilevers are chosen to enhance force sensitivity [272].

To illustrate the difficulties of relating a pull-off force to the work required to separate two real asperities, we also estimate the work of adhesion using a second method. The "integral method" capitalizes on the IFM's unique ability to measure forces at all tip-sample distances. The integral of the attractive portion of the force-displacement curve divided by the contact area gives the work of adhesion, $W_I$, required to separate the real contact. While this method appears simple, the challenge is in estimating the true area of a material contact that is only a few nanometers wide. Few techniques can measure a tip's shape to such accuracy, so that the shape of the indentation can only be estimated using contact mechanics models. Another challenge is that sharp conical or spherical tips may adhere laterally to the contact's periphery, creating additional contact area, so that the work of adhesion is overestimated. Again, these shortcomings introduce systematic uncertainty, but do not affect our conclusions, which are concerned only with trends.

To compare $W_I$ to the $W_{PO}$ measured from the pull-off method, we used the same Yang model [287] to calculate the contact area ($A$) at the equivalent pull-off, or separation, point between the conical indenter and flat substrates, viz.,

$$A = \pi[18(1-\nu^2)W_{PO}/(\pi\, \mathrm{K}\, \mathrm{Cos}(\theta)\, \mathrm{Tan}^2(\theta))]^2. \qquad (3b)$$

This area estimate requires an estimate of the work of adhesion, for which the value from the pull-off method (Eq.2b) was used to allow a comparison between the pull-off and integral methods. Both the pull-off and integral methods estimate the work of adhesion on an areal basis; however, their definitions are geometry-specific. As stated, $W_{PO}$ represents the work to separate two flat surfaces, while $W_I$ represents the true work to separate the conical and planar surfaces, divided by the estimated area of that particular contact. Because these geometries are not equivalent, one should not expect the two methods to yield identical values. For example, this can occur when the true contact area is enlarged by lateral adhesion between the tip and substrate, or by the presence of a liquid capillary [288]. Nonetheless, because these differences are systematic, one should expect $W_{PO}$ and $W_I$ to be strongly correlated if the pull-off force is, in fact, a good indicator of the work required to separate two surfaces.

It is important to recognize that the values for $W_I$ and $W_{PO}$ are highly sensitive to the half-angle of the indenter used. To show this quantitatively, we note that the numerical calculation of $W_I$, $W_{PO}$, and their ratio, have the following proportionalities:

$$W_I \propto \mathrm{Sin}^2(\theta)\, \mathrm{Tan}^2(\theta) \qquad (4b)$$

$$W_{PO} \propto \mathrm{Cos}(\theta)\, \mathrm{Tan}^{3/2}(\theta) \qquad (5b)$$

$$W_I / W_{PO} \propto \mathrm{Sin}(\theta)\, \mathrm{Tan}^{3/2}(\theta) \qquad (6b)$$

from Eqs. 1–3. A physical difference in angle will also correspond to different contact areas and forces, so that the proportionalities of Eqs.4–6 are only meaningful as an assessment of systematic error introduced by uncertainty in $\theta$. Using Eqs.4–6 with a nominal value of $\theta = 60^\circ$, a

5% uncertainty in $\theta$ produces uncertainty in $W_I$, $W_{PO}$, and the ratio, $W_I$ / $W_{PO}$, of 18%, 62%, and 43%, respectively. In comparison, uncertainty in the work of adhesion determined with a spherical tip scales linearly with uncertainty in the tip radius (Eq.1b). An additional systematic error in the calculation of $W_I$ and $W_{PO}$ may arise from the faceted shape of the diamond indenter, for which the cone geometry of the Yang model is only an approximation. A smaller systematic error (<5%) arises from assuming a Poisson's ratio of 0.3 for both tip and substrate, which are assumed identical in Eqs.2–3. For these reasons, we do not attempt to compare the absolute values of $W_I$ and $W_{PO}$ on a point-by-point basis. Instead, we focus only on the relative trends between $W_I$ and $W_{PO}$. This approach is reasonable because the shape of the diamond indenter can be expected to remain constant under the short times and small elastic loads applied in these experiments.

A Sandia-built Interfacial Force Microscope and control software were used as described elsewhere [42, 225]. The present configuration can measure forces between ~30 nN and 50 μN with time resolution ~1 ms, over a wide range of temperature (–50 to +100ºC) and relative humidity (0<*RH*<70%). Accuracy in the measured force was limited by absolute error in calibrating the sensor gain (±10%). Accuracy in the tip displacement is limited by absolute error in calibrating the piezo actuator (±5%).

Polished single-crystal $BaF_2$ (Alfa Aesar, Ward Hill, MA; Lot#G16S051) was cleaned with ethanol and dried in the measurement chamber (<1% relative humidity, *RH*) at 75ºC for 2.5h before use. AFM imaging showed that the $BaF_2$ surface used here was atomically flat over the areas of interest. Si(111) substrates were rinsed in ethanol and water and dried. Poly(vinyl acetate) (Scientific Polymer Products; provided by courtesy of Hongbing Lu, University of North Texas) was in the form of ~4 mm hemispherical pucks, cleaned with ethanol, and dried. The IFM tip was a conical diamond indenter (macroscopic half-angle θ = 30º) and cleaned by rinsing successively in 3:1 concentrated $H_2SO_4$/30% $H_2O_2$ (piranha), water, and ethanol, and dried, which left the tip mildly hydrophilic (water contact angle ~70°). Caution! Piranha is a strong oxidant and reacts violently with organic substances. The end radius of the diamond tip was estimated by scanning the tip over a calibration grating (MikroMasch, Si grating #TGG01), viz., ≤10 nm, which is an upper bound for the grating radius. This value was used to estimate the Tabor parameter. All measurements were performed at room temperature and <1% *RH* except where noted. $BaF_2$ and Si surfaces were grounded to minimize electrostatic charging.

### *4.3.4 Results and Discussion*

To compare what can be learned from the pull-off and integral methods, we briefly examine the adhesion between our diamond tip and three materials showing distinct adhesion mechanisms. The first, adhesion between diamond and Si(111), is shown in Figure 29A. The force between tip and substrate gradually becomes more adhesive (negative) as the tip approaches the surface, until the two materials touch near $D \approx 0$, defined as the distance where the force is minimum (most negative), i.e., where the force of elastic compression begins to become significant. That only a slight hysteresis is seen between the force on approach and withdrawal is consistent with the presence of only van der Waals or electrostatic forces.

To show that the long-range attraction is not dominated by van der Waals forces, we use the model of Argento and French [290] to estimate the magnitude of the van der Waals interaction between the conical tip and substrate, viz.,

$$F_{vdW} = [\alpha \rho^2 (1-\mathrm{Sin}(\theta)) (\rho \,\mathrm{Sin}(\theta) - D \,\mathrm{Sin}(\theta) - \rho - D)] / [6 D^2 (\rho + D - \rho \,\mathrm{Sin}(\theta)^2]$$

$$- \alpha \,\mathrm{Tan}(\theta) [D \,\mathrm{Sin}(\theta) + \rho \,\mathrm{Sin}(\theta) + \rho \,\mathrm{Cos}(2\theta)] / [6\mathrm{Cos}(\theta) (D + \rho - \mathrm{Sin}(\theta))^2] \qquad (7b)$$

where $\rho$ is the end-radius of a spheroconical tip and $\alpha$ is the Hamaker constant. In principle, values for $\alpha$ could be estimated using dielectric constants for the interacting materials. However, for an order of magnitude estimate, it is sufficient to assume a typical value, $\alpha$ of the order $\sim 10^{-19}$ J as values for $\alpha$ span a narrow range for a broad range of materials ($\sim 1\text{–}50 \times 10^{-20}$ J) [82]. We use the macroscopic half-angle of the diamond indenter ($\theta = 30°$), and values for the unknown $\rho$ ranging from 0 to 1 μm. For these parameters, the magnitude of the attractive van der Waals force (Eq.7b) ranges from $10^{-6} - 10^{-3}$ μN for $D$ = 40Å, $10^{-5} - 0.2$ μN for $D$ = 3Å, and $10^{-4} - 1.5$ μN for $D$ = 1Å. Similarly, values of $F_{vdW} < 10^{-3}$ μN are estimated for $\rho = 0$ and $1° < \theta < 80°$. Consequently, for the probe geometry here, the van der Waals force is significant over only a few atomic distances. Sumant, et al. [291], measured the work of adhesion for a diamond-coated tip and a Si(111) substrate, and found $W_{PO}$ = 59 mJ/m$^2$, which was attributed solely to van der Waals forces. Their value is an order of magnitude lower than what we find in this particular experiment (Figure 29B), suggesting again that here the adhesion is dominated by long-range electrostatic forces, e.g., as can arise from surface charge [291].

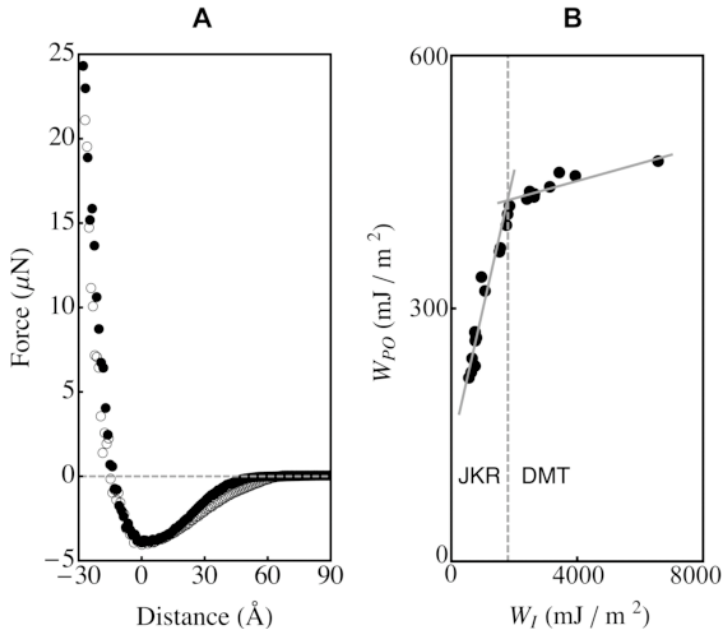


**Figure 29. Interaction between a diamond tip and Si(111) at 25ºC and <1% *RH*. (A) Example measurement of the normal force during the tip's approach (●) and withdrawal (○). (B) Comparison of the work of adhesion calculated by the pull-off force method ($W_{PO}$) and the integral method ($W_I$). Dashed vertical line indicates the approximate transition from the JKR to DMT regimes. Grey lines are best-fit lines in each regime.**

Each data point in Figure 29B represents a measure of the work of adhesion every ~4 minutes in the same location on the sample, as calculated from both the pull-off ($W_{PO}$) and integral ($W_I$) methods. As the surface ages over a span of ~100 minutes, both $W_{PO}$ and $W_I$ decrease commensurately. This decrease in adhesion can be ascribed to chemical changes at the interface, e.g., from triboelectrification or oxidation, rather than from physical changes in the underlying material, which never showed plastic deformation under these small indentation forces (<25 μN).

This example is classic in that at least two of the key requirements of the JKR-DMT framework are fully met: both tip and substrate are elastic, and the adhesion forces (i.e., the van der Waals and electrostatic forces) are conservative forces. That is, the amount of energy dissipated during the formation and rupture of the single asperity contact was insignificant, as evidenced by the small hysteresis between the approach and withdrawal data in Figure 29A. For this reason, we find excellent correlation between the works of adhesion calculated using the pull-off force and integral methods. The two methods give values that are correlated in each of the two regions indicated in Figure 29B (dashed line). This division roughly corresponds to the transition between the JKR and DMT regimes ($\mu_T$ ~1.2, $W_I$ ~1900 mJ/m$^2$). This deviation is expected because Yang's model for conical adhesion is strictly valid only for the JKR regime, so that $W_{PO}$ is underestimated for higher values of $F_{PO}$. That $W_I$ is much larger than $W_{PO}$ may stem from systematic error in estimating the true contact area for the cone-plane geometry (Eq.3b), as discussed earlier. For this work, the key detail is the strong correlation between $W_I$ and $W_{PO}$. This correlation suggests that either method could be used as a general indicator of the adhesion strength between these materials.

The situation changes dramatically when the tip is brought near our model insulator surface. $BaF_2(111)$ is a well-defined, ionic surface that exposes a hexagonal array of barium and fluoride ions and is moderately hydrophilic [227]. Figure 30A shows a long-range attraction that abruptly changes to a stronger, short-range attraction when the tip is ~50Å from the $BaF_2$ surface. Here the force-distance profile becomes more linear, a strong contrast from the monotonically decreasing attractive force at larger distances. Such short-range, quasi-linear forces can arise from condensation of vapor into a liquid capillary between the tip and substrate [108]. This transition in force might also arise from solid necking in response to short-range, van der Waals forces [8, 108, 285]. That is, at tip-sample separations on the order of a few angstroms, where the van der Waals forces dominate the adhesion forces, the gradient of the attractive force can exceed the effective elastic constants of the tip and substrate materials, causing them to snap into contact [42]. The above analysis using Eq.7b can also be used to argue that, here also, the long-range force cannot be explained by van der Waals forces alone, and is therefore likely electrostatic in origin, as would be expected if defects were present in the ionic surface.

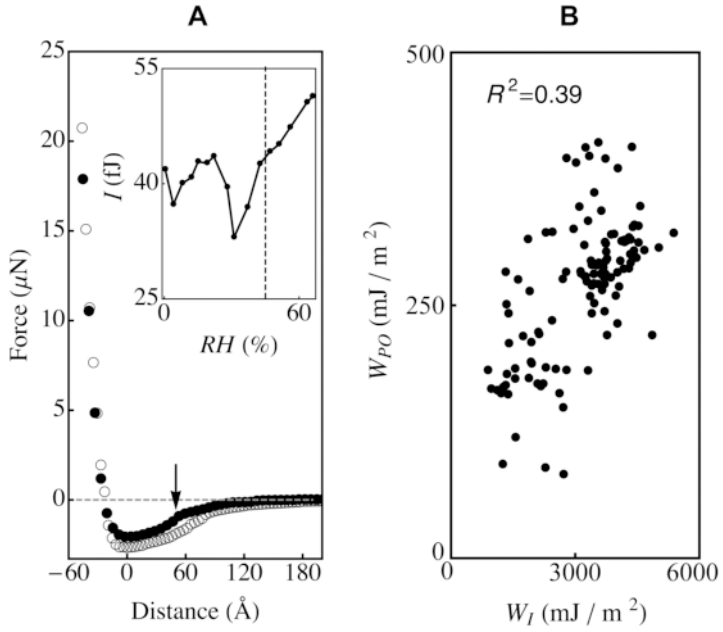


**Figure 30. Interaction between a diamond tip and a model insulator surface, $BaF_2(111)$. (A) Example measurement of the normal force during the tip's approach (●) and withdrawal (○) (25ºC, 1% *RH*). Arrow marks the onset of the short-range attraction. Inset shows how the integral of the force curve, *I*, changes with relative humidity at 25ºC; dashed vertical line indicates the humidity corresponding to monolayer adsorption on isolated $BaF_2(111)$ surfaces [227]. (B) Comparison of the work of adhesion calculated by the pull-off force method ($W_{PO}$) and the integral method ($W_I$), from measurements over a range of temperature (23–90°C) and relative humidity (1–66%).**

The humidity dependence (Figure 30A, inset) suggests that both capillary attraction and elastic necking may contribute to the short-range adhesion. Below ~45% *RH*, the integral of the force curve, *I*, fluctuates seemingly randomly, while above ~45% *RH*, *I* increases steadily with humidity. This transition occurs near the 45% *RH* required to produce a net monolayer coverage of water on an isolated $BaF_2(111)$ surface [227]. We anticipate that capillary formation is

"frustrated" at low humidities, before the surface is wetted fully [28, 110]. We also note that such a liquid capillary would have a very small volume ($<10^5$ Å$^3$ as estimated using the method of Sirghi et al. [108]), which would preclude more than ~1 $BaF_2$ unit being dissolved before the meniscus is saturated with $Ba^+$ and $F^-$ ions. Such small amounts of dissolution have been shown to allow hillocks of salt to grow inside a nanoscale meniscus formed between a NaCl crystal surface and an AFM tip [220]; however, this process occurs over a timescale of minutes to hours. Thus, for the measurements here, which lasted only a few seconds, we do not anticipate that dissolution played a dominant role in the surface mechanics or the measured adhesion forces.

Here, the possible confluences of long-range electrostatic and short-range van der Waals forces, capillary attraction, and short-range DMT-type necking control the adhesion in a complicated manner, even at low humidities. For this reason, Figure 30B shows no apparent correlation between $W_I$ and $W_{PO}$ ($R^2$ = 0.39). This contrasts with the diamond/Si interaction (Figure 29), which showed strong correlation between $W_I$ and $W_{PO}$, even in the DMT regime. Both Si and $BaF_2$ behave elastically with a relatively high Young's modulus (~150 and 54 GPa, respectively), and produce similar pull-off forces. Yet with $BaF_2$, the relationship between $W_I$ and $W_{PO}$ is unclear. This result also contrasts with the supposition by several authors (e.g., [276, 286]) that the JKR-DMT type framework is relatively insensitive to the nature of the adhesion forces. The large scatter in the data (Figure 30B) echoes a common challenge in characterizing adhesion at nanoscale dimensions, namely, that the geometries of the contacting surfaces and any capillary between them are generally unknown, and may be highly variable. In particular, that capillary forces can modify the contact geometry has only recently begun to be explored for a sphere-plane contact geometry [229]. How these effects could be manifested in a cone-plane geometry remains an open question.

We now turn to a third example of an adhesion interaction where the pull-off and integral methods can show qualitatively different trends in the adhesion behavior, namely, in adhesion to compliant polymer films. Because MEMS/NEMS are frequently coated with thin films to reduce friction and corrosion, even structural components that behave as elastic bodies at the macroscale can have surfaces that deform plastically or viscoelastically at the nanoscale [282]. For this we have repeated similar IFM measurements, using the same tip as before, on the surface of poly(vinyl acetate), PVAc.

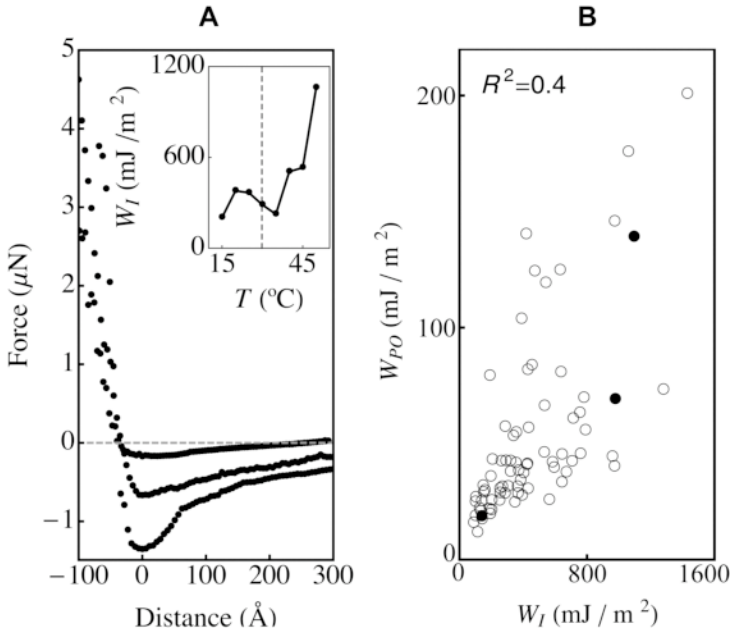


**Figure 31. Interaction between a diamond tip and the surface of poly(vinyl acetate). (A) Example measurements of the normal force in different sample locations (bottom to top: after 3, 6, and 9 successive compressions, respectively). Inset shows the work of adhesion as a function of temperature (*T*); each point is an average of ~10 measurements at various speeds and indentation depths; dashed vertical line is the polymer glass-transition temperature. (B) Comparison of the work of adhesion calculated by the pull-off force method ($W_{PO}$) and the integral method ($W_I$) for the three curves in Part (A) (●) and for all measurements over the range, 15–50ºC (○).**

Figure 31A shows three examples of force-displacement profiles measured between our diamond tip and the PVAc surface, in different locations on the sample, after 3, 6, and 9 loading cycles (bottom to top curves, respectively). In each of the force curves in Figure 31A, the attractive forces extend up to ~600Å from the surface (not shown), suggesting that the long-range attraction is electrostatic in origin, as might arise from charged impurities introduced during manufacture of the polymer, for example. This view is supported by the analysis using Eq.7b, which showed that for the present tip geometry, the van der Waals force is only expected to be significant over a few atomic lengths. In all cases, the forces in Figure 31 at long range ($D$>100Å) are proportional to $1/D^n$, with $n$ = 1.8±0.3. This exponent falls within the range (1–3) determined for a van der Waals force between sphero-conical probes and a flat surface [290]. However, as Argento and French [290] point out, it is not possible to distinguish this scaling from an electrostatic interaction when there is the possibility of plastic deformation, as might be caused by repeated indentations. Here, the magnitude of the long-range adhesion decreases with the cycle number (Figure 31A), implying smaller contact areas and a surface that is less able to conform to the indenting tip.

The near-surface force behavior is more distinct. The bottom curve in Figure 31A shows a slope discontinuity near $D$ = 60Å. This may arise from viscoelastic (time-dependent) deformation of the polymer surface onto the tip. Under the influence of attractive force, a viscoelastic material can be expected to adhere to the tip in a manner that depends on the entire history of the tip-sample contact. Here, repeated compression resulted in a more elastic response (cf. Figure 29),

e.g., as could arise from either a reshaping of the polymer surface or from a local change in mechanical properties as the molecular chains within the polymer are reorganized under the applied forces. The temperature dependence also suggests that the adhesion is influenced by viscoelastic deformation of the polymer onto the tip. Temperature was varied over 15–50ºC in a random sequence for the same sample, which may introduce complicated history effects, such as water adsorption/desorption, that we do not attempt to quantify here. Although we do not see evidence of capillary condensation in the force profile (Figure 31A), PVAc is extremely hygroscopic, and even small amounts of absorbed water affect its viscoelastic properties [292]. Nonetheless, it can be seen that above 35ºC (near the glass transition temperature, $T_g$ ≈30ºC [292]), the work of adhesion increases with temperature to about twice the values near room temperature (Figure 31A, inset). This transition is expected, because increased mobility of the polymer chains above $T_g$ allows the polymer to flow onto the tip more rapidly, creating larger contact areas.

These subtle changes at the polymer surface are not predicted by the pull-off force, which, in Figure 31A, simply decreases with cycle number. Further, the pull-off force is not strongly correlated with the work of adhesion for this material. Looking at the entire data set, the works of adhesion calculated with each method ($W_{PO}$ and $W_I$) are not strongly correlated ($R^2$ = 0.40). Considering just the three examples in Figure 31A (dark circles in Figure 31B), the two measurements with the strongest adhesion have $W_I$ within 12% of each other, while the work of adhesion calculated from the pull-off force ($W_{PO}$) differs by ~100%. That is, in these measurements, the pull-off force does not predict the material's adhesion behavior. In this case, measuring only the pull-off force with a cantilever would show quantitatively different trends, and obscure the effects of viscoelastic deformation. We anticipate that these challenges are not unique to PVAc, as viscoelasticity and load history are known determinants in the adhesion of some thin films used on MEMS/NEMS components, including SAMs and gold films [243, 282, 293, 294].

### *4.3.5 Conclusions*

We have shown three situations where the pull-off and integral methods estimate different values or trends for the work of adhesion, as measured in a cone-plane geometry. This follows an earlier observation of the same discrepancy, resulting from deformation of self-assembled monolayers adsorbed on a sphere-plane geometry [282]. This prior work, as well as the measurements with PVAc, involve "soft" material interactions where agreement with the strict requirements of a JKR-type framework is not expected *a priori*. However, neither does one generally know the mechanical properties of an interface *a priori*. That is, when only the pull-off force can be measured, one cannot know if it is an appropriate metric for a given material.

This work also shows that measuring only the pull-off force can mask the physical origins of the adhesion. In contrast, because the integral method accounts for forces at all surface separations, it is extremely sensitive to any material behavior that deviates from the assumptions of simple elastic theories, such as the JKR or DMT models. That is, the integral method can determine the work required to separate surfaces regardless of the adhesion mechanism or contact geometry. The lack of correlation between the pull-off and integral methods in some cases echoes the importance of continuing work to understand these details. In particular, the utility of the integral method is limited by the accuracy of estimating the true contact area. Further, the work of

adhesion calculated in this manner may be difficult to relate to other measurement geometries. Toward this end, a promising technique is *in situ* mechanics testing (e.g., [295, 296]), wherein contact geometries can be measured and models justified. A growing field where such breakthroughs are needed is in measuring adhesion between biological materials (e.g., cells, membranes and even individual proteins), for which pull-off forces have been used extensively [273, 278, 297]. Increasingly, MEMS/NEMS technologies are also being used to characterize these materials [265]. The development of displacement-controlled techniques with adequate sensitivity to measure adhesion forces between these materials will be of ongoing interest to both communities.

### *4.3.6 Acknowledgements*

We thank Prof. Hongbing Lu and Direk Cakiroglu for providing the PVAc and for useful discussions, and Maarten de Boer for reviewing this section.

## 4.4 Contact Electrification through Dewetting of a Nanoscale Meniscus between Oxide Surfaces

The results of this experimental investigation are in preparation and will be published elsewhere in FY11 under the authorship of Nathan W. Moore.

# 5. ANALYSIS OF METHODS FOR MEASURING INTERPHASE VISCOSITY

## 5.1 Summary

This section identifies challenges unique to measuring the effective viscosity of water interphases within nanometer-level confinement with Interfacial Force Microscopy (IFM). Particular emphasis is placed on the "drainage" and "lateral dither" methods (see Sections 5.1 and 5.2, respectively), as well as challenges common to both methods (see Section 5.3). Experiments replicating conditions relevant to measuring interfacial water viscosity with IFM suggest that the dynamical deformations (i.e., the rheological properties) of nanometer-thin water samples cannot be easily deconvoluted from the dynamical mechanical and electrical characteristics of the IFM sensor given our present understanding of the latter. Therefore, we cannot directly assess the validity of prior IFM measurements wherein viscosity values one-million times that of the value for bulk water were concluded to exist [8-10, 137]. The study herein presents several plausible alternative mechanisms of energy dissipation within the IFM measurements that have not been previously reviewed. However, additional study of the sensor dynamics, and/or use of other experimental methods, will be required to fully quantify the uncertainty in measuring the interphase viscosity using the IFM methods. Such a task would be a substantial effort that would fall beyond the scope of this LDRD project. Nonetheless, a number of ideas for improving the IFM methods have directly resulted from exploring these aspects, some of which are demonstrated herein. Alternate methods for viscosity measurement are summarized in Section 5.4.

## 5.2 IFM Drainage Method

### *5.2.1 Introduction*

The drainage method for determining the viscosity of fluid confined between two axisymmetric curved asperities (or equivalent geometry) involves moving a probe toward a surface, both submersed in fluid, at several speeds [10]. The speed-dependence of the force-distance profiles can then be related to the dissipative (viscous) properties of the fluid medium by fitting the force-distance profile to a suitable hydrodynamics model (e.g., the model of Ref.[41]) after accounting for the elastic deformation of the solid surfaces. This method has been used with IFM to infer a high viscosity among water confined between hydrophilic surfaces [9, 10]. Figure 32 shows data from one of these experiments as an example. In Figure 32a, the surfaces are hydrophilic and the force-distance profiles appear "pushed out" farther when the tip is move faster. When the surfaces are hydrophobic, the speed-dependence is greatly diminished (Figure 32b). This suggests the presence of a repulsive hydration force that is less significant when the surfaces are hydrophobic, either because of hydrodynamic slip at the water-hydrophobic interface or because the water viscosity is higher when the confining surfaces are hydrophilic, as the authors of that study concluded.

The goal of the following sections is to illustrate that such an observation can also arise from several other sources. One dominant source is lag in the output of the feedback-controlled IFM

sensor. In particular, hydration repulsion heightens lag in the feedback response of the IFM sensor. Thus, to validate this approach to measuring interphase viscosity, one must first having a detailed understanding of the sensor dynamical response—that is, of the various modes of energy dissipation within the sensor itself. These include lag when the feedback gains are set low to obtain good force-sensitivity as well as squeeze-film air dampening inherent to the sensor geometry (both are low-frequency energy loss mechanisms), and higher-frequency oscillations of the tip in response to movement into the sample. The latter can easily have amplitudes that exceed the interfacial water thickness when the feedback gains are set high to avoid the aforementioned low-frequency dissipation mechanisms. In short, for performing rheometry of nanometric thin films, the limited bandwidth of the present feedback-controlled IFM sensor presents significant challenges to quantitative interpretation. Besides hydration forces, elastohydrodynamic flattening of the tip and substrate surfaces also scales linearly with the tip approach speed and is anticipated to be significant for the IFM probe geometry when high-viscosity interphases are present; the latter may result in an overstatement of the thickness of the interfacial water thickness. Other uncertainties are identified in the following sections.

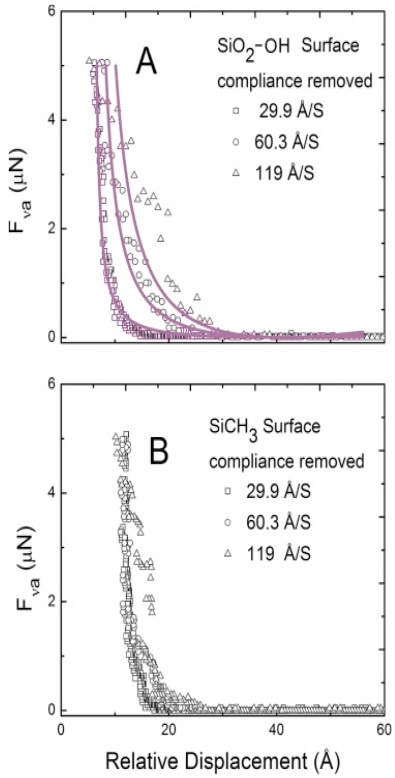


**Figure 32. Example force-displacement curves measured with IFM as a W tip approached a (A) hydrophilic or (B) hydrophobic surface submerged in water (from Ref. [10]). Data from three different rates of the approach were fit to the model of Feibelman [41].**

### *5.2.2 Lag in the Feedback Control*

#### 5.2.2.1 Existence and Significance

*5.2.2.1.1 Dynamical Response to Stepped Indentation in Fluid*

Figure 33 shows an example of the force measured in a "typical" drainage experiment, but with more detail than has been previously presented. In particular, to show dynamic information, Figure 33 shows force vs. time, rather than the more traditional plot of force vs. displacement. In this example, a diamond tip was stepped toward a clean, Si surface, both submerged in water. The tip was moved with relatively course steps of ~1Å, using the original ProbeView IFM control software [298]. The duration of each step was ~80 msec. The force was recorded simultaneously by two data acquisition systems. A high-speed data acquisition system (gray line) shows the force that the IFM sensor outputs as a function of time at much higher time resolution than recorded by the ProbeView software (circles). The ProbeView software has been used for most previous IFM experiments after c.a.2003 [298]. The latter software typically records a ~10-msec. time average of the force signal near the center of each step. For that reason, this level of detail about the sensor's dynamic behavior has not appeared in previous publications.

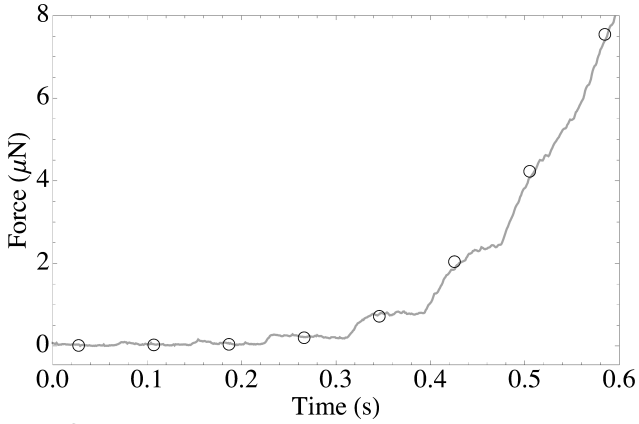


**Figure 33. Force output of the IFM sensor during a typical drainage experiment (line), showing the stepwise measurement characteristic. Circles show a ~10 msec. moving average around the center of each step interval recorded with the IFM.**

When the probe is far from the surface (near "0" time), when a step is taken, the force initially rises and then settles down quickly. The duration of the initial rise (~10 msec) is larger than the time required to physically move the tip with the piezo (~1 msec). Thus, the initial rise in force at each step arises either from hydrodynamic forces or from inertial effects of the sensor top-plate and tip mass. When the tip is very close to the surface, the force still rises at each step, but does not settle down after initially rising, indicating that the tip is pressing into the substrate elastically. At higher forces, the sensor under feedback takes longer to cancel out the new force applied at each step. At the highest loads (above ~2 μN in this example), the sensor does not fully equilibrate within the duration of each step. This behavior is distinct from what one would expect to see if the limiting dynamic mechanism was fluid drainage, which would show a decrease in force throughout the duration of each step as the fluid relaxed. Similar results (not shown) can be obtained when no fluid is present. This implies that lag exists in the IFM force sensor upon stepped displacement of the tip into a surface. The following section describes how such lag also arises when the tip is moved continuously (viz., in much finer steps), and, in fact, is a general feature of IFM that must be accounted for in dynamic measurements, such as the drainage method. That such lag can bias the interpretation of the interphase viscosity is also discussed.

*5.2.2.1.2 Sensor Response in Contact versus in Air*

It is well-known that displacement-controlled nanoindentation techniques, such as IFM, that control displacement using a feedback control circuit can exhibit significant lag in the output of the force sensor upon ramped displacement of the tip into a sample, as is typical in IFM experiments [105]. This is because the integrating portion of the controller, which is needed to remove steady-state error, will integrate error during the entire ramped-indentation where the tip encounters ever-steepening gradients of force and hence a continually larger error that continually sums, leading to lag in the control response. This lag in the control output is manifest as a lag in the position of the probe tip relative to the position prescribed by the ramp, and as a corresponding lag in the recorded force signal. This idea has not been widely recognized in the IFM community because the feedback controller is traditionally tuned when the tip is in air, rather than when it is contact with a sample, so that the response time reported for the IFM

sensor under feedback is much faster than during the experimentally-relevant ramp-loading [299], as we show in the following.

Figure 34 shows that the speed at which the IFM sensor can correct for a disturbance (e.g., the onset of an interaction with a sample) can be much slower when the tip contacts a sample. This lag has been reproduced on multiple IFM instruments, with the response time averaging 100±30 times slower at a normal load of 45 μN for four different IFM sensors with identical feedback tuning parameters. Similar results have been obtained using a variety of materials for the tip (diamond, W, glass) and substrate (Si(111), polystyrene, poly(vinyl acetate)) in both dry and fluid environments. The rise time also depends on the feedback gains. We have found that for the full range of gain values accessible on the IFM controller, for a 5-μm W probe on Si(111) in dry nitrogen, the rise time ranges ~ 20–200 ms, with the longest rise times occurring at lower gain values and higher normal loads. In all cases, this is substantially larger than the ~ 1–20 ms rise times measured by displacing the probe when it is not in contact with a sample surface, as illustrated in Figure 34b.

Qualitatively, these results are entirely expected, as first identified by Warren, et al. [105]. They concluded that the extent of lag and the resulting error in the measured force-distance profiles depends on the speed of the tip, the tuning of the feedback circuit, the tip radius, the tip and sample elastic moduli, and the presence or absence of interstitial fluid [111]. In short, the faster the tip moves (or the lower the feedback gains), the greater the lag in the probe position and the greater the error in the corresponding recorded force.

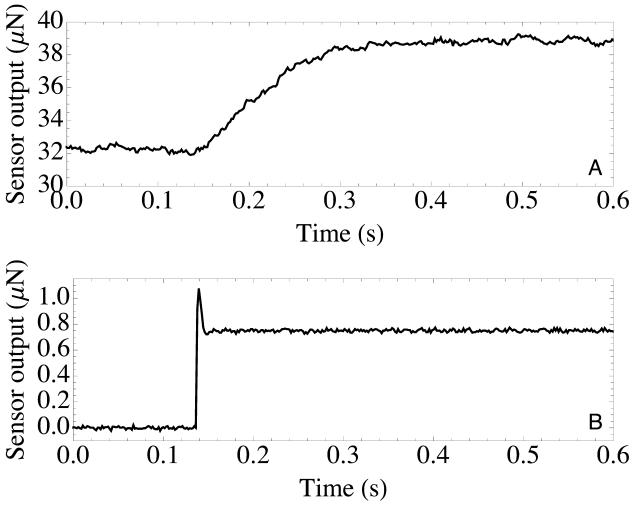


**Figure 34. Examples of measuring the transient response of an IFM sensor by separately (A) stepping the piezo with the tip in contact with a surface and (B) stepping the static bias to the error signal input to the PID controller when the tip was free in air.**

To a lesser extent, Figure 33 shows that the significance of lag in the IFM sensor also depends on the method of data acquisition (see 5.2.1 ). To simplify matters and show more detail about the sensor performance, the remainder of this section only shows data recorded with a high-speed data acquisition system and custom control software (N.Moore, 3/2009) following extensive calibration and validation, rather than the software used during previous studies of interfacial

water to control and record data [298], except where noted. This new software has several advantages. First, multiple signals can be recorded in addition to the force, such as the actual position of the probe relative to the prescribed position, which indicates how well the feedback circuit is working. Second, the piezo controlling the tip position can be moved in steps as small as ~0.01Å. This small step size improves the signal-to-noise ratio by about a factor of 15 by minimizing force from acceleration of the top-plate at each step. This allows smaller forces to be measured.

*5.2.2.1.3 Sensor Response at High and Low Values for the Feedback Gain*

Figure 35 shows an example of a series of measurements made with a diamond tip on a hydroxylated silicon substrate in "dry" nitrogen (<1% RH) at various speeds of approach (1–60 nm/sec.). Results are compared for low (A,C) and high (B,D) values of the PID controller gain (K=3, I=1; and K=25, I=10, respectively), which correspond to slower and faster response times for the sensor, respectively and relatively. Here and throughout, K, I, and D are the values of the net proportional, integral, and differential gains, respectively, on the IFM controller hardware, and D=0. The force-distance curves in the body of (B) have been smoothed using a 10-point moving average to aid comparison. The inset in (B) shows the raw (unaveraged) data for the slowest speed, showing a noise floor of ~1 μN in contact.

The distance axis of each measurement was shifted arbitrarily to align the curves at the maximum force value, following the method of Refs. [9, 10, 300, 301]. Shown this way, the curves in Figure 35a appear "pushed out", as in these prior works. Between the fastest and slowest speeds, the displacement required to achieve the same force differs by ~2 nm, also comparable to these prior works, and perhaps not coincidentally, about twice the thickness these works have reported for interfacial water. The prior interpretation of speed-dependence in the force-distance profiles measured with IFM has been to assert the presence of hydration forces, which could only be reconciled if the interphase had a viscosity many times larger than the value for bulk water. However, Figure 35a shows that this trend can be reproduced despite that there is no bulk fluid present, and that any capillary should be extremely small (Kelvin radius <1 Å) at this humidity level. Here, the speed-dependence can be explained solely by lag in the output of the IFM sensor, as is known to occur with all feedback-controlled nanoindentation instruments, such as IFM [105].

These observations do not necessarily invalidate the aforementioned works involving IFM, but do highlight the need for caution in interpreting data obtained using the drainage method. While a direct comparison with prior works is not possible, it is worth noting that the gain values used to collect the data in Figure 35b wherein no significant lag was observed were similar to the gain values used in the viscosity measurement in Ref. [10]. Lag is more significant when fluid is present, however (see section 5.2.2.1.4 Sensor Response in Dry versus Wet Contacts). The method is further detailed below.

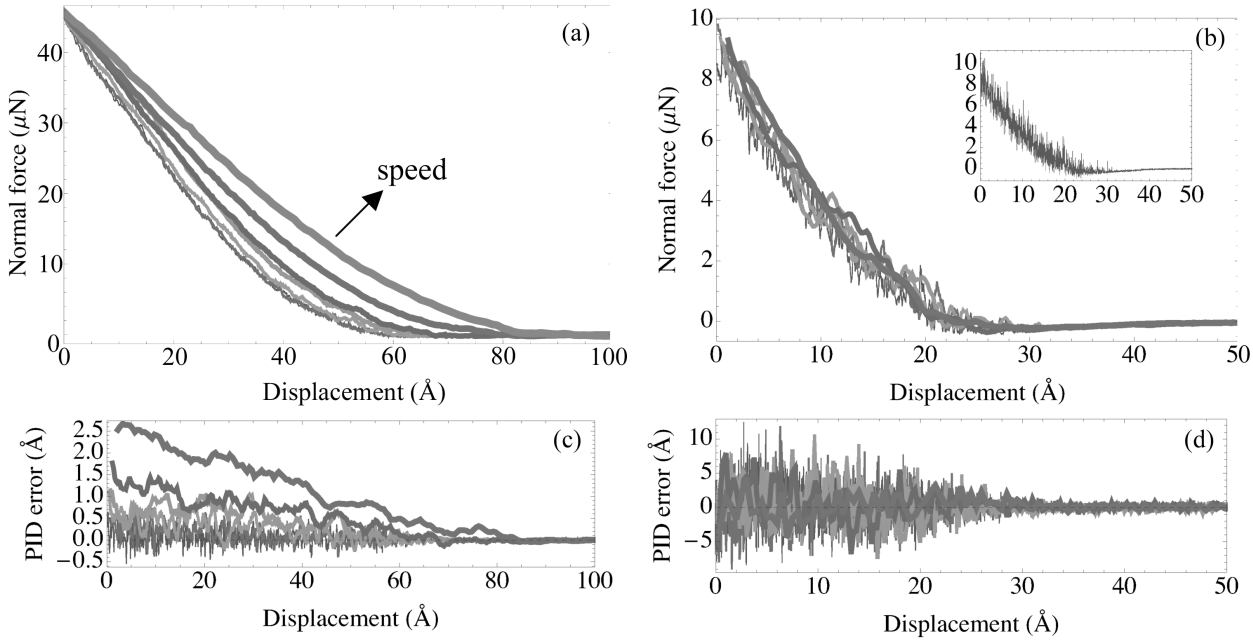


**Figure 35. (a, b) Force-distance profiles measured for a diamond tip interacting with a Si(111)-oxide surface in dry nitrogen (<1% RH). Results are compared for a sensor PID set with low (a) and high (a) gain values. In parts (a–d), the curves shown are for tip speeds of 1, 2, 5, 10, 15, 30, and 60 nm/sec. (thin to thick, respectively). The curves in the body of (B) have been smoothed using a 10-point moving average for easier comparison. The inset in (a) shows the unaveraged data for the slowest speed, showing a noise floor of ~1 μN in contact). Parts (c, d) show the error in the feedback controller calibrated to correspond to error in the tip position relative to the prescribed tip position. Gain values were (K=3, I=1) for parts (a,c) and (K=25, I=10) for parts (b,d). In Part (c), the curve thickness corresponds to the same measurement speeds as in Part (a); at the lowest speeds, the error oscillates around 0, but a stead-state error is observed for the upper-most curves, which directly corresponds to the fastest measurement speeds.**

Figure 35(C, D) shows the error in the sensor's ability to maintain the tip in the desired position. This is the output of the demodulator board on the PID controller calibrated to represent the instantaneous, near-vertical displacement of the tip arising from error in the PID control and the resultant rotation of the top-plate. The demodulator was calibrated by resting the tip onto a sample surface with the feedback disabled while moving the sensor toward the sample with a calibrated piezo, and calculating the linear constant of proportionality between the piezo movement and the demodulator voltage. The calibration constant depends on the feedback tuning constants and the particular sensor, but typically ranges 40–600 Å/V. Note that when the feedback control is active, vertical deflection of the torsion bars can become the most compliant axis of the sensor; however, probe displacement arising from this effect is not measured with the current IFM sensor (see 5.3.4.1 Torsion Bars). Therefore, the positional error that we report is a lower bound for the true value.

Lag in the force sensor is identified by the growth of a psuedo-steady-state error at faster speeds (Figure 35c). The sensor lag is what causes the speed dependence in the force-distance profiles in (Figure 35a). In Figure 35b, the sensor was tuned to eliminate lag by setting the proportional gain

to higher values. This was accomplished at the expense of increasing the noise floor substantially (Figure 35b inset). Under these conditions, the tip was "jack hammering" the surface with a peak-to-peak amplitude of ~1-nm, representing a potential source of energy dissipation that has not been previously accounted for.

One way to quantify the effect of lag on the measured repulsive force is to fit the portion of the force-distance curve involving repulsive force to the model of Johnson, Kendall, and Roberts (JKR) [228] to determine the reduced Young's modulus of the dry tip-substrate contact. Table 5 shows results for a measurement speed of 5 nm/sec for several values of the proportional and integral gains, corresponding to the respective settings on the IFM controller. This speed of approach corresponds to a typical measurement speed in an IFM experiment, neither excessively fast nor excessively slow. These results show that the measurement of repulsive force is highly sensitive to the feedback tuning, and particularly to the integral gain value, as discussed above.

Conversely, we have done additional measurements wherein the feedback gains were fixed at "low" values (K = 1 and I = 1) to represent situations wherein low-noise force measurement is required (e.g., in probing interfacial water) so that the oscillation of the probe position is smaller than the fluid layer being probed (<1 nm). In such cases, lag could not be detected when the tip speed was <1 nm/s. However, higher tip speeds are required to accurately measure hydration forces within interfacial water films, owing to thermal drift of the interface.

**Table 5. Measured contact modulus as a function of Sensor Tuning for a 6-μm radius W-oxide Tip Interacting with Si(111) at <1% RH.**

| Net proportional gain (K) | Integral gain (I) | Reduced contact modulus (GPa) |
|---|---|---|
| 1 | 2 | 46 |
| 2 | 2 | 76 |
| 2 | 1 | 8.5 |

*5.2.2.1.4 Sensor Response in Dry versus Wet Contacts*

Immersing an IFM tip in water near a surface slows the sensor response considerably compared to when the tip is in a dry contact, under otherwise identical conditions. Figure 36(left) shows an example of two measurements at a moderately fast rate of approach (15 nm/s) with the IFM PID controller set at low and high values (blue and purple dots, respectively). The approach curves are nearly coincident, and only by the hysteresis in the approach and retract curves (Figure 36(right)) is the small lag in the sensor response evident. The lag was easily removed by setting the gains to higher values (data not shown; see Figure 35 for an example).

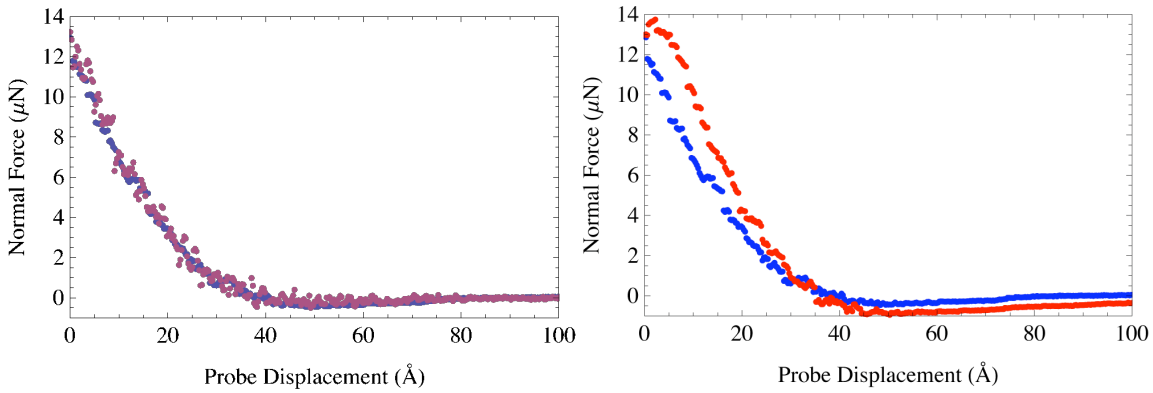


**Figure 36. Left: Force-distance curves measured during the approach of a W-oxide tip toward a hydroxylated Si(111)-oxide surface at <0.1% RH at a rate of 15 nm/s for two settings of the net proportional gain of the PID controller: K = 1 (blue curve) and K = 5 (red curve). The integral and derivative gain values were 1 and 0, respectively, in both cases. Right: Approach (blue) and retract (red) curves for the low-gain case.**

The situation changes when the probe and sample are immersed into fluid (Figure 37). Here, the gains on the IFM controller were set to the same values as that of the high-gain case shown Figure 36 for which lag was insignificant. Many of the experimental conditions were chosen to mimic earlier experiments by Goertz, et al. [10], using identical materials (W-oxide against hydroxylated Si(111)-oxide in ultrapure water) and similar cleaning procedures. Significant differences include: 1) the tip radius was 5.1 μm, rather than 500 nm, to avoid severe blunting of the probe; 2) the Tungsten-oxide tip was cleaned in ethanol rather than strong acid to avoid pitting the tip; 3) here the ProbeView control software was used to control the probe and record data, whereas in Ref.[10] the ProveView program was only used to control the probe and data were collected on a digitizing oscilloscope [302]; 4) the fastest tip speed here (50 nm/s) was ~4× faster than in Ref.[10] to exaggerate the effect of moving the probe quickly, though slower speeds are also shown in Figure 37; 5) the net proportional gain set on the PID controller (K = 5 here) was ~4× smaller than in Ref.[10] ([302]); and 6) the force setpoint at which the indenting tip was retracted from the interface was ~5× larger than in Ref.[10]. Under these conditions, lag in the feedback-controlled IFM sensor can be expected to be larger than what would be expected under the conditions of the experiment of Ref.[10], which is useful for illustrating the key parameters determining the lag. A total of 20 speeds over the range 4–50 nm/s were investigated and gave self-consistent results. Only measurements at speeds of 4, 30, and 50 nm/s are shown for clarity. Both substrate and tip were very hydrophilic (the Si substrate had a contact angle of ~5º, and the tip formed a large meniscus when immersed in water). As well, the distance values for each curve in Figure 37 were shifted to align each curve at the point of maximal force measured at the fastest speed. This analysis procedure replicates that of the drainage experiment in Ref.[10].

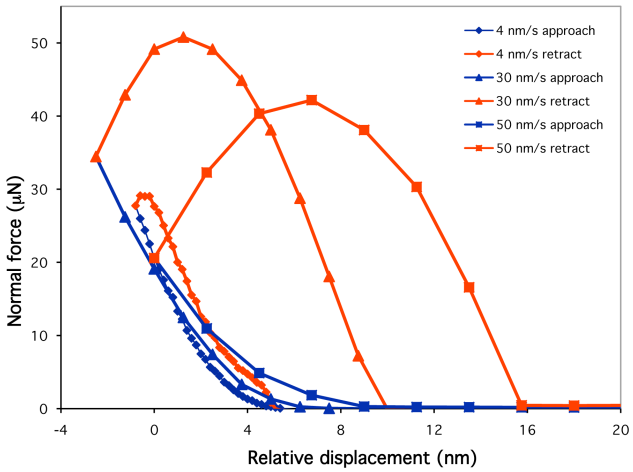


**Figure 37. Force-displacement curves measured with the same tip and sample as in Figure 36 immediately after placing a droplet of 18.2 MΩ water into the contact region. Shown is the force measured during the probe's approach (connected blue points) and withdrawal (connected red points) at three different tip speeds.**

With the probe in fluid, even at measurement speeds much slower than those in Figure 36, the sensor output lags behind the measurement considerably. The curves at higher speeds measured during the tip's approach appear to be "pushed out", that is, more repulsive at a given displacement. Such effects have previously been attributed a high viscosity for the water interphase(s). However, from this experiment, it is clear that the same effect can arise from lag in the IFM sensor. This is evidenced as large hysteresis and a rise in force beyond the turn-around point in Figure 37, as well as a non-zero error in the PID controller (demodulator signal) when the tip is near to or touching the surface (recorded simultaneously but not plotted here; see Figure 35c for an example). Prior studies of interfacial water using IFM have not documented the force measured during the tip's retraction nor the PID error (demodulator signal) [9, 10, 300, 301]. Therefore, it is impossible to assess if the anomalous viscosity values inferred from these prior works can be attributed to lag in the sensor response. Regardless, Figure 37 shows that the effect can be significant even for relatively slow tip speeds (e.g., 4 nm/s) if the net proportional gain setting is relatively low (e.g., K = 5). This demonstrates the need to control for this effect when using feedback-controlled nanoindentation tools, such as IFM, to measure thin-film viscosity using the drainage method.

*5.2.2.1.5 Software accuracy*

Lag in the sensor response, which can ordinarily be identified as a large inverse hysteresis between the force-distance curves measured during approach and withdrawal of the tip from the sample (Figure 37), is not evident when data is plotted on the ProbeView IFM control software used in at least some of the previous interfacial water experiments [298]. This is because of an error in the software. When plotting the approach and withdrawal curves together, the software uses the point of maximal force to determine the point at which the tip reversed direction, rather than the actual reversal point. This works acceptably when no hysteresis exists between the force-distance curves. However, when hysteresis is present, lag in the sensor response appears only as a small change in the derivative of the force-displacement curve that is not generally distinguishable by eye at computer screen resolution. This gives the illusion that the force output

of the sensor does not lag behind the rate of displacement. The software does record the data correctly, however.

### 5.2.2.2 Compensation Strategies

*5.2.2.2.1 Feedforward Control*

The best method for eliminating lag in displacement-controlled nanoindentation experiments may be to use feedforward control instead of feedback-control, as demonstrated by Warren at al. [105]. In general, this requires extensive sensor characterization and development of custom algorithms and electronics, and is beyond the scope of this project.

*5.2.2.2.2 Increasing Feedback Gains*

Increasing feedback gains decreases sensor lag at the expense of increasing the amplitude of oscillations of the tip in response to changes in external force from the tip-sample interaction and/or from external mechanical vibrations or tip movement. In such cases, the resulting variation in the probe position can easily exceed the thickness of the interfacial water layer (1–2 nm), so that it is impossible to measure the rheological properties of only the fluid (e.g., see Figure 35(b,d)).

*5.2.2.2.3 Empirical Correction*

The lag in the response of the IFM sensor that arises at the low feedback gain settings required to achieve high force sensitivity at the measurement speeds required for the drainage method can be empirically corrected. However, this correction is only based partially on physically-measurable parameters. Further, the method does not achieve results superior to what could be obtained using a cantilever-based force sensing method (e.g., AFM) without feedback stabilization of the tip. Therefore, this correction is of little value without further development. The method and example results are briefly described below.

Figure 38 shows an example IFM measurement involving a diamond tip interacting with a Si(111)-oxide surface at <1% RH with "low" gain settings (K = 3, I = 1). The hysteresis between the force-distance curves indicates lag in the sensor response, which is confirmed by recording the error signal of the PID controller, shown here as a value that is calibrated to correspond to the actual deflection of the tip relative to the setpoint as described previously. The latter was calibrated by displacing the sensor toward a surface with the sensor in open-loop (feedback off), while recording the voltage of the demodulator output, which is the PID error in volts. The tip was moved with a piezo that was calibrated against both a standard electromagnetic displacement gauge and a NanoCube™ XYZ Piezo System (Physike Internationale, Model P-615), both giving identical calibration factors within ±3%.

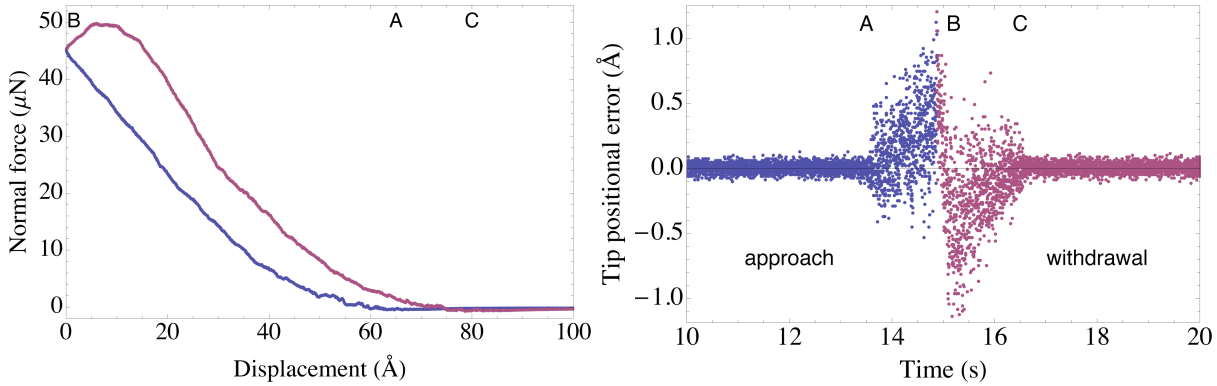


**Figure 38. Left: example force-distance curve measured with IFM during the approach (blue; bottom curve) and withdrawal (red; upper curve) of a diamond indenter toward a Si(111)-oxide surface at <1% relative humidity. Right: Recorded error in the tip displacement relative to the controller set point, indicating lag upon approach (blue) and withdrawal (red). Letters indicate the approximate moment of (A) initial contact between probe and substrate, (B) reversal of the direction of probe movement, and (C) last contact between probe and substrate.**

The method used here for correcting the data to account for lag in the sensor output amounts to shifting the distance values by an amount equal to the positional error times an arbitrary scalar ($S$) that is varied until the approach and withdrawal curves lie on top of each other. An example result is shown in Figure 39(left) for $S$ = 15. The deviation of this scalar from 1 cannot be explained at present, which prevents certifying this method of data correction. As well, with this correction method, noise in the error signal propagates into the force-displacement profile. Figure 39(right) shows the elastic modulus that would be inferred from several measurements both with and without this displacement correction, for different measurement speeds. It is clear that erroneous physical properties are obtained with low PID gain settings and fast rates of approach if this correction is not applied.

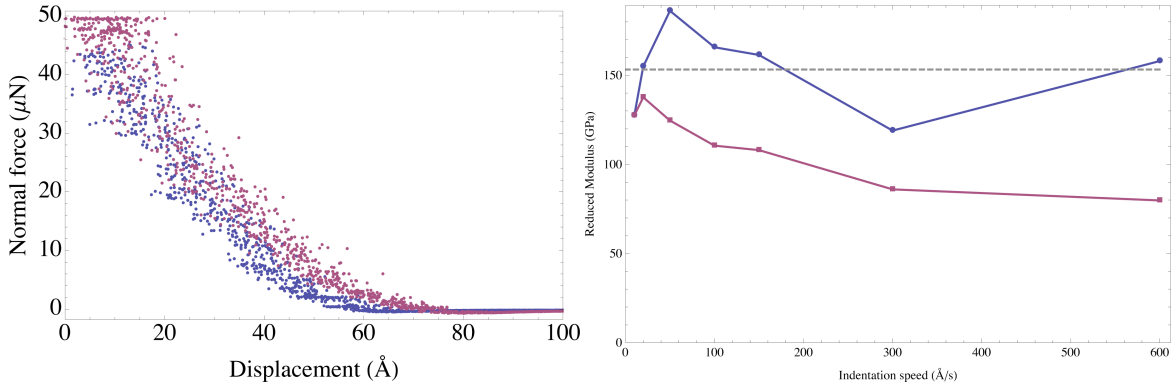


**Figure 39. Left: Example force-distance curve after correcting for error in the probe position arising from lag in the PID control scheme. Right: Comparison of the elastic modulus inferred from several measurements at difference rates of approach and withdrawal, before (red, lower set of points) and after (blue, upper set of points) correcting for lag in the sensor response, relative to the expected value (dashed line).**

*5.2.2.2.4 Open-Loop Operation*

Operating the IFM in open loop (feedback disabled) eliminates lag in the sensor output from the integrator portion of the PID. Some lag may still exist from air damping within the capacitor gap of the sensor. Atomic force microscopy (AFM) may provide a more versatile platform for such measurements of fluids in open-loop, however.

*5.2.2.2.5 Reduce Measurement Speed*

Reducing the tip's speed of approach minimizes sensor lag, but also decreases sensitivity to measuring hydrodynamic forces. Alternately, to avoid complication from sensor lag with feedback-controlled nanoindentation, one can study material systems with deformation timescales much longer than the lag. An example is the investigation of the viscoelastic properties of Silly Putty™ (Binney and Smith) [303, 304]. The measurement was made by making a single step with the IFM tip into the sample, and recording the force's decay over a ~3 sec. period as the polymer relaxed. The largest timescale for the sensor response that has been measured in any condition is ~200 ms (when indenting Si(111))[111], but can be expected to be much smaller (~ 1-20 ms) when the tip indents Silly Putty, which has an interfacial stiffness ~4 orders of magnitude smaller than Si [105]. (Here, interfacial stiffness is defined as the gradient of the interfacial force with respect to the probe's displacement into the sample, and was estimated here using the Hertzian theory of elastic, single-asperity contact [267] by assuming bulk, zero-frequency elastic modulii at room temperature for the materials, tip radii, and characteristic indentation depths of the respective studies.) Because the lag is much smaller than the measurement time, the lag is insignificant in the experiment involving Silly Putty™. Second, in that experiment the lag can be reduced by increasing the feedback gains without further consequence. The increased noise in the force signal that would result upon contact with the sample and the tip's resulting oscillation around the positional set point would not be significant because of the large thickness of the sample with respect to the tip oscillation amplitude [303, 304].

### *5.2.3 Continuous vs. Stepwise Tip Movement*

The effect of continuous vs. stepwise movement of the tip through an interfacial water layer and into a surface has not been rigorously evaluated with respect to how the results or interpretation may change. However, two qualitative observations can be made.

First, moving the probe with smaller steps results in a lower noise floor in the recorded force and smaller oscillation of the probe position than taking larger steps. For example, the original IFM control software used for previous interfacial water experiments is not capable of moving the tip with steps smaller than ~0.25Å or at rates greater than ~16 steps per second [298]. By reducing the step-size to ~0.02Å and increasing the stepping rate to 500 steps per second, a 15× reduction in noise floor has been achieved, corresponding to control of the probe position of 0.2Å-rms. The finer control over probe position is advantageous for these studies, because less energy is dissipated into the water film from the then-lower amplitude of the damped-oscillation of the tip that follows each step that the probe takes toward the surface.

Second, in the ProveView IFM control software, the rate of stepping and data collection are coupled and involve heavily-averaging the force signal in time (typically a 10-msec. moving average) before the force is recorded. This reduced time resolution can mask key features of the sensor performance, as shown in Figure 33.

### *5.2.4 Method Sensitivity*

The smallest viscosity that can be determined using the drainage method depends on the sensitivity of IFM to drainage (hydration) forces. This can be estimated using Feibelman's expression for the drainage force with respect to the nominal separation of tip and substrate:

$$F = -6\pi\eta v(R^2/D))(1-(D/w))^2 \qquad (1)$$

The smallest force that can be measured with the current IFM in a quasi-static mode (non-oscillatory mode) is ~10 nN. Then, using Eq.1b, for a typical tip radius $R$=500 nm, interphase thickness $w$=1 nm, and intersurface separation of 1Å, the smallest viscosity that can be inferred using the drainage method is 0.1 Pa·s, or ~$10^2$× the viscosity of bulk water, based solely on limitations of the instrument sensitivity. Then, any viscosity value inferred from IFM using this method will appear much larger than the bulk value for water. This also shows that the drainage method is more sensitive than the lateral dither method for measuring interphase viscosity (see 5.3.5.1 Method Sensitivity).

### *5.2.5 Possible Sources of Systematic Error in Viscosity Determination*

#### 5.2.5.1 Squeeze-Film Air Damping

Because the capacitor gap of the IFM sensor is only ~6 μm in height, movement of the top-plate in response to a tip-sample interaction is expected to give rise to a significant damping force arising from squeeze-film flow of air within the capacitor gap. Top-plate rotation will occur when the feedback mechanism is not able to compensate fast enough for changes in force, such as during ramp loading or oscillation. An upper bound for the systematic error introduced from

squeeze-film air damping can be estimated as follows. The damping coefficient associated with rotation of the sensor top-plate is given by Ref.[305]: $\beta_t = 8\eta L^6\zeta/(15D^3)$, where $\eta$ is the air viscosity ($1.82\times10^{-5}$ Pa.s), $L$ is the half-length of the top-plate (~4 mm), $D$ is the capacitor gap spacing (~6 μm), and $\zeta$ =0.82 is an aspect ratio coefficient [306], so $\beta_t = 1.5\times10^{-4}$ N m s rad$^{-1}$.

To estimate the corresponding force at the tip position, if one assumes a maximum top-plate displacement of 2-nm corresponding to the thickness of two layers of interfacial water and an average tip approach speed of 12 nm/s corresponding to the experiments in Ref.[10], then the average angular velocity is $d\theta/dt$ = 6 μrad/s, and the torque damping coefficient is $\tau = \beta_t (d\theta/dt)$ = $9.1\times10^{-10}$ N·m. Then, the force at the tip point arising from the air squeeze-film damping is $2\tau/L$ = 0.45 μN. This value for the force associated with air damping is an upper bound because it assumes that the feedback mechanism is not able to compensate at all for changes in external force on the tip. This force value is significant with respect to the instrument resolution (0.03 μN), but is still much smaller than the increase in force shown in the force curves of Ref. [10] at speeds twice and four times the slowest speed (~4 μN). Therefore, squeeze-film air damping likely only contributes a small (<10%) systematic error in inferring the viscosity of interfacial water using the drainage method.

#### 5.2.5.2 Elastohydrodynamic Considerations

In modeling the dissipative forces measured with IFM for probes moving within viscous interphases, it has always been assumed that the probe and substrate are perfectly elastic. Under static loading, the probe and substrate are not anticipated to deform significantly under the experimental conditions, based on standard contact-mechanics models, such as the JKR theory [228]. However, Landman, et al. [307], suggested that surface deformation and fluid flow should be considered coupled phenomenon when describing the principles of what is recognized as the field of elastohydrodynamics:

> "When two nonconforming solid surfaces come into contact in the presence of a liquid lubricant (or when two asperities of nominally conforming surfaces, under conditions of boundary lubrication, come together), the pressure developed in the contact zone may achieve such high values that local elastic deformations of the surfaces must be included in proper treatments of lubrication of the tribosystem… Inherent to [the] continuum models are certain assumptions which are used as input into the calculations. These include constitutive relationships such as rheological properties of the lubricant film (Newtonian or non-Newtonian viscosity laws, as well as pressure and temperature variations of the viscosity) and mechanical response characteristics of the bounding surface materials (substrates and asperities), as well as imposed interfacial liquid-solid boundary conditions." [307]

As well, intersurface forces are known to influence the shape of asperity contacts, and to influence static-force measurements with the Surface Forces Apparatus when the interfacial separation is < ~3 nm [308]. However, neither of these effects have been previously considered in modeling IFM experiments addressing interfacial water. Their relative importance on the drainage experiment can be estimated using the formulation of Chan and Horn [309], who determined the amount of elastic deformation of the probe center along the surface normal as:

$$\delta D = (3/4)\pi\eta c[(1-\sigma^2)/E^*](2R/D)^{3/2} \qquad (1c)$$

where $\eta$ is the fluid viscosity, $c$ is the surface approach speed, $\sigma$ and $E^*$ are the Poisson ratio and reduced elastic modulus of the interface, and $R$ is the probe radius. Note that the tip deformation scales linearly with the approach velocity, as does the hydrodynamic force [41]. Therefore, it is important to determine if the tip deformation is significant before using the drainage method to determine viscosity.

Table 6 lists values calculated with Eq.1c using parameters from several previous IFM experiments involving interfacial water. In all cases, characteristic values of $\sigma$ = 0.3, $c$ = 10 nm/s, and $D$ ranging 0.25–1.0 nm were assumed. The calculated values show that, in all cases, the elastic deformation of the probe is expected to be comparable to or much greater than the thickness of the viscous layer of water (~ 1 nm). Therefore, if the interfacial water viscosity is, in fact, many orders of magnitude higher than the value for bulk water, it would seem necessary to account for the deformation of the IFM probe under the influence of hydrodynamic drag in order to extract an accurate viscosity value. We also note that subtracting the elastic compliance of the interface using Hertzian contact mechanics does not properly account for the elastohydrodynamic deformation that ocurrs before the tip and substrate contact each other [307]. Elastohydrodynamic deformation is insignificant if the interphase viscosity equals the bulk value (~$10^{-3}$ Pa.s), however.

For comparison, we also estimate the elastohydrodynamic deflection of an AFM tip that was used in an experiment to measure the viscosity of OMCTS fluid molecules confined between an AFM tip and mica [140]. Parameters are taken from Ref.[140], giving $\delta D$ = 0.001Å (Eq.1). One reason that elastohydrodynamics is insignificant for AFM experiment, but not for IFM, is because of the small tip radius used for AFM ($R$ ~10 nm) compared to IFM ($R \geq$ 500 nm).

**Table 6. Comparison between the estimated elastohydrodynamic deformation of the IFM probe and substrate interface (Eq.1) based on experimental parameters and previously reported values for the interphase viscosity, and the reported interphase thickness.**

| Probe material | Substrate material | Reduced modulus (E*, GPa) | Probe radius (R, nm) | Interphase viscosity (η, relative to bulk) | Probe deformation (δD, nm)* | Reported interphase thickness (nm) | Ref. |
|---|---|---|---|---|---|---|---|
| W (etched) | Hydroxylated Si(111)-oxide | 38 | 500 | $10^6\times$ | **1.4–12** | **0.7–1.7** | [10] |
| SAM-$CO_2$H coated Au (etched) | SAM-$CO_2$H coated Au(111) | 13 | 500 | $10^7\times$ | **8.4–66** | **≤1** | [8] |
| SAM-OEG coated polycrystalline Au | SAM-OEG coated polycrystalline Au | 19 | 500 | $10^6\times$ | **0.5–4** | **≤5.5** | [9] |

* for D from 0.25–1.0 nm.

#### 5.2.5.3 Plastic Deformation of Asperity Contacts

Soft, amorphous materials, such as the SAM-coated Au tips used in the first IFM study of interfacial water are particularly susceptible to plastic deformation at low levels of force via deformation of the Au tip or Au coating [300]. Such plastic deformation is a potential source of energy dissipation. The lack of observable excursions in force-distance curves does not necessarily indicate the absence of plastic deformation [105]. A clear sign of plastic deformation would be hysteresis between the force-distance curves measured during a probe's approach and withdrawal into a sample, after the effects of fluid drag are properly accounted for. However, this possibility cannot be retroactively evaluated because the required data (the retraction curves) for the published IFM experiments on interfacial water have not been reported. Force-distance curves measured with IFM for dry, stiffer materials do not generally show such hysteresis [111].

Further, the deformation of a scanning probe near a surface within a fluid, either elastically or plastically, is not strictly independent of the fluid shear forces imposed (see 5.2.5.2 Elastohydrodynamic Considerations). It is also possible that some energy may have dissipated through the SAMs confining the interfacial water in the experiments of Refs. [8, 300], which would make the extraction of only the fluid properties a complicated matter.

#### 5.2.5.4 Numerical Propagation of Parameter Uncertainties

For sake of example, we consider only a single-point calculation of the viscosity using the model of Feibelman [41] for the drainage force, by inverting the relation between hydrodynamic force and displacement to calculate the viscosity at a single separation ($D$ = 9Å) for a tip velocity ($v$ = 10 nm/s), tip radius ($R$ = 0.5 μm), and for the minimum measurable force of ~30 nN. This approach is undoubtedly less accurate than fitting multiple points. We assume generous error bounds in estimating the tip radius (±100 nm), tip position (±1 nm), and interfacial film thickness (±4Å). Then, through standard propagation of errors, it can be shown that the uncertainty in the viscosity value arising from these sources of uncertainty is at most about one order of magnitude.

#### 5.2.5.5 Nonparallelism between Sample, Top-plate, and Sensor

As described below, nonparallelism between the sample, sensor top-plate, and sensor capacitor pads is anticipated to alter the measurement of fluid viscosity in two manners. First, a systematic error in the measured forces can arise. Second, when force is applied to the probe (either normally or laterally) the top-plate will translate as well as rotate because of geometric asymmetry inherent in the sensor design. This allows additional energy dissipation via squeeze-film air damping (see 5.2.5.1 Squeeze-Film Air Damping).

Table 7 lists the depth of the force well (the maximum adhesion force) measured during a force-distance profile with IFM for several angles of the plane of the IFM sensor holder relative to the sample holder. Measurements were made with a 100-μm annealed glass tip interacting with Si(111) in humid air (~30% RH). Table 7 also lists the composite elastic modulus determined for the tip-sample interface determined by fitting the force-distance profiles to the JKR model for elastic compression in the presence of adhesion [228]. Both the adhesion force and the composite modulus change significantly with tilt of the sensor relative to the sample. The change in both metrics is less than an order of magnitude. A few percent of the variation from tilt can be

attributed to change in the direction of the net vector of force applied to the tip. Another possibility is that the tip may have irregular shape at the nanometer scale. This observation motivates further study to determine if the variation arises from irregularities of the tip shape, asymmetries in the single-asperity contact from tilt alone, or if it is a feature of the IFM method.

**Table 7. Effect of sensor tilt on measurement of adhesion force**

| Tilt (degrees) | Depth of force well (μN) | Composite modulus (GPa) |
|---|---|---|
| -2 | -1.9 | 92 |
| 0 | -1.8 | 87 |
| 0.5 | -3.4 | 79 |

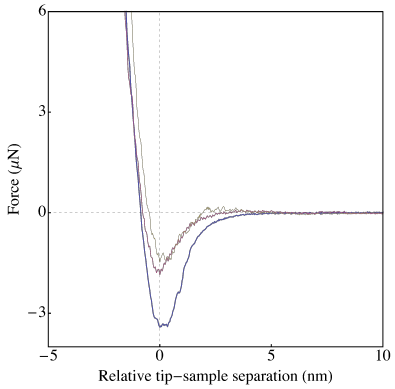


**Figure 40. Force-distance profiles measured with IFM with the sensor tilted at several discrete angles relative to the sample, c.f., Table 7.**

A possible affect of tilt between the top-plate and underlying capacitor pads is described as follows Figure 41a illustrates the typical assumption that the IFM sensor is parallel to the sample and that both plates forming the capacitor gap are parallel. Neither assumption is generally true. The sensor is not generally aligned with the sample to better than 2º, and the tips have typically been mounted ≤6º off of the normal. As well, the weight of the tip will cause the top-plate to rotate before the feedback is engaged. The geometry shown in Figure 41b is the "zero error" positional reference that the sensor electronics are tuned to maintain. When the tip encounters an interaction force with the sample (normal or lateral), this produces a torque and a small lateral displacement that, because of the nonparallelism, will result in a change in differential capacitance between each side of the teeter totter (Figure 41). The feedback circuit will then rotate the top-plate to try to nullify the differential capacitance back to the starting condition shown in Figure 41b. Thus, because of nonparallelism within the sensor, the lateral compliance of the sensor is coupled with the normal compliance. This gives rise to a lower-than-expected compliance for the IFM sensor along the normal coordinate, depending on the interaction force, the extent of tilt of the sensor relative to the sample, and of the tip relative to the sensor. It can be shown that this effect produces error in the displacement axis of force-displacement curves on the order of a few angstroms to several nanometers for tilt angles <5º. However, because the

process is conservative, it is not anticipated to significantly affect the measurement of interphase viscosity.

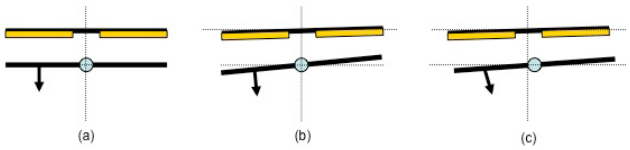


**Figure 41. Schematic of rotational states of the IFM sensor: (a) typical assumption (parallel plates, parallel to sample), (b) actual geometry without feedback, (c) actual geometry in response to an interaction force with the sample. Arrow represents the IFM tip. Not to scale.**

### *5.2.6 Summary*

Lag in the output of the IFM force sensor upon ramped displacement near or into an interface is a general feature of feedback-controlled nanoindentation, such as IFM, that if unaccounted for can give the false appearance of rate-dependant material properties, such as hydration repulsion or viscoelasticity of an interface, and hence anomalous values when determining the interphase viscosity using the drainage method. The error in the force measurement depends on the tip speed, the feedback tuning, the elastic moduli of the tip and substrate, the tip radius, and the presence or absence of interstitial fluid. Lag can be identified either as inverse hysteresis between the force-distance curves measured during the tip's approach and retraction from a surface or as a steady rise in the positional error of the tip effected by the feedback loop during indentation (viz., the IFM controller's demodulator output voltage). Recording the latter along with the force and distance information during the probe's approach allows one to assess the severity of lag in the IFM sensor and to estimate the resulting error in the probe position. Neither metric has been reported in previous studies of interfacial water involving the drainage method [9, 10]. Therefore, an assessment of the validity of these prior works cannot be made. As well, if the interphase viscosity is in fact significantly larger than the bulk value, an accurate determination of the interphase thickness will require accounting for elastohydrodynamic deformation of the probe and opposing substrate.

Sensor lag can be reduced by setting the feedback gains on the IFM controller to higher values. However, this introduces tip oscillations with amplitudes that are a significant fraction of the presumed interfacial water thickness that must be accounted for in the analysis. For these reasons, the present IFM configuration is not well-suited for characterizing rheological properties of nanometric thin films, such as interfacial water. Two solutions that could be developed include using feedforward control (rather than feedback control) and making empirical corrections for the tip position based on calibrating the PID error signal in terms of tip displacement. However, it may be more tractable to perform such experiments in open-loop (e.g., with AFM) or by using small-amplitude, oscillatory AFM techniques that are already fully characterized [310]. Alternately, measurement speeds may be reduced; however, without a validated model for the sensor dynamics, extracting accurate viscosity values from the then-lower hydrodynamic forces may be problematic. Because of instrumental sensitivity, the

drainage method with IFM is presently limited to measuring viscosity values > ~ 0.1 Pa·s, or ~$10^2\times$ that of bulk water.

## 5.3 IFM Lateral Dither Method

### *5.3.1 Introduction*

In this method, the IFM sensor to which the tip is mounted is oscillated laterally by actuation of a piezo element, typically at frequencies of 90–100 Hz and amplitudes of 7–10Å. A lock-in amplifier is used to measure the component of the sensor response (force) corresponding to the frequency of oscillation. The relative phase between the piezo drive and the sensor response is also recorded. The lateral dither method has been used with IFM to infer large viscosity values for water confined between a surface and IFM tip both submerged in water, for a water meniscus formed between an IFM tip and surface in humid air [8, 10], in a water bath, and for the liquid-like layer (LLL) on ice [28]. Similar viscosity values (~$10^6$ times the bulk value) were obtained in each case.

The assumptions in the analyses in Refs.[8, 10, 28] of the IFM experiments include:

- the response time ($\tau$) of the IFM sensor under feedback is much smaller than the inverse frequency ($1/f$) at which the sensor assembly is dithered, so that the phase lag from the IFM electronics is constant and only the material interaction is measured.
- the torsion bars can rotate along their axes, but are noncompliant along the normal and lateral coordinates,
- the probe oscillation is parallel to the substrate,
- the probe shank, sensor top-plate, and sensor and sample mounting hardware are rigid, inelastic bodies,
- the sample and probe tip are axisymmetric, inelastic bodies,
- the probe's rate of advance toward the surface is much slower than its average lateral speed,
- the confined fluid (confined bulk water, meniscus, or LLL) is a Newtonian fluid,

Under such cases, the lateral and normal forces on the probe can be easily separated using the magnitude and phase output values of the lock-in detector, as described in Ref.[10]. Then, the model of Ref.[131] can be used to determine the fluid viscosity from the frictional (dissipative) component of the lateral force as a function of the nominal probe-substrate separation as described in Ref.[10].

Here, we present several observations and analyses to test these assumptions. We conclude that qualifying this method for viscosity measurement will require a more detailed understanding of the dynamical characteristics of the IFM sensor than is presently available.

### *5.3.2 Sensor Dynamical Characteristics*

The assumption that the response time of the IFM sensor is fast enough to keep up with changes in the force on the probe tip during a lateral dither is valid when the IFM probe is dithered in air but is not always true when the tip contacts the substrate (see also section, 5.2.2 Lag in the Feedback Control). It is well known that measuring viscoelastic properties with a scanning probe requires that the dynamical properties of the entire mechanical train (probe tip / sensor / feedback and detection electronics) first be determined (e.g., [105]). This is particularly important when the measurement frequency (e.g., 90–100 Hz for the interfacial water measurements) is near the resonant frequency of the sensor (e.g., ~80 Hz for the IFM sensors used in this study) [310]. After the dynamical properties of the measuring instrument have been determined, a suitable model can be used to relate the measured amplitude and phase of the tip movement to the damping characteristics (e.g., viscosity or stiffness) of the sample with which the probe interacts when it is dithered within the sample.

In contrast, previous analyses of interfacial water experiments wherein the tip was dithered to measure viscosity have assumed that the amplitude and phase of the lateral force measured with IFM in this manner is independent of the measurement frequency, so that only the sample response need be modeled. This approach is not valid when the dither frequency is near the resonant frequency of the oscillating element [310], as is the case with the IFM experiments. Warren, et al. [7], were the first to develop a model for an early-generation IFM to deconvolute the responses of the sample and the sensor under feedback. Even with modification to account for known differences between the older and newer IFM sensor designs, Warren's model does not accurately account for the movement of the IFM sensor in response to a sinusoidal disturbance (described below). One limitation is that even in its simplest form, the model involves 12 parameters, not all of which can be measured accurately, and vary widely for different IFM sensors. As well, the IFM sensor has three degrees of freedom that are not accounted for in this model, and that are not easily characterized. Developing a suitable model is beyond the scope of this LDRD. The 2$^{nd}$-Generation IFM [311-313] has one fewer degrees of freedom, but still cannot detect deflection of the top-plate along the surface tangent, representing a mode of energy dissipation that cannot be accounted for with the current IFM sensor designs.

The following subsections show experimental evidence that the measured sensor response (amplitude and phase) under the lateral dither method is a convolution of the sensor and material responses.

#### 5.3.2.1 Stiffness-Dependent Phase Response

In measuring the viscosity of interfacial water with IFM, it has previously been assumed that the output of the lock-in amplifier used for lateral force detection is related only to the material interaction. The material interaction is further assumed to be represented by a single Maxwell element (spring and dashpot in series). The dynamics of that situation correspond to a single, damped harmonic oscillator, which has well-known analytical solutions describing the oscillator position as a function of time for an arbitrary level of damping. In such cases, the phase lag between the driving force and the oscillator response can only range 0–180º. Figure 42 shows an example where this is not true. Here, the phase ranged over 360º during the course of measurement, as seen by monotonic flips in sign of the phase between -180º and +180º. For

clarity, Figure 42b shows the phase after correcting for these sign flips to show that the change in phase is monotonic throughout the measurement. The phase was also shifted to average zero at the start of the measurement, following the methods of Refs. [8, 10, 28].

By comparing the phase to the normal force, it appears that the phase changes by <180º when the tip and substrate are not in intimate contact. However, the rate of change of the phase changes dramatically when the two touch. In other words, the phase response appears to depend on the interfacial stiffness, indicating that the IFM sensor / material interaction cannot be modeled as a simple harmonic oscillator. (The point of contact is confirmed also by comparing the phase (Figure 42b) to the amplitude of the lockin (Figure 42c).) We have obtained similar results using other tips and substrates (not shown) and determined that the total range of phase change from out-of-contact to a hard contact depends on the indentation depth, as well as the tuning of IFM controller. This indicates that the phase and amplitude output by the lockin amplifier contains information about both the material and sensor responses to the dither. Therefore, the two must deconvoluted to accurately measure viscoelastic properties of the sample material. In general, the phase shift depends on the mass, stiffness, and damping of each of the tip, substrate, intervening fluid (if present), sensor mechanical components, and sensor feedback electronics (in equivalent electrical terms) [105]. The damping coefficients can be frequency-dependant. Then, accurate viscosity measurement requires a many-parameter model. This is nontrivial because only one axis of motion (rotation) is measured by the current IFM electronics, while significant motion may exist along the other axes (see Section 5.2.5.5 Nonparallelism between Sample, Top-plate, and Sensor).

Another telling example is an observation that occurred during the measurements of the viscosity of the liquid-like-layer on ice [28]. In that study, the in-phase and out-of-phase components of the lateral force were coincident; that is, the phase was a constant 45º throughout the measurement [299, 302]. At present, no physical explanation has been found for this anomaly.

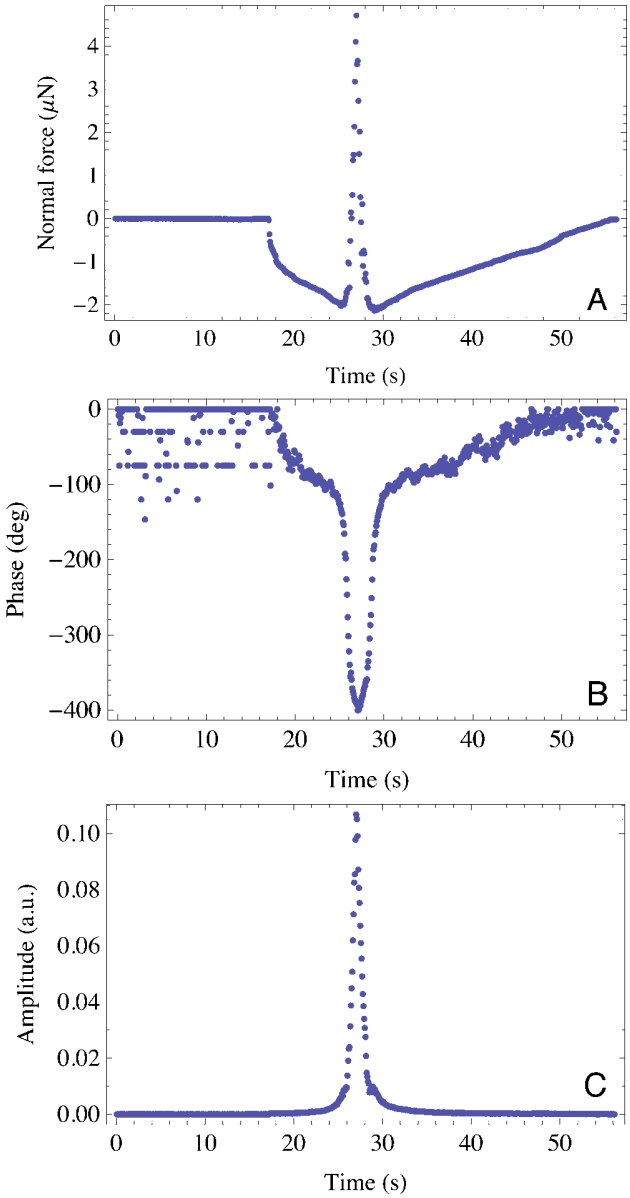


**Figure 42. Example IFM measurement during the approach of a diamond tip toward Si(111) in humid air while the tip was dithered laterally: (A) normal force on the tip; (B) phase lag between dither drive and sensor output after normalizing initial phase to zero and adjusting for phase inversions beyond the 360º range of the lockin to show the monotonic change in phase throughout the measurement; and (C) amplitude of the lockin amplifier (a.u.).**

### 5.3.2.2 Dynamic Response of IFM Sensor to Oscillatory Set-Point Changes

That the IFM sensor cannot be accurately modeled as a damped harmonic oscillator is illustrated as follows. The setpoint to the probe position was oscillated as a function of frequency for a sensor suspended in air, while the amplitude of the resultant top-plate oscillation (rotation

amplitude) was recorded. The frequency-response curve (Figure 43, left) shows a resonant peak ~80 Hz, but the form of the curve does not follow that of a damped harmonic oscillator, which flattens to zero gain beyond the resonance peak if the oscillator is mechanically overdamped, as is the IFM sensor [42]. This observation is expected because the feedback mechanism effectively extends the bandwidth of the sensor. However, this indicates that the sensor cannot be modeled as a damped harmonic oscillator. Neither does the model of Warren et al. [136] modified for the single-sided feedback control used in these measurements correctly reproduce the frequency-response curve (Figure 43, right). These data also show that the assumption made in prior interfacial water studies involving this method [8] that the dynamic response of the sensor is insensitive to the measurement frequency is not valid. In particular, the procedure of Ref. [10] to account for phase lag arising from the sensor response by subtracting the value measured before the tip nears the sample surface should only be valid if the phase lag is constant throughout the measurement. In general, this is not expected to be the case. Non-constant frequency in the frequency-response curve (Figure 43) implies non-constant phase in response to the tip's interaction with a sample. This should motivate accounting for the sensor's full electromechanical response to deconvolute the sensor and sample dynamic responses. Such a task is a considerable effort and is beyond the scope of this project.

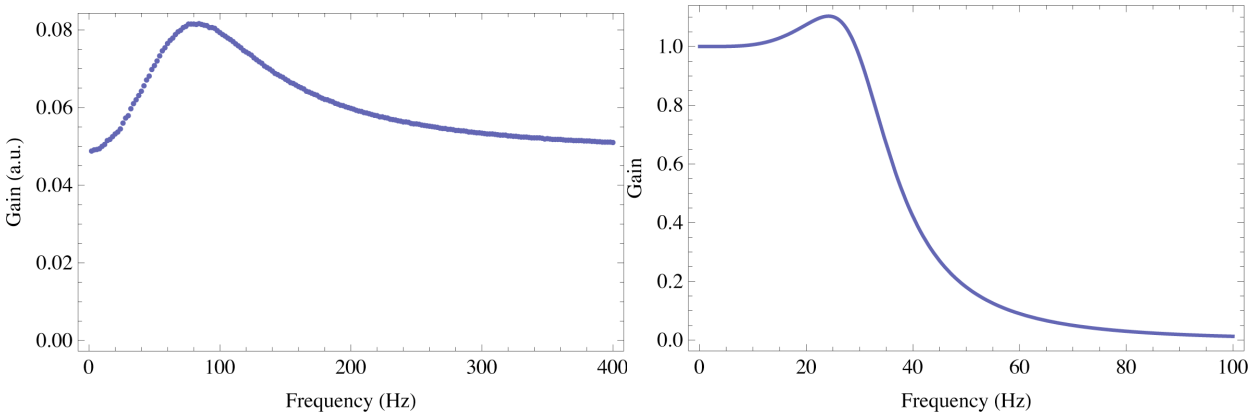


**Figure 43. Left: Measured frequency response of the IFM sensor rotation in response to an oscillatory change in set point. Right: prediction based on the model of Warren et al. [136] modified for single-sided actuation. Note the different horizontal scales between panels. Both vertical scales are in arbitrary units.**

### 5.3.2.3 Unintended Motion along the Normal Coordinate

The purpose of the IFM's force-feedback is to maintain the position of the probe at a prescribed location at all times. However, like all systems or processes operating under feedback, the control is inherently imperfect. It is now recognized that force feedback control is not well suited for nanoindentation instruments, such as IFM, because of the wide range of nonlinear stiffnesses (>5 orders) encountered by the probe as it starts from out-of-contact and contacts and indents a sample [105]. That is, a feedback loop that is tuned to minimize error in the probe position when the probe is far from the sample may have to be retuned to minimize error when the probe touches the sample. The IFM force sensor is typically tuned to achieve optimal force resolution in the region of probe-substrate separations where attractive forces can be measured. In such

cases, the IFM sensor is susceptible to noise, both ambient and that created by perturbing the probe. Laterally dithering the probe excites resonances in the IFM control response that are manifest as oscillations of the probe position both normal and lateral to the sample.

As an example, Figure 44 shows the interaction of a 250-μm glass IFM tip with a $BaF_2(111)$ surface in humid nitrogen. During the measurement, the sensor holding the probe was oscillated laterally at a frequency of ~90 Hz and an amplitude of ~1 nm. Figure 44(upper pane) shows the force in the normal direction as a function of the probe displacement, as well as the displacement of the probe in the normal direction relative to the prescribed position. The prescribed probe position was ramped in time to until a specified force of 45 μN on the tip was reached, then the probe was retracted at the same speed. The lower pane in Figure 44 shows that the error in the probe position was >8Å peak-to-peak when the probe was near the substrate. Importantly, this amplitude was several times the diameter of a water molecule. In this case, the properties of the fluid are not easily separated from that of the probe and sensor. The force signal has a significant noise associated with moving the probe. Such noise is generally not noticeable in earlier IFM works because of the heavy averaging done by the ProbeView IFM software used in prior works. Then, because no previous IFM studies have reported values for the error signal in the IFM controller, it is impossible to assess whether or not this effect was significant in previous studies of interfacial water. Further, because in the lateral dither method a lock-in amplifier is used to filter out all frequencies in the force signal except the one corresponding to the dither frequency (~90 Hz), this noise may not appear in the recorded lateral force. Because the IFM sensor is only sensitive to rotation, the exact trajectory of the probe during a dither within interfacial water is unknown; however, it is clear from these data that the probe cannot move purely tangentially to a surface, which may allow additional modes of energy dissipation that are not captured with the single-frequency lock-in method.

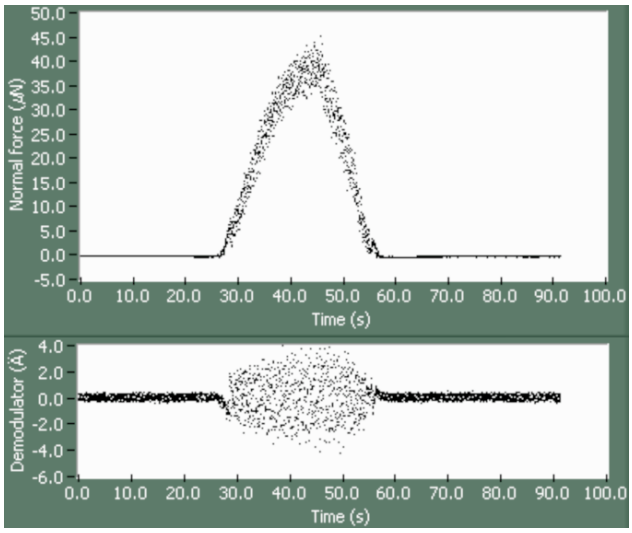


**Figure 44. Normal force (upper curve) and PID error (lower curve; viz., the demodulator signal calibrated in terms of the probe motion relative to its position setpoint) as a function of time as a glass IFM tip is moved toward a $BaF_2$(111) surface, then retracted after reaching ~45 μN of force in a humid nitrogen environment (<1% relative humidity). The tip was dithered laterally during the entire measurement (90 Hz, 1-nm amplitude) and approached and withdrew at a speed of 25 Å/s. Sensor tuning constants: K = 15 and I = 9.**

### 5.3.2.4 Squeeze-Film Air Damping

Unintended motion of the IFM sensor top-plate may give rise to energy dissipation internal to the IFM sensor because of squeeze-film air damping within the capacitor gap. This effect is anticipated to be much more significant when applying the lateral dither method of viscosity measurement than for a drainage experiment because of large differences in the top-plate rotational velocity along the torsion bar axis. This is shown by repeating the analysis of the section, 5.2.5.1 Squeeze-Film Air Damping, but with the following modifications. The rotation of the top-plate while a tip is dithered across a surface can be directly measured. For example, for the data in Figure 44, this rotation corresponded to an ~8Å peak-to-peak oscillation along the torsion bar rotational axis. Along with the frequency (typically ~100 Hz) and scaling by $2^{1/2}/2$ to estimate the rms velocity, this corresponds to an average rotational velocity of $d\theta/dt$ = 57 μrad/s, nearly an order of magnitude larger than the upper limit anticipated during a drainage experiment. Then, the oscillatory force at the tip point arising from squeeze-film air damping at the measurement frequency is anticipated to have an amplitude $\sim 2\tau/L$ = 4.3 μN.

The value of the force (~4.3 μN) is comparable to the friction values typically measured with IFM, being larger in some cases (e.g., Ref. [10]), as expected if the feedback mechanism were able to partially compensate for rotation of the sensor top-plate as intended. Nonetheless, this suggests that squeeze-film air damping may be a significant source of energy dissipation in measurements of friction using the dither method. The extent that this effect is significant should depend on the sensor tuning and the nature of the tip-sample interaction; therefore, we are unable to assess its significance during previous studies of interfacial water. However, even if the top-plate position were controlled to within ±1Å peak-to-peak, the damping force would be expected to be ~530 nN, which is still significant compared to friction force values reported earlier ([8, 10,

28]). That squeeze-film air damping affects the dynamic response of the IFM sensor has been noted elsewhere [136].

Also, Figure 44 indicates that the top-plate rotational amplitude is not constant throughout the measurement, therefore, neither should the force arising from air damping be constant. For this reason, neither will the phase shift introduced from air damping be constant. Accounting for these non-constant contributions to the amplitude and phase of the measured force is not easily accomplished empirically.

### *5.3.3 Sympathetic Response from Probe Misalignment*

Small amounts of tilt between the tip and the sample may create an artificial "friction" force when none should exist. This is because the lock-in method only measures the dot product of the force vector on the tip at the oscillation frequency. In such cases, the phase-sensitive detection may register a lateral force proportional to the gradient of the normal force ($F_N$) with respect to distance ($D$), scaled by the cosine of the misalignment angle ($\theta_{p\text{-}t}$). Typical values for the force gradient before intimate probe-substrate contact can be taken from the interfacial water study of Goertz, et al., (Fig. 1a), viz., $\partial F/\partial D \approx 530$ N/m, and $\theta_{p\text{-}t} \leq 5^{\circ}$. Then, the measured lateral force arising from sympathetic effects could a have maximum value of $a(\partial F/\partial D)\ \mathrm{Sin}(\theta_{p\text{-}t}) \approx 31$ nN. This value is comparable to the total lateral force reported by Goertz, et al. [10] when the probe was ~0.5 nm from the substrate. While their data do not show that the lateral force directly follows the gradient of the normal force, it should be recognized that the sensor under feedback is a nonlinear process element; therefore, this calculation only highlights plausibility. This effect is elastic; however, as with elastic deformation of sensor components in response to oscillatory excitation, it cannot be strictly discounted in modeling the entire nonlinear response of the IFM sensor.

### *5.3.4 Stiffness of Components in the Measurement Train*

Elastic deformation of sensor components may contribute to inaccuracy in the calculated viscosity values even though energy stored in elastic components is conserved because the IFM sensor operated under feedback cannot be modeled as a simple harmonic oscillator (see Section [x]). Consequently, quantitative interpretation of the phase and amplitude values recorded using the lock-in technique also requires knowledge of the stiffness of each compliant element. As discussed below, the torsion bars and probe shank appear to be the only significant sensor components that may need such consideration.

#### **5.3.4.1 Torsion Bars**

The effective stiffness of the torsion bars in the vertical or horizontal directions relative to the sensor normal can be estimated as $k = 250$ N/m per bar, or 500 N/m for the two bars in parallel [305]. Therefore, at a typical lateral force value of 100 nN relevant to the interfacial water experiments, the torsion bar deflection is expected to be ≤2Å along the surface normal, a significant fraction of the typical oscillation amplitude (7–10 Å). This value is an upper bound because, in general, the probe tip is not perfectly normal to the sample. As well, the current IFM sensor only detects rotation of the sensor top-plate along the torsion bar axis, and cannot detect horizontal or vertical movement of the top-plate [305], so that only estimates for the torsion bar

deflection can be made. The situation is further complicated by non-parallelism between the capacitor electrodes inherent in the sensor and tip assembly process, so that lateral compliance of the torsion bars can allow energy dissipation when the sensor is under feedback (see 5.2.5.5 Nonparallelism between Sample, Top-plate, and Sensor).

#### 5.3.4.2 Top-Plate

The effective stiffness of the top-plate can be estimated from simple beam-deflection theory as $k = Ewt^3/(4l^3)$, where $w$, $t$, and $l$ are the top-plate's width, thickness, and length, respectively [265]. One-sided deflection across the torsion bars (assumed fixed) with the tip mounted in the middle of the top-plate, $k$ = 150,000 N/m for the current sensor dimensions. Then, at an indentation force of 10 μN, the top-plate deflection is expected to be <0.1Å. Therefore, deflection of the top-plate is insignificant.

#### 5.3.4.3 Probe Shank

The effective stiffness ($k_{eff}$) of a macroscopic cylinder can be estimated from its Young's modulus ($E$), radius ($R_m$), and length ($L$) as $k_{eff} = 3\pi E R_m^4 / (4L^3)$ [314]. Assuming typical values for the shank of a W IFM probe ($R_m$ = 50 μm, $L$ = 4 mm, $E$ = 450 GPa) suggests $k_{eff}$ ~ 100 N/m for the probes used in the IFM experiments. The lateral force, $F_L$, measured in the IFM experiments of interfacial water (e.g. [10]) are ~40 nN when the probe is in the interfacial region. Under this force, the deflection of the probe shank is anticipated to be $F_L / k_{eff}$ ~4Å, or about 40% of the amplitude of the lateral oscillation. As the probe presses hard against the sample, $F_L$ can reach ~160 nN, so that the deflection of the probe shank is expected to be ~1.5 nm, or ~50% larger than the imposed oscillation. That is to say, at these large lateral forces, the bulk of the deflection can be expected to be taken up by the probe, rather than by interaction between the tip and sample. Both scenarios suggest that accounting for the probe deflection may be necessary for achieving an accurate value for the viscosity of the interfacial water.

#### 5.3.4.4 Probe and Substrate

While we are not aware of a formalism that could be used to easily predict the elastohydrodynamic deformation of the probe and substrate during the lateral dither method, we note that tip speeds in the IFM experiment are typically ~300 nm/s, more than an order of magnitude greater than in the drainage method (~10 nm/s). At the latter speeds, elastohydrodynamic considerations were predicted to be significant in the drainage method when the probe-substrate separation was less than ~1 nm (see 5.2.5.2 Elastohydrodynamic Considerations). Therefore, it will be important to establish if elastohydrodynamic deformation is significant for the lateral dither method.

### *5.3.5 Other Assessments*

#### 5.3.5.1 Method Sensitivity

The smallest viscosity that can be measured using the IFM lateral dither method can be estimated from Feibelman's expression for the friction force (Eq. 36 of Ref. [41]), solved for the viscosity (single-point method), viz.:

$$\eta = \Delta F_L / (2\pi v R \, \mathrm{Ln}(w/D)) \qquad (2)$$

For the typical experimental parameter values, $\Delta F_L$= 1 nN, $w$ = 1 nm, $D$ = 1Å, v = (1 nm)×(90 Hz), and $R$ = 5 μm, the smallest viscosity that can be measured using the IFM lateral dither method is ~150 Pas, or ~$10^5$× the viscosity of bulk water. Then, any viscosity inferred with this method will appear to have a very large viscosity compared to that of bulk water.

#### 5.3.5.2 Statistical Evaluation

One criticism with the IFM measurements of interfacial water viscosity concerns the lack of suitable statistics. For example, in Ref.[10], only one friction-versus-probe displacement curve was fit to Feibelman's model [41] to determine the interphase viscosity. While comparable viscosity values for interfacial water have been obtained with IFM using several methods, an evaluation of the precision of each technique is lacking. To address this issue, Figure 45 shows a superposition of ~100 measurements of interphase viscosity at various relative humidities using the dither method as described in Ref. [10, 111]. In the plot, both the friction force and probe penetration into the film are normalized according to Feibelman's model [41], and so give the expected linear relationship at small penetrations. However, we stress that correlation does not guarantee causation. Here, values for the fit thickness range over $0.8 \leq w \leq 2$ nm. A sensitivity analysis of the fitting procedure (in this case, nonlinear least-squares regression) applied to each fit revealed that the interphase thickness determined in this manner has an uncertainty that range ~30–50%, owing to uncertainties in determining the initial point of contact between the interphases that are assumed to cover both probe and substrate in this model. The fit viscosity is not sensitive to this uncertainty, and gave values comparable in each case ($\eta_0$ ~1 MPa.s, ~20% standard deviation) that did not vary with relative humidity.

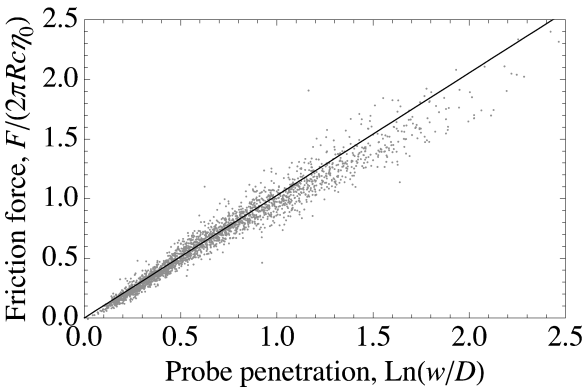


**Figure 45. Friction force determined using the lateral dither method with IFM [10] between a spherical Au-coated glass probe (200-nm radius) and hydroxylated Si(111)-oxide. Shown is a superposition of ~100 measurements at various relative humidities (2–60%). Each measurement was fit independently to the model of Feibelman [41] and normalized before superimposing the results. The friction force is normalized by the probe radius (*R*), probe lateral velocity (*c*), and the fit interphase viscosity ($\eta_0$). The probe penetration into the film is the probe displacement (D) normalized by the fit interphase thickness (*w*). The best fit line shows reasonable linearity in the normalized data for small film penetrations, as anticipated by Feibelman's model [10].**

#### 5.3.5.3 Triboelectrification

Triboelectrification of the probe-substrate interface is another possible origin of energy dissipation during single-asperity friction [315]. The significance of this effect can be expected to be materials specific, and has not yet been explored in IFM experiments.

#### 5.3.5.4 Selection of Dither Frequency

Among other noise sources, the IFM instrumentation contains a significant 120Hz noise component, as shown in Figure 46. However, noise is lowest over the range 90–110 Hz. From this standpoint, the convolution of the results from electrical line noise sources is not anticipated to be a significant source of error. That the oscillation frequency used in prior IFM experiments is near the resonant frequency of the IFM sensor under feedback is problematic for analysis, however (see section 5.3.2 Sensor Dynamical ).

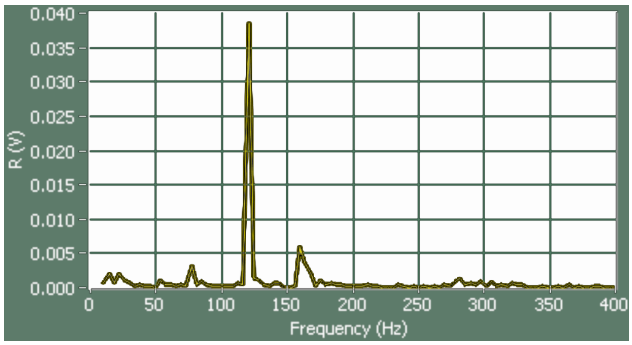


**Figure 46. Frequency response of a diamond IFM tip hovering on a Si(111)-oxide surface in humid air while maintaining a constant force level of 0.5 μN.**

#### 5.3.5.5 Lateral Shear of a Meniscus

IFM has also been used to estimate the viscosity of interfacial water inside a nanoscale meniscus of water condensed between a probe and surface placed within a few nanometers of each other in humid nitrogen [8]. It is important to recognize that what was actually measured in this experiment was a lateral force, which was then modeled to estimate a viscosity value. In principle, such a model should account for viscous dissipation from the entire meniscus, not just from the interfacial water. Such a model has not been developed to determine the significance of this effect, however.

#### 5.3.5.6 Rate of Approach

The lateral speed of the IFM probe tip is much faster than the tip's rate of approach toward the sample in the experiments in Refs.[10], but not for the experiments involving the liquid-like layer of ice [28].

#### 5.3.5.7 Newtonian Fluid

See Section 5.4.6 Newtonian vs. Non-Newtonian Fluid.

### *5.3.6 Summary*

Several key assumptions underlying the dither method for determining the viscosity of interfacial water have been discussed. Uncertainties in the dynamical characteristics of the sensor components (both mechanical and electrical) constitute the largest uncertainty in this method. Key is that the present IFM only detects and controls motion along one axis (rotation), while deflection along the other three most significant axes of motion (lateral and vertical deflection of the torsion bars and torsion of the sensing tip) are anticipated to be significant under typical force levels encountered during experiments involving interfacial water. While these deflections are expected to be "small" (angstroms), they are nonetheless a significant fraction of the interfacial water thickness. Further, mechanical "cross-talk" between the deformation modes of the sensor is anticipated to allow energy dissipation that cannot be measured with the present instrumental configuration. That the assumptions about the dynamical behavior of the sensor followed in prior work [8, 10] may not always be accurate is highlighted by examples of measured amplitude and phase of the IFM's force output that appear anomalous with respect to those assumptions. Fully

characterizing the dynamics of the IFM sensor constitutes a rigorous sensor characterization and modeling project that is beyond the scope of this LDRD project. An alternate experimental method that has already been well-characterized is discussed in section 5.5.2 Small-Amplitude Atomic Force Microscopy.

## 5.4 Common Aspects in IFM

A number of additional analyses relevant to both the drainage and dither methods used with IFM for measuring interfacial water viscosity are summarized below.

### *5.4.1 Validity of Continuum Description*

Tichy [118, 128, 130, 316, 317] and others argue that continuum hydrodynamics modeling can remain a valid tool at the nanometer scale when one is interested in ensemble averages of time scales much longer than the molecular relaxation time, so that the transport of even a small number of molecules can be described using continuum theories. It is well-known that confined water can exhibit reduced mobility and antisymmetric transport properties [27]; however, precise guidelines for assessing the validity of continuum mechanics at the length scale of interfacial water (~1 nm) have yet to be developed.

### *5.4.2 Molecular Shape of Probe and Substrate*

When modeling the interaction of a probe with a surface, e.g., to estimate interfacial viscosity, it is customary to model the probe as a sphere or parabaloid [265]. However, crystalline tips cannot be perfectly round. For W and Au probes (lattice parameter ~3 and ~4Å, respectively) coated with water interphases totaling 1-nm thick and of macroscopic radius of ~1 μm, the effective lateral radius of the probe-substrate contact is ~170 nm. Then, ~3 atomic layers of the probe are expected to interact within the interphases if the probes are crystalline and uniform. The majority of the probe-sample force arises from the portion of the probe deepest within the sample, that is, the outermost atomic monolayer of atoms on the probe surface. At this scale, it could be that the probe is better described as a flat surface. Li et al. [45] determined this uncertainty to cause <20% uncertainty in the inferred viscosity in the context of their measurements, by comparing model results based on sphere-flat and plane-parallel geometries of equivalent area. Though, the crystallographic orientation of the probe is not controlled with respect to the substrate and, in the case of the IFM dithering experiments, with respect to the probe sliding direction. Uncertainty in the viscosity values for this more complicated situation has not been evaluated; however, the present authors intuit on this basis of the result of Li, et al., that this is less than an order-of-magnitude effect on the inferred viscosity.

Neither probe nor substrate surfaces may be either perfectly spherical or perfectly flat, however. Tungsten, which was used for tips in the IFM experiments reported in Ref.[10], is known to readily oxidize in air and may pit when treated with strong acid. Only more recently has a procedure been developed to prepare tungsten IFM tips of micron radius with <1nm rms roughness [318]. The characterization of Au probes used in earlier IFM experiments [8] was not reported. IFM probes are not generally believed to wear as much as AFM tips used for imaging, for which even relatively hard silicon nitride tips are known to wear significantly over typical

durations of use [24, 265]. Kunert, et al. [319] recently used lattice Boltzmann simulations to show that during fluid drainage between a spherical probe and a randomly rough surface, the effect of the roughness was to shift the no-slip plane (boundary) of the rough surface to a position between the lowest and farthest extending point. Their conclusion relies on the assumptions that the fluid viscosity is equal to that of the bulk and that there is no hydrodynamic slip. Similar results have been found for macroscopic Poiseuille flow; viz., roughness can be accounted for as a change in the hydrodynamic perimeter of the conduit [320].

### *5.4.3 Salt Concentration*

The concentration of various salts in the aqueous phase and the confining surfaces has been shown to influence the propensity for water structuring between hydrophilic surfaces in some cases (e.g., [321, 322]). Therefore, it may be useful to control the concentration of salt or organic contaminants. Surfaces prepared in air can be assumed to adsorb atmospheric hydrocarbons and/or to undergo reactions with atmospheric species that may change the chemical nature and/or the charge state on the surface, thereby influencing any nearby fluid structure that may exist [222]. The chemical nature of the tip materials used in previous IFM studies of interfacial water had not been independently characterized. For example, Tungsten (used for IFM tips) is known to readily oxidize, but the extent of oxidation cannot be easily controlled or monitored at present.

### *5.4.4 Spatial Variation of Viscosity within the Confined Volume*

All determinations of interfacial water viscosity have pivoted on a particular solution to the Reynolds lubrication equation. Solutions differ primarily based on assumptions about: 1) the extent of hydrodynamic slip (or lack thereof) at the solid-fluid interfaces (see 5.4.5 No-Slip Boundary Condition), and 2) the viscosity variation (or lack thereof) with respect to either the solid-fluid interfaces or the local confinement. These two assumptions have only been evaluated independently using MD simulations [142].

In interpreting IFM experiments involving interfacial water, is has been assumed that water has a high viscosity within an interphase closest to the confining surfaces, and a bulk value elsewhere [8, 10, 28]. Feibelman developed solutions to the Reynolds equation relevant to the latter situation [41, 131], as well as for the drainage problem when the viscosity decreases linearly away from the surfaces [41]. In contrast, the overwhelming majority of studies aiming to measure the viscosity of interfacial water using other techniques have assumed that the viscosity of the fluid between the probe tip and substrate is constant (e.g., [45, 123, 125, 126]). With this assumption, what is measured is an “effective viscosity” that is a geometrically averaged value corresponding to the volume of fluid between tip and substrate [135]. This assumption greatly simplifies the mathematics required to solve the Reynolds lubrication equation to describe the fluid movement of interest (drainage or sliding lubrication), and to arrive at an analytical expression from which the force-versus-separation data can be modeled and an effective viscosity extracted. This assumption is also motivated by studies showing elevated shear resistance in nanoconfined fluids that are inferred to pack into liquid crystals [323]. In that view, the fluid viscosity is assumed to depend on the extent of local confinement, arising from the non-uniform pressure distribution between the surfaces.

Other motivations for validating these assumptions are listed below:

- The structure of water at an interface is known for relatively few materials [4], and may differ for probes and substrates made of different materials, as in the IFM experiments, because of epitaxial mismatch (or roughness) or chemical bonding [13].

- Fluid viscosity is known to sometimes increase when the local confinement approaches molecular dimensions, with some engineering fluids following the scaling relationship: $\eta / \eta_0 = (1+k_0/h)^8$, where $k_0$ is the molecular diameter and $h$ is the local surface separation [315]. If this scaling relation were valid for water, this would suggest that for $k_0 \sim h$, $\eta / \eta_0 = 256$, or a two-order of magnitude increase in viscosity from confinement effects alone. This value is only slightly higher than recent findings from molecular dynamics simulations [27, 115].

- Fluid viscosity is widely known to depend on pressure. For some lubricants, including water, this takes the form $\eta / \eta_0 = e^{mp}$, where $p$ is the local pressure and $m$ has a typical value of $2\ 10^{-9}\ Pa^{-1}$ [315]. In the drainage method, the average pressure on the probe and the pressure on the probe apex are of the order ~1 and 100 GPa, respectively [324, 325], corresponding to viscosities $10^{86}$ and 7 times the bulk values, respectively—assuming that this scaling relationship is valid over this range of pressures, which is by no means certain. Nonetheless, this suggests that the effect may be significant.

- In general, spheres sliding along a wall within fluid are deformed somewhat, leading to variations in local pressure and hence variation in local viscosity (see 5.2.5.2 Elastohydrodynamic Considerations) [315].

Further, the true spatial variation (or lack thereof) of water viscosity away from the solid-liquid interface cannot be easily measured between curves surfaces without data of exceptionally high fidelity [135]. Nonetheless, a crude sensitivity analysis of the data in Ref.[28] to the functional form for the viscosity distribution has been performed and suggests that this assumption produces uncertainty in the viscosity value by at most ~3 orders of magnitude when using the lateral dither method.

### *5.4.5 No-Slip Boundary Condition*

In modeling the IFM experiments, one must assume a boundary condition for the velocity of fluid at each solid-fluid interface. The models of Feibelman [41, 131] assume that the fluid velocity is zero at the water-solid interface, which is the well-known “no-slip” boundary condition [326]. However, several experimentalists have reported that their measurements of hydrodynamic forces with probes near surfaces can only be well-described by assuming a finite ”slip-length”, that is, the distance beyond the interface that the fluid velocity extrapolates to zero (e.g., [327]). Based on the formulation of Vinogradova, et al. [328], one can estimate that ignoring the possibility of hydrodynamic slip may overestimate the viscosity of interfacial water by a factor of <7 for slip lengths < 40 nm. MD simulations also report a finite slip length for water entrapped between hydroxylated diamond-like carbon surfaces [142].

### *5.4.6 Newtonian vs. Non-Newtonian Fluid*

Several authors have suggested that nanoconfined fluids, including water, may be non-Newtonian, that is, their viscosity may be shear-rate dependant. Lorenz, et al., used computer simulations to indicate shear-thinning of water confined between carboxylated SAMs [27]. Li and Riedo measured the loss and storage moduli of nanoconfined water using AFM and inferred a mild shear thinning behavior over a less than one decade change in shear rate [123]. Zhu and Granick [124] sheared water between mica sheets with SFA and observed a similar trend for the loss modulus over three decades of shear rate. The measurements of the shear response of confined fluids represented in Table 1 collectively span a frequency range of ~1–$10^4$ Hz.

### *5.4.7 Contact Size*

That simple organic fluids can be squeezed between mica sheets to form a liquid crystal at room temperature suggests that this structuring may have colligative attributes [91]. In this light, it is important to recognize that the measurements reported in Table 1 collectively span a broad range of length scales. Probe or probe-like geometries with radii spanning from ~10 nm to 1 cm were used in the studies listed in Table 1.

## 5.5 Alternative Experimental Methods

In this section, we comment on the plausibility of alternate experimental methods of measuring the viscosity of interfacial water.

### *5.5.1 Tapping-Mode IFM*

One possible approach to improving sensitivity in the viscosity measurement involves oscillating the IFM probe along the normal coordinate of the surface as it proceeds through an interfacial water film, and measuring the out-of-phase component of the oscillatory force using a lock-in amplifier. Figure 47 shows an analagous result where the in-phase force component was recorded to measure the stiffness of an interface. The method is as simple to implement as the lateral dither method, and qualitatively reproduces the same overall trend as simply derivitizing a force-distance profile. However, many important features of the stiffness curve are not represented. As with the drainage method, lag in the response of the IFM sensor while under load, which has a timescale much larger than the $1/f$ timescale of the oscillation, cannot be eliminated with this method. Therefore, this method will require further development of suitable models for interpreting the results. The chief advantages of this method over the lateral dither method is increased sensitivity and fewer uncontrolled modes of energy dissipation.

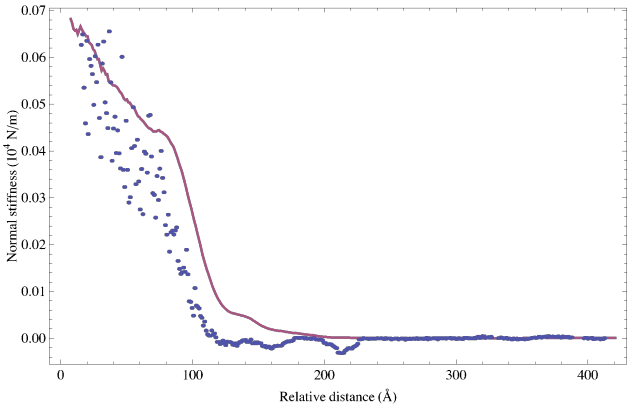


**Figure 47. Interfacial stiffness measured between a diamond IFM tip and a Si(111) surface in humid air as a function of the nominal surface separation. Dots indicate the numerical derivative of the force-distance curve measured using the conventional IFM method. The connected line is the stiffness (a.u.) measured using tapping mode IFM.**

### *5.5.2 Small-Amplitude Atomic Force Microscopy*

Implicit measurements of the structure of interfacial water using AFM have been pursued by Jarvis et al. [329] using nanotube probes and a large amplitude AFM technique, by Antognozzi et al. [125] using an AFM in shear force mode, by Cleveland et al. [89], who measured the oscillatory potential of the confined water layers indirectly by analyzing the Brownian noise spectrum of a AFM tip immersed in water, by Jeffrey, et al. [138], who used an off-resonance tapping mode AFM, and Maali, et al. [140], who use a near-resonance method. While the latter has so-far proven the most sensitive method, O'Shea [330] noted that the fluid viscosity cannot be determined independently of the fluid stiffness using Maali's analytical method. A constitutive model that fully deconvolves the full mechanical responses of the cantilever, elastic tip, elastic substrate, and fluid has not yet been developed.

### *5.5.3 Time-Resolved Evanescent Wave-Induced Fluorescence Anisotropy*

This method uses the time-dependant decay of bipolarized emission light from fluorescent dye molecules responding to evanescent waves propagating along an interface [331]. The method can be used to probe the local viscosity around the dye molecules, and therefore can be used to probe viscosity over nanometer length scales. The interfacial sensitivity of this technique is limited by the decay length of the evanescent wave into the medium away from the interface, which has the minimum value $L = \lambda/(4\pi n_1)$, where $\lambda$ is the wavelength of the fluorescent emitter and $n_1$ is the refractive index of the substrate supporting the interfacial water. The value $\lambda$ can be as small as 325 nm for hydroxycoumarin emitters, while $n_1$ can be enhanced to ~10 using a Pt or Au overcoat. Then, the method will probe viscosity over a length scale of ~26Å, roughly ten times the size of a water molecule. Therefore, this technique is unsuitable for probing interfacial water only ~1-nm thick.

### *5.5.4 NMR*

A method for probing dynamics of fluids is to use pulse field gradient (PFG) H-NMR, where magnetic gradients are used to label the position of spins and to measure their diffusion. The

limitation is illustrated by estimating the length scale that can examined be examined, $l = \sqrt{D\Delta}$ where D is the diffusion rate and $\Delta$ is an experimental observation time, typically ~1 ns. For bulk water, D~ 2.3 x$10^{-9}$ $m^2$/s at room temperature, such that experimentally one examines a surface dimension ~1.5 μm, much larger than the thickness of interfacial water. Therefore, this method does not appear well-suited for measuring the diffusivities of interfacial water. Another limitation is that the molecular relaxations of water in nanoconfinement may not be symmetric, which complicates the analysis of such an experiment. In particular, the Stokes-Einstein relation may not be valid at lengthscales of one or two nanometers near surfaces. Despite these limitations, Tovbina, et al., [332] used H-NMR in this manner to estimate that the viscosity of water confined within silica gel pores may be as large as 9.6 times that of bulk water.

### *5.5.5 High-Frequency Mechanical Resonators*

Two devices for measuring the dampening of fluids near surfaces include the Quartz Crystal Microbalance (QCM) and Surface Acoustic Wave (SAW) devices (e.g., Refs.[333-336]). The former can typically be oscillated at frequencies of ~5–10 MHz, while the latter can achieve resonances >300 MHz. Consequently, the latter is more sensitive to the surface condition, such as the presence of a film of higher viscosity than the surrounding bulk fluid. Use of either method to extract interphase viscosity requires carefully determined parameters for the QCM or SAW sensor electromechanical response, interface roughness, fluid slip-length, surface concentration of ionic impurities, and bulk fluid viscosity. Assuming typical values for each of these parameters, as well as for the viscosity of the interfacial water, QCM is anticipated to measure the response of the fluid >30-nm into the fluid bulk, and therefore would not be adequately sensitive to the surface condition (Personal communication, Q-Sense Corporation, March 2009). SAW devices may be adequately sensitive, but are limited in the geometries that can be investigated. As well, it is nontrivial to relate the damping coefficients inferred from modeling the SAW output to the interfacial water viscosity. However, if such an effort were successful, it would allow the viscosity of interfacial water to be examined in the absence of confinement, providing a useful comparison to probe-based methods where confinement of fluid between a probe and surface is inherent to the measurement.

### *5.5.6 Pressurized Infiltration of Porous Media*

The pressure drop across a porous media subjected to differential pressure on opposite sides of the media as a way to estimate the viscosity of the fluid moving through a media (e.g.[337]). However, this approach is not viable for measuring the viscosity of near-surface water because of the difficult of producing porous media with pore sizes less than a few nanometers. Consequently, the bulk of the pressure drop results from the transport properties of water molecules near the center of the pore. As well, the extraction of an interphase viscosity requires an accurate model for the pore topology; however, only the average pore size is easily obtained. Some comparison studies are possible. For example, Bowen et al. [337] showed that various salt solutions had up to 1.7 times the viscosity of purified water in the same polysulfone membranes.

### *5.5.7 Fluid flow through Carbon Nanotubes*

The rate of flow of water through a carbon nanotube can be measured explicitly, and potentially related to the structure of water within the tube; relating these results to the water-solid structure and generalizing the results to other interfaces is not trivial, however [338].

### *5.5.8 Mechanical Relaxation*

It has been suggested that one could measure the relaxation of interfacial water, that is, the evolution of stress in response following an imposed strain, to ascertain its viscoelastic properties, along the lines of the IFM experiment in Ref. [303] involving a viscoelastic polymer. This is not possible with the present IFM configuration because of thermal drift that typically causes the sample interface to expand at a rate exceeding several angstroms per second. As well, this drift rate is comparable to that which arises from charge infiltration and/or thermal expansion of the piezo transducer that is actuated to move the IFM probe. Deconvoluting these effects significantly complicates the interpretation of the data, and may not be practical. MD simulations suggest a shear-thinning behavior for interfacial water at shear rates much higher than can presently be achieved with IFM [127]. Therefore, to examine the regime of lower shear rates, a well-characterized oscillatory or sliding method may prove sufficient (see below).

### *5.5.9 Slow, Lateral Sliding with a Scanning Probe*

Some of the difficulties of relating the lateral force on a probe tip as it slides through interfacial water to the true frictional force and the interfacial viscosity can be ameliorated by reducing the sliding frequency to one far below the resonant frequency of the IFM sensor under feedback. This is not possible with the 1$^{st}$-generation IFM, because it cannot measure normal and lateral forces independently at the low frequencies that this method would require. However, this capability exists in the 2$^{nd}$-generation IFM [311]. This will require higher displacement stability (and hence lower force resolution) of the IFM probe tip than the data in Ref.[312] suggest presently exists.

## 5.6 Conclusions

We have evaluated the drainage and lateral dither methods that have been used with IFM to measure the viscosity of water confined within an intersurface gap of 1–2 nanometers. We have found that the present IFM at Sandia is not well-suited to this particular task. The reasons for this are listed in Table 8 and summarized below. Further, not accounting for these facets of the measurement may lead to overestimation of the interphase viscosity or thickness in some cases.

The dominating limitation of the present IFM instrument is the inability to completely eliminate lag in the force-feedback response completely and to *simultaneously* control the tip displacement to better than ~1 nm. Lag can only be completely eliminated using relatively high values for the gains of the feedback controller to ensure a fast response time. However, this creates resonance in the feedback loop that is manifest as tip oscillations with amplitudes that typically range ~0.5–2 nm rms, depending on the specific tuning, the tip radius, and other factors. This oscillation is larger than the thickness of interfacial water. In turn, energy may be dissipated through the

interfacial film from these oscillations, the tip may intermittently contact the underlying surface, and the native near-surface structure of the film may be heavily influenced by the measurement itself. While not insurmountable, these aspects present difficulty in interpreting the experiments, particularly in relating the measured apparent viscosity to molecular properties of the surfaces or fluid.

Conversely, setting the feedback controller to relatively low gain values reduces the oscillations to amplitudes as small as 0.2Å rms but introduces significant lag (up to 200 msec.) in the feedback response, allowing for low-frequency energy dissipation through the sensor's own damping characteristics. A feedback tuning that forms a compromise between these two situations may exist in some cases; however, care must still be taken to validate the results by, for example, fully developing one of the approaches outlined in Section 5.2.2.2. Not enough information is available to evaluate the validity of the prior IFM measurements of interphase viscosity [8-10, 28, 300] on this basis, however.

The dynamic response of the IFM sensor is only expected to complicate the interpretation of results when the sample thickness is of the order of ~1–2 nm (e.g., interfacial water) *and* the properties of interest are dynamic (e.g., viscosity). These limitations are not problematic for nanometric thin films when the properties of interest are quasi-static (e.g., equilibrium force-distance curves, adhesion, yield stress, etc.). Conversely, dynamic properties can be measured without complication for films much thicker than 1 nm (e.g, Silly Putty™) and of high enough stiffness, e.g., using the relaxation method described in Refs.[303, 339]. Also, qualitative comparisons between dynamic properties of interfacial water, such hydrodynamic slip or viscosity change, can be made using IFM [10]; however, quantitative interpretation is subject to the limitations summarized in Table 8.

Finally, the complexities of both the experiments and their interpretation can be circumvented using small-amplitude AFM [340]. With this method, the tip oscillations are much smaller than the diameter of a water molecule and an analytical framework already exists to fully deconvolute the dynamical responses of the cantilever and the fluid. Besides, the force resolution is superior to IFM, allowing for smaller tips, superior imaging, mapping of rheological properties and correlation to topography, the examination of a greater variety of surfaces, and the use of commercially available tips.

Strategies for overcoming the dynamic limitations of the IFM sensor include:

1. Performing experiments with small-amplitude AFM [340].

2. Developing a unified model for the dynamical response of the entire train of electromechanical and sample components in the existing IFM to allow the sensor and material responses to be mathmatically deconvoluted.

3. Replacing the electronic feedback control with feedforward control, thereby effectively increasing the bandwidth of the IFM sensor [105].

4. Redesigning the IFM sensor to allow larger electromechanical bandwidth.

**Table 8. Potential pitfalls in measuring interphase viscosity with IFM.**

| Cause | Effect | Report Section(s) |
|---|---|---|
| Sensor response time is comparable to measurement time (if using "low" feedback gains) | Lag in feedback response.<br>Apparent energy dissipation in measurement is a convolution of sensor and sample damping mechanisms.<br>Viscosity may be overestimated. | 5.2.2.1<br>5.3.2.2 |
| Jitter in tip position is larger than the thickness of interfacial water (if using "high" feedback gains) | Energy dissipation and sample perturbation through motion of the tip along the normal coordinate.<br>Native "structure" of interfacial water may be altered by the tip oscillations.<br>Tip intermittently touches the substrate while contacting the fluid interphase. | 5.2.2.1 |
| Unmonitored mechanical degrees of freedom in the sensor | Energy dissipation and sample perturbation through unmonitored axes of motion of the tip. | 5.2.2.1<br>5.3.2.3 |
| Force-sensitivity limits IFM to large-radius tips | Elastohydrodynamic flattening can lead to overestimation of the thickness of the viscous interphase.<br>Insufficient imaging resolution to target areas on a sample or to study small-grained materials (e.g., kaolinite). | 5.2.5.2 |
| Finite error in alignment of the tip to the sample and in assembling sensor components | Energy dissipation through tip-substrate friction and squeeze-film air damping of sensor.<br>Sympathetic frictional response to the force gradient. | 5.2.5.5<br>5.3.3<br>5.3.5.3 |
| Lack of multi-axis force sensing | Cannot detect off-axis tip motion or energy dissipation mechanisms (e.g., from misalignment or sample interactions). | 5.2.5.5 |
| Inadequate force sensitivity to measure the viscosity of bulk water | Cannot measure transition from fluid to near-surface rheological properties.<br>Lack of a built-in viscosity calibration. (Other fluids, such as glycerol, can be used for calibration, however.) | 5.2.4<br>5.3.5.1 |
| Complexity of electromechanical train | Involved process to develop a unified model for the full sensor dynamics (16 parameters for IFM sensor, plus material parameters) | 5.2.2.2.1 |
| Limited bandwidth of sensor | Rheological properties can only be measured over ~2 orders of frequency, which is small compared to typical rheometric methods. | 5.2.2.2.1 |
| Lack of environmental control and tools for *in situ* characterization of surface chemistry | Difficult to relate rheological properties to surface chemistry and hence to molecular / atomistic interpretations. | 5.4.3 |

## 5.7 Acknowledgements

We thank Matthew Goertz for carefully reviewing this section and for many helpful discussions, as well as: Todd Alam, Darren Branch, Richard Cernosek, Randy Cygan, Greg Hebner, Jim Martin, Stephen Martin, Randy Schunk, and Brian Swartzentruber (preceding at Sandia National Laboratories), Steven Hussey (Q-Sense Corporation), Jacquelin Krim (North Carolina State University), and Kristianto Tjiptowidjojo (University of New Mexico).

# 6. CONCLUSIONS

We have made fundamental progress in understanding the structure and transport properties of water near surfaces and confined between hydrophilic surfaces at the nanometer scale. Our computations show that water in nanoconfinement can have reduced mobility that can be manifest as an increase in its apparent viscosity in some cases. Both water-water and water-solid molecular interactions give rise to unique temporal ordering of water that, for the material systems we have studied, differs from that of the liquid bulk and of the structure of ice-1h, both at cryogenic and room temperatures for various surfaces. How this balance of interactions gives rise to the boundary conditions that determine fluid flow in nanopores has yet to be resolved in a general sense yet remains important for a myriad of areas of science and technology.

In attempting to answer this question, several experimental discoveries have also been made. One was the discovery that superplastic nanowires could be pulled from the surface of common salt (NaCl)—the first demonstration of superplasticity in an ionic crystal at the nanoscale. Also, by improving the sensitivity of Sandia's Interfacial Force Microscope (IFM) by 15×, we have made detailed observations of nanoscale wetting and adhesion forces, and identified limitations of current adhesion theories relevant to resolving stiction in MEMS/NEMS. Other related experimental and theoretical accomplishments are summarized in Section 1.2.

Finally, we have evaluated the methods involving IFM used previously to measure a viscosity for interfacial water one-million times that of the bulk value. In particular, we have identified several potential pitfalls in the IFM methods that, while not insurmountable, motivate the use of newer techniques, such as small-amplitude AFM [340], that resolve these difficulties and thus present a more rapid and certifiable experimental approach to answering fundamental questions about the fluidity and structure of interfacial water. (See Section 5.6 for a summary of these findings.) The evaluation has also identified ways to improve the operation and design of IFM relevant to this and other Sandia research.

# 7. REFERENCES


1. Canter, N., *Stretching salt.* Tribology and Lubrication Technology Magazine, 2010(January): p. 10-11.
2. Cygan, R.T., et al., *A molecular basis for advanced materials in water treatment.* MRS Bulletin, 2008. **33**: p. 42-47.
3. Peschel, G. and K.H. Adlfinger, *Viscosity Anomalies in Liquid Surface Zones: IV. The Apparent Viscosity of Water in Thin Layers Adjacent to Hydroxylated Fused Silica Surfaces.* Journal of Colloid and Interface Science, 1970. **34**(4): p. 505-510.
4. Henderson, M.A., *The interaction of water with solid surfaces: fundamental aspects revisited.* Surface Science Reports, 2002. **46**(1-8): p. 5-308.
5. Cygan, R.T. and J.A. Greathouse, *Frontiers of Interfacial Water Research: Workshop Report*. 2005, Sandia National Laboratories: Albuquerque, NM.
6. Pollack, G.H., *Gels and the Engines of Life, A New Unifying Approach to Cell Function*. 2001, Seattle: Ebner and Sons. 319.
7. Cameron, I.L., *Commentary (and book review) Pollack's Gel Phase Transition Paradigm of Cell Function.* Cell Biology International, 2002. **26**(4): p. 309-312.
8. Major, R.C., et al., *Viscous water meniscus under nanoconfinement.* Physical Review Letters, 2006. **96**(17): p. 177803-1 -- 177803-4.
9. Kim, H.I., et al., *Viscous "interphase" water adjacent to oligo(ethylene glycol)-terminated monolayers.* Langmuir, 2003. **19**(22): p. 9271-9275.
10. Goertz, M.P., J.E. Houston, and X.Y. Zhu, *Hydrophilicity and the viscosity of interfacial water.* Langmuir, 2007. **23**(10): p. 5491-5497.
11. Brovchenko, I. and A. Oleinikova, *Interfacial and confined water*. 2008, Amsterdam ; Oxford: Elsevier. x, 305 p.
12. Bhushan, B., *Micro/Nanotribology of MEMS/NEMS Mateirals and Devices*, in *Nanotribology and Nanomechanics; An Introduction*, B. Bhushan, Editor. 2005, Springer-Verlag: Berlin. p. 1031-1089.
13. Feibelman, P.J., *The first wetting layer on a solid.* Physics Today, 2010. **63**(2): p. 34-39.
14. Moore, N.W., et al., *Superplastic Nanowires Pulled from the Surface of Common Salt.* Nano Letters, 2009. **9**(6): p. 2295-2299.
15. Chang, K., *The Silly Putty Properties of Table Salt*, in *The New York Times*. 2009: New York. p. D3.
16. Flatow, I., *Science Fridays*, in *National Public Radio Broadcast*. 2009.
17. Ceurstemont, S., *Salt Crystals Reveal Surprise Stretchiness.* New Scientist, 2009(June 2009).
18. Broadwith, P., *Salt nanowire surprise*, in *Chemistry World News*. 2009, Royal Society of Chemistry.
19. Ehrenberg, R., *Salt Stretches in Nanoworld.* Science News, 2009. **176**(3): p. 14.
20. (2009) *Brittle table salt can stretch like taffy in the nanoworld*. ACS News.
21. King, A.G., *Research Advances: Elastic Salt, and Plant Progesterone.* Journal of Chemical Education, 2010. **87**(7): p. 660-661.
22. Feibelman, P.J., *Surface Water: Pentagonal ice in chains.* Nature Materials, 2009. **8**: p. 372-3.
23. Feibelman, P.J., *Water - From Interfaces to Bulk* Faraday Discussions, 2009. **141**(467): p. 467-475.

24. Goertz, M.P. and N.W. Moore, *Mechanics of Soft Interfaces Studied with Displacement-Controlled Scanning Probe Microscopy.* Progress in Surface Science, 2010. **In press**.
25. Lorenz, C.D., M. Chandross, and G.S. Grest, *Large Scale Molecular Dynamics Simulations of Vapor Phase Lubrication for MEMS.* Journal of Adhesion Science and Technology, 2010. **In press.**
26. Moore, N.W., *Contact Electrification through Dewetting of a Nanoscale Meniscus between Oxide Surfaces.* In preparation.
27. Lorenz, C.D., et al., *Molecular Dynamics Simulations of Water Confined between Matched Pairs of Hydrophobic and Hydrophilic Self-Assembled Monolayers* Langmuir, 2009. **25**(8): p. 4535-4542.
28. Goertz, M.P., X.Y. Zhu, and J.E. Houston, *Exploring the Liquid-like Layer on the Ice Surface.* Langmuir, 2009. **25**(12): p. 6905-6908.
29. Moore, N.W. and J.E. Houston, *The Pull-Off Force and the Work of Adhesion: New Challenges at the Nanoscale.* Journal of Adhesion Science and Technology, 2009. **In press.**
30. Degennes, P.G., *WETTING - STATICS AND DYNAMICS.* Reviews of Modern Physics, 1985. **57**(3): p. 827-863.
31. Kimmel, G.A., et al., *Crystalline ice growth on Pt(111): Observation of a hydrophobic water monolayer.* Physical Review Letters, 2005. **95**(16): p. 4.
32. Thurmer, K. and N.C. Bartelt, *Nucleation-limited dewetting of ice films on pt(111).* Physical Review Letters, 2008. **100**(18): p. 4.
33. Hu, X.L. and A. Michaelides, *Ice formation on kaolinite: Lattice match or amphoterism?* Surface Science, 2007. **601**(23): p. 5378-5381.
34. Thiel, P.A. and T.E. Madey, *THE INTERACTION OF WATER WITH SOLID-SURFACES - FUNDAMENTAL-ASPECTS.* Surface Science Reports, 1987. **7**(6-8): p. 211-385.
35. Feibelman, P.J., *Partial dissociation of water on Ru(0001).* Science, 2002. **295**(5552): p. 99-102.
36. Clay, C., S. Haq, and A. Hodgson, *Intact and dissociative adsorption of water on Ru(0001).* Chemical Physics Letters, 2004. **388**(1-3): p. 89-93.
37. Cerda, J., et al., *Novel water overlayer growth on Pd(111) characterized with scanning tunneling microscopy and density functional theory.* Physical Review Letters, 2004. **93**(11).
38. Carrasco, J., et al., *A one-dimensional ice structure built from pentagons.* Nature Materials, 2009. **8**(5): p. 427-431.
39. Miller, J., *Ice chains on copper are built from pentagons.* Physics Today, 2009. **62**(5): p. 17.
40. Vonnegut, B., *The nucleation of Ice Formation by Silver Iodide.* Journal of Applied Physics, 1947. **18**(7): p. 593-595.
41. Feibelman, P.J., *Effect of high-viscosity interphases on drainage between hydrophilic surfaces.* Langmuir, 2004. **20**(4): p. 1239-1244.
42. Joyce, S.A. and J.E. Houston, *A New Force Sensor Incorporating Force-Feedback Control for Interfacial Force Microscopy.* Review of Scientific Instruments, 1991. **62**(3): p. 710-715.
43. Raviv, U., et al., *Fluidity of water confined down to subnanometer films.* Langmuir, 2004. **20**(13): p. 5322-5332.

44. Fenter, P. and N.C. Sturchio, *Mineral-water interfacial structures revealed by synchrotron X-ray scattering.* Progress in Surface Science, 2004. **77**(5-8): p. 171-258.
45. Li, T.D., et al., *Structured and viscous water in subnanometer gaps.* Physical Review B, 2007. **75**(11): p. 115415.
46. Kumacheva, E. and J. Klein, *Simple liquids confined to molecularly thin layers. II. Shear and frictional behavior of solidified films.* Journal of Chemical Physics, 1998. **108**(16): p. 7010-7022.
47. Yamada, Y., et al., *Anisotropic water chain growth on Cu(110) observed with scanning tunneling microscopy* Physical Review Letters, 2006. **96**(3).
48. Duke, C.B., *Interaction of Electrons and Positrons with Solids - From Bulk to Surface in 30 Years.* Surface Science, 1994. **299**(1-3): p. 24-33.
49. Watson, P.R., M.A. van Hove, and K. Hermann, *Atlas of Surface Structures*. 1994, Woodbury, NY: American Institute of Physics.
50. Marcus, P.M., Surface Science, 1994. **299/300**: p. 447.
51. Schlier, R.E. and H.E. Farnsworth, *Structure and Adsorption Characteristics of Clearn Surfaces of Germanium and Silicon.* Journal of Chemical Physics, 1959. **30**(4): p. 917-926.
52. Lander, J.J., Journal of Applied Physics, 1963. **34**.
53. Takayanagi, K., et al., *Structural-Analysis of Si(111)-7x7 by UHV-Transmission Electron-Diffraction and Microscopy.* Journal of Vacuum Science & Technology a-Vacuum Surfaces and Films, 1985. **3**(3): p. 1502-1506.
54. Becker, R.S., et al., *Real-Space Observation of Surface-States on Si(111) 7x7 with the Tunneling Microscope.* Physical Review Letters, 1985. **55**(19): p. 2032-2034.
55. Binnig, G. and H. Rohrer, *Scanning Tunelling Microscopy.* Helvetica Physica Acta, 1982. **55**(6): p. 726-735.
56. Moore, G.E., Electronics, 1965. **38**.
57. Born, B., et al., *The terahertz dance of water with the proteins: the effect of protein flexibility on the dynamical hydration shell of ubiquitin.* Faraday Discussions, 2009.
58. Qvist, J., et al., *Time scales of water dynamics at biological interfaces: peptides, proteins and cells.* Faraday Discussions, 2009. **141**: p. 131-144.
59. Tobias, D.J., N. Sengupta, and N. Tarek, *Hydration dynamics of purple membranes.* Faraday Discussions, 2009. **141**: p. 99-116.
60. Beattie, J.K., A.N. Djerdjev, and G.G. Warr, *The surface of neat water is basic.* Faraday Discussions, 2009. **141**: p. 31-39.
61. Hanni-Ciunel, K., N. Schelero, and R. von Klitzing, *Negative charges at the air/water interface and their consequences for aqueous wetting films containing surfactants.* Faraday Discussions, 2009. **141**: p. 41-53.
62. Jungwirth, P., *Ions at aqueous interfaces.* Faraday Discussions, 2009. **141**.
63. Perkin, S., et al., *Dynamic properties of confined hydration layers.* Faraday Discussions, 2009. **141**.
64. Salmeron, M., et al., *Water growth on metals and oxides: binding, dissociation and role of hydroxyl groups.* Faraday Discussions, 2009. **141**: p. 221-229.
65. Held, G. and D. Menzel, *The structure of the P(Root-3x-root-3) R30-degrees Bilayer of D2O on Ru(001).* Surface Science, 1994. **316**(1-2): p. 92-102.
66. Feibelman, P.J., Physical Review B, 2007. **67**: p. 035420.

67. Feibelman, P.J., *A wetting layer breaks the ice rules.* Chemical Physics Letters, 2005. **410**(1-3): p. 120-124.
68. Haq, S., J. Harnett, and A. Hodgson, *Growth of thin crystalline ice films on Pt(111).* Surface Science, 2002. **505**(1-3): p. 171-182.
69. Zimbitas, G., S. Haq, and A. Hodgson, *The structure and crystallization of thin water films on Pt(111).* Journal of Chemical Physics, 2005. **123**(17): p. 9.
70. Glebov, A., et al., *Orientational ordering of two-dimensional ice on Pt(111).* Journal of Chemical Physics, 1997. **106**(22): p. 9382-9385.
71. Kresse, G. and J. Hafner, *Ab Initio Molecular-Dynamics for Liquid-Metals.* Physical Review B, 1993. **47**(1): p. 558-561.
72. Kresse, G. and J. Hafner, *Ab Initio Molecular-Dynamics of the Liquid-Metal Amorphous-Semiconductor Transition in Germanium.* Physical Review B, 1994. **49**(20): p. 14251-14269.
73. Kresse, G. and J. Furthmuller, *Efficient iterative schemes for ab initio total-energy calculations using a plane-wave basis set.* Physical Review B, 1996. **54**(16): p. 11169-11186.
74. Kresse, G. and J. Furthmuller, *Efficiency of ab-initio total energy calculations for metals and semiconductors using a plane-wave basis set.* Computational Materials Science, 1996. **6**(1): p. 15-50.
75. Perdew, J.P., K. Burke, and M. Ernzerhof, *Generalized gradient approximation made simple.* Physical Review Letters, 1996. **77**(18): p. 3865-3868.
76. Blochl, P.E., *Projector Augmented-Wave Method.* Physical Review B, 1994. **50**(24): p. 17953-17979.
77. Kresse, G. and D. Joubert, *From ultrasoft pseudopotentials to the projector augmented-wave method.* Physical Review B, 1999. **59**(3): p. 1758-1775.
78. Neugebauer, J. and M. Scheffler, *Adsorbate-Substrate and Adsorbate-Adsorbate Interactions of Na and K Adlayers on Al(111).* Physical Review B, 1992. **46**(24): p. 16067-16080.
79. Morgenstern, M., et al., *The ice bilayer on Pt(111): Nucleation, structure and melting.* Zeitschrift Fur Physikalische Chemie-International Journal of Research in Physical Chemistry & Chemical Physics, 1997. **198**: p. 43-72.
80. Feibelman, P.J., *Lattice match in density functional calculations: ice Ih vs. beta-AgI.* Physical Chemistry Chemical Physics, 2008. **10**(32): p. 4688-4691.
81. Chakarova-Kack, S.D., et al., *Application of van der Waals density functional to an extended system: Adsorption of benzene and naphthalene on graphite.* Physical Review Letters, 2006. **96**(14): p. 4.
82. Israelachvili, J.N., *Intermolecular and surface forces*. 2nd ed. 1991, London ; San Diego: Academic Press. xxi, 450 p.
83. Ruths, M., *Time-dependant interactions in polymer and liquid crystal systems*, in *Chemistry*. 1996, University of California-Santa Barbara: Santa Barabara. p. 181.
84. Bonander, J.R. and B.I. Kim, *Cantilever based optical interfacial force microscope.* Applied Physics Letters, 2008. **92**: p. 103124.
85. Ruths, M. and S. Granick, *Influence of alignment of crystalline confining surfaces on static forces and shear in a liquid crystal, 4 '-n-pentyl-4-cyanobiphenyl.* Langmuir, 2000. **16**(22): p. 8368-8376.

86. Bonaccurso, E., M. Kappl, and H.J. Butt, *Thin liquid films studied by atomic force microscopy.* Current Opinion in Colloid & Interface Science, 2008. **13**(3): p. 107-119.
87. Zhu, Y.X. and S. Granick, *Reassessment of solidification in fluids confined between mica sheets.* Langmuir, 2003. **19**(20): p. 8148-8151.
88. Granick, S., *Motions and relaxations of confined liquids.* Science, 1991. **253**: p. 1374-1379.
89. Cleveland, J.P., T.E. Schaffer, and P.K. Hansma, *Probing oscillatory hydration potentials using thermal-mechanical noise in an atomic-force microscope.* Physical Review B, 2003. **52**(12): p. R8692.
90. Hodgson, A. and S. Haq, *Water adsorption and the wetting of metal surfaces.* Surface Science Reports, 2009. **64**: p. 381-451.
91. Horn, R.G. and J. Israelachvili, *Direct measurement of structural forces between two surfaces in a nonpolar liquid.* Journal of Chemical Physics, 1981. **75**(3): p. 1400-1411.
92. Stewart, A.M. and J.L. Parker, *Force feedback surface force apparatus: Principles of operation.* Review of Scientific Instruments, 1992. **63**(12): p. 5626-5633.
93. Frantz, P., N. Agrait, and M. Salmeron, *Use of Capacitance to Measure Surface Forces. 1.Measuring Distance of Separation with Enhanced Spatial and Time Resolution.* Langmuir, 1996. **12**(13): p. 3289-3294.
94. Dash, J.G., *Thermomolecular Pressure in Surface Melting: Motivation for Frost Heave.* Science, 1989. **246**(4937): p. 1591-1593.
95. Takagi, S., *Approximate Thermodynamics oftThe Liquid-Like Layer on an Ice Sphere Based on an Interpretation of the Wetting Parameter.* Journal of Colloid and Interface Science, 1990. **137**(2): p. 446-455.
96. Li, Y. and G.A. Somorjai, *Surface Premelting of Ice.* Journal of Physical Chemistry C, 2007. **111**(27): p. 9631-9637.
97. Dash, J.G., H. Fu, and J.S. Wettlaufer, *The premelting of ice and its environmental consequences.* Reports on Progress in Physics, 1995. **58**: p. 115-167.
98. Doppenschmidt, A. and H.J. Butt, *Measuring the Thickness of the Liquid-liek Layer on Ice Surfaces with Atomic Force Microscopy.* Langmuir, 2000. **16**: p. 6709-6714.
99. Persson, B.N.J., *Sliding friction : physical principles and applications*. 2nd ed. Nanoscience and technology,. 2000, Berlin ; New York: Springer. xi, 515 p.
100. Meyer, E.E., K.J. Rosenberg, and J. Israelachvili, *Recent progress in understanding hydrophobic interactions.* Proceedings of the National Academy of Sciences of the United States of America, 2007. **103**(43): p. 15739-15746.
101. Spalla, O., *Long-range attraction between surfaces: existence and amplitude?* Current Opinion in Colloid & Interface Science, 2000. **5**(1-2): p. 5-12.
102. Skvarta, J., *Hydrophobic interaction between macroscopic and microscopic surfaces. Unification using surface thermodynamics.* Advances in Colloid and Interface Science, 2001. **91**(3): p. 335-390.
103. Christenson, H.K. and P.M. Claesson, *Direct measurements of the force between hydrophobic surfaces in water.* Advances in Colloid and Interface Science, 2001. **91**(3): p. 391-436.
104. Singh, S., et al., *Superhydrophobicity - Drying transition of confined water.* Nature, 2006. **442**(7102): p. 526-526.

105. Warren, O.L., S.A. Downs, and T.J. Wyrobek, *Challenges and interesting observations associated with feedback-controlled nanoindentation.* Zeitschrift Fur Metallkunde, 2004. **95**(5): p. 287-296.
106. Butt, H.J. and M. Kappl, *Normal capillary forces.* Advances in Colloid and Interface Science, 2009. **146**(1-2): p. 48-60.
107. Xu, D.W., K.M. Liechti, and K. Ravi-Chandar, *Mechanical probing of icelike water monolayers.* Langmuir, 2009. **25**(22): p. 12870-12873.
108. Sirghi, L., R. Szoszkiewicz, and E. Riedo, *Volume of a nanoscale water bridge.* Langmuir, 2006. **22**(3): p. 1093-1098.
109. de Boer, M.P., *Capillary adhesion between elastically hard rough surfaces.* Experimental Mechanics, 2007. **47**(1): p. 171-183.
110. Asay, D.B. and S.H. Kim, *Molar volume and adsorption isotherm dependence of capillary forces in nanoasperity contacts.* Langmuir, 2007. **23**(24): p. 12174-12178.
111. Moore, N.W., Unpublished data.
112. Jeffery, S., et al., *Direct measurement of molecular stiffness and damping in confined water layers.* Physical Review B, 2004. **70**(5): p. 1-8.
113. Asay, D.B. and S.H. Kim, *Evolution of the adsorbed water layer structure on silicon oxide at room temperature.* Journal of Physical Chemistry B, 2005. **109**(35): p. 16760-16763.
114. Perkin, S., et al., *Dynamic properties of confined hydration layers.* Faraday Discussions, 2008. **141**(21): p. 1-15.
115. Lane, J.M.D., et al., *Water in Nanoconfinement between Hydrophilic Self-Assembled Monolayers.* Langmuir, 2008. **24**(10): p. 5209-5212.
116. Vankeken, P.E., et al., *The Effective Viscosity of Rock-Salt - Implementation of Steady-State Creep Laws in Numerical-Models of Salt Diapirism.* Tectonophysics, 1993. **225**(4): p. 457-476.
117. Bhushan, B., J.N. Israelachvili, and U. Landman, *Nanotribology - Friction, Wear and Lubrication at the Atomic-Scale.* Nature, 1995. **374**(6523): p. 607-616.
118. Tichy, J.A. and D.M. Meyer, *Review of solid mechanics in tribology.* International Journal of Solids and Structures, 2000. **37**(1-2): p. 391-400.
119. Peschel, G. and A.K. H., *Viscosity Anomalies in Liquid Surface Zones IV. The Apparent Viscosity of Water in Thin Layers Adjacent to Hydroxylated Fused Silica Surfaces.* Journal of Colloid and Interface Science, 1970. **34**(4): p. 505-510.
120. Jinesh, K.B. and J.W.M. Frenken, *Capillary condensation in atomic scale friction: How water acts like a glue.* Physical Review Letters, 2006. **96**(16): p. -.
121. Vanalsten, J. and S. Granick, *Molecular Tribometry of Ultrathin Liquid-Films.* Physical Review Letters, 1988. **61**(22): p. 2570-2573.
122. Dhinojwala, A. and S. Granick, *Relaxation time of confined aqueous films under shear.* Journal of the American Chemical Society, 1997. **119**(1): p. 241-242.
123. Li, T.D. and E. Riedo, *Nonlinear viscoelastic dynamics of nanoconfined wetting liquids.* Physical Review Letters, 2008. **100**(10): p. -.
124. Zhu, Y.X. and S. Granick, *Viscosity of interfacial water.* Physical Review Letters, 2001. **8709**(9): p. 096104-1--4.
125. Antognozzi, M., A.D.L. Humphris, and M.J. Miles, *Observation of molecular layering in a confined water film and study of the layers viscoelastic properties.* Applied Physics Letters, 2001. **78**(3): p. 300-302.

126. Lee, M., et al., *Study of a nanoscale water cluster by atomic force microscopy.* Faraday Discussions, 2008. **141**(22): p. 1-7.
127. Leng, Y.S. and P.T. Cummings, *Fluidity of hydration layers nanoconfined between mica surfaces.* Physical Review Letters, 2005. **94**(2): p. -.
128. Tichy, J., *Rheological behavior of confined fluids in thin lubricated contacts.* Journal of Applied Mechanics-Transactions of the Asme, 2001. **68**(2): p. 278-283.
129. Klein, J. and E. Kumacheva, *Simple liquids confined to molecularly thin layers. I. Confinement-induced liquid-to-solid phase transitions.* Journal of Chemical Physics, 1998. **108**(16): p. 6996-7009.
130. Tichy, J.A., *A Surface-Layer Model for Thin-Film Lubrication.* Tribology Transactions, 1995. **38**(3): p. 577-582.
131. Feibelman, P.J., *Lubrication theory of drag on a scanning probe in structured water, near a hydrophilic surface.* Langmuir, 2006. **22**(5): p. 2136-2140.
132. Israelachvili, J., *Measurement of the Viscsoity of Liquids in Very Thin Films.* Journal of Colloid and Interface Science, 1986. **110**(1): p. 263-271.
133. Raviv, U., et al., *Viscosity of ultra-thin water films confined between hydrophobic or hydrophilic surfaces.* Journal of Physics-Condensed Matter, 2002. **14**(40): p. 9275-9283.
134. Zhu, Y.X. and S. Granick, *Limits of the Hydrodynamic No-Slip Boundary Condition.* Physical Review Letters, 2002. **88**(10): p. 106102.
135. Vanalsten, J., S. Granick, and J.N. Israelachvili, *Concerning the Measurement of Fluid Viscosity between Curved Surfaces.* Journal of Colloid and Interface Science, 1988. **125**(2): p. 739-740.
136. Warren, O.L., J.F. Graham, and P.R. Norton, *Tapping mode imaging with an interfacial force microscope.* Review of Scientific Instruments, 1997. **68**(11): p. 4124-4131.
137. Moore, N.W., and J.E. Houston, In preparation.
138. Jeffery, S., et al., *Direct measurement of molecular stiffness and damping in confined water layers.* Physical Review B, 2004. **70**(5): p. 054114.
139. McGuiggan, P.M., et al., *Friction studies of polymer lubricated surfaces.* Macromolecules, 2007. **40**(6): p. 2126-2133.
140. Maali, A., et al., *Oscillatory Dissipation of a Simple Confined Liquid.* Physical Review Letters, 2006. **96**(8): p. 086105.
141. Raviv, U., P. Laurat, and J. Klein, *Fluidity of water confined to subnanometre films.* Nature, 2001. **413**(6851): p. 51-54.
142. Sendner, C., et al., *Interfacial Water at Hydrophobic and Hydrophilic Surfaces: Slip, Viscosity, and Diffusion.* Langmuir, 2009. **25**(18): p. 10768-10781.
143. Michaelides, A., et al., *General Model for Water Monomer Adsorption on Close-Packed Transition and Noble Metal Surfaces.* Physical Review Letters, 2003. **90**(21): p. 216102.
144. Thurmer, K. and N.C. Bartelt, *Growth of multilayer ice films and the formation of cubic ice imaged with STM.* Physical Review B, 2008. **77**(19): p. 10.
145. Haq, S., et al., *Growth of intact water ice on Ru(0001) between 140 and 160 K: Experiment and density-functional theory calculations.* Physical Review B, 2006. **73**(11): p. 11.
146. Amorim, R.G., et al., *Divacancies in graphene and carbon nanotubes.* Nano Letters, 2007. **7**(8): p. 2459-2462.
147. Methfessel, M. and A.T. Paxton, *HIGH-PRECISION SAMPLING FOR BRILLOUIN-ZONE INTEGRATION IN METALS.* Physical Review B, 1989. **40**(6): p. 3616-3621.

148. Standop, S., et al., *http://arXiv.org/abs/1004.5030v1*.
149. Kimmel, G.A., et al., *Crystalline ice growth on Pt(111) and Pd(111): Nonwetting growth on a hydrophobic water monolayer.* Journal of Chemical Physics, 2007. **126**(11): p. 10.
150. Batista, E.R. and H. Jonsson, *Diffusion and Island formation on the ice Ih basal plane surface.* Computational Materials Science, 2001. **20**(3-4): p. 325-336.
151. Becke, A.D., *Density-Functional Exchange-Energy Approximation with Correct Asymptotic-Behavior.* Physical Review A, 1988. **38**(6): p. 3098-3100.
152. Perdew, J.P., et al., *Atomcs, Molecules, Solids, and Surfaces - Applications of the Generalized Gradient Approximation for Exchange and Correlation.* Physical Review B, 1993. **48**(7): p. 4978-4978.
153. Perdew, J.P., in *Electronic Structure of Solids*, P. Ziesche and H. Eschrig, Editors. 1991, Akademie Verlag: Berlin.
154. Perdew, J.P., et al., *Atomcs, Molecules, Solids, and Surfaces - Applications of the Generalized Gradient Approximation for Exchange and Correlation.* Physical Review B, 1992. **46**(11): p. 6671-6687.
155. Zhang, Y.K. and W.T. Yang, *Comment on "Generalized gradient approximation made simple".* Physical Review Letters, 1998. **80**(4): p. 890-890.
156. Hammer, B., L.B. Hansen, and J.K. Norskov, *Improved adsorption energetics within density-functional theory using revised Perdew-Burke-Ernzerhof functionals.* Physical Review B, 1999. **59**(11): p. 7413-7421.
157. Armiento, R. and A.E. Mattsson, *Functional designed to include surface effects in self-consistent density functional theory.* Physical Review B, 2005. **72**(8): p. 5.
158. Perdew, J.P., et al., *Restoring the density-gradient expansion for exchange in solids and surfaces.* Physical Review Letters, 2008. **100**(13): p. 4.
159. Perdew, J.P. and A. Zunger, *Self-interaction Correction to Density-Functional Approximations for Many-Electron Systems.* Physical Review B, 1981. **23**(10): p. 5048-5079.
160. Lee, C.T., W.T. Yang, and R.G. Parr, *Development of the Colle-Salvetti Correlation-Energy Formula into a Functional of teh Electron-Density.* Physical Review B, 1988. **37**(2): p. 785-789.
161. Ceperley, D.M. and B.J. Alder, *Ground-State of the Electron-Gas by a Stochastic Method.* Physical Review Letters, 1980. **45**(7): p. 566-569.
162. Grossman, J.C. and L. Mitas, *Efficient quantum monte carlo energies for molecular dynamics simulations.* Physical Review Letters, 2005. **94**(5): p. 4.
163. Dodson, B.W., *Many-Body Surface Strain and Surface Reconstructions in FCC Transition-Metals.* Physical Review Letters, 1988. **60**(22): p. 2288-2291.
164. Standler, R.B. *Weather Modification law in the USA*. 2006; Available from: http://www.rbs2.com/weather.pdf.
165. Pruppacher, H.R. and J.D. Klett, *Microphysics of Clouds and Precipitation*. 2nd Enlarged and Revised Edition ed. 1997, Norwell, MA: Kluwer Academic Publishers.
166. Christner, B.C., et al., *Ubiquity of biological ice nucleators in snowfall.* Science, 2008. **319**(5867): p. 1214-1214.
167. Rottger, K., et al., *Lattice-Constants and Thermal-Expansion of H2O and D2O Ice 1H Between 10 and 265 K.* Acta Crystallographica Section B-Structural Science, 1994. **50**: p. 644-648.

168. Lawn, B.R., *Thermal Expansion of Silver Iodide + Cuprous Halides.* Acta Crystallographica, 1964. **17**(11): p. 1341-&.
169. Petrenko, V.F., *Study of the surface of ice, ice/solid and ice/liquid interfaces with scanning force microscopy* Journal of Physical Chemistry B, 1997. **101**(32): p. 3276-6281.
170. Santra, B., A. Michaelides, and M. Scheffler, *On the accuracy of density-functional theory exchange-correlation functionals for H bonds in small water clusters: Benchmarks approaching the complete basis set limit.* Journal of Chemical Physics, 2007. **127**(18): p. 9.
171. Hamann, D.R., *H2O hydrogen bonding in density-functional theory.* Physical Review B, 1997. **55**(16): p. 10157-10160.
172. Kresse, G., *Private communication.* 2008.
173. Monkhorst, H.J. and J.D. Pack, *Special Points for Brillouin-Zone Integrations.* Physical Review B, 1976. **13**(12): p. 5188-5192.
174. Wu, X., et al., *Towards extending the applicability of density functional theory to weakly bound systems.* Journal of Chemical Physics, 2001. **115**(19): p. 8748-8757.
175. Feibelman, P.J., *Using Ar adsorption to estimate the van der Waals contribution to the wetting of Ru(0001).* Physical Review B, 2005. **72**(11): p. 3.
176. Da Silva, J.L.F., C. Stampfl, and M. Scheffler, *Adsorption of Xe atoms on metal surfaces: New insights from first-principles calculations.* Physical Review Letters, 2003. **90**(6): p. 4.
177. Hamann, D.R., *Comparison of global and local adaptive coordinates for density-functional calculations.* Physical Review B, 2001. **63**(7): p. 6.
178. Hamann, D.R., *Private communication.* 2008.
179. Maboudian, R., *Surface processes in MEMS technology.* Surface Science Reports, 1998. **30**(6-8): p. 209-270.
180. Szlufarska, I., M. Chandross, and R.W. Carpick, *Recent advances in single-asperity nanotribology.* Journal of Physics D-Applied Physics, 2008. **41**(12).
181. Hook, D.A., et al., *Tribological degradation of fluorocarbon coated silicon microdevice surfaces in normal and sliding contact.* Journal of Applied Physics, 2008. **104**(3).
182. Chandross, M., et al., Journal of Manufacturing Science and Engineering, 2009. **In press**.
183. Xiao, X.D., et al., *Chain length dependence of the frictional properties of alkylsilane molecules self-assembled on Mica studied by atomic force microscopy.* Langmuir, 1996. **12**(2): p. 235-237.
184. Lane, J.M.D., et al., *Water penetration of damaged self-assembled monolayers.* Langmuir, 2008. **24**(11): p. 5734-5739.
185. Asay, D.B., et al., *Macro- to nanoscale wear prevention via molecular adsorption.* Langmuir, 2008. **24**(1): p. 155-159.
186. Robbins, M.O. and P.A. Thompson, *CRITICAL VELOCITY OF STICK-SLIP MOTION.* Science, 1991. **253**(5022): p. 916-916.
187. Thompson, P.A. and M.O. Robbins, *ORIGIN OF STICK-SLIP MOTION IN BOUNDARY LUBRICATION.* Science, 1990. **250**(4982): p. 792-794.
188. Thompson, P.A., G.S. Grest, and M.O. Robbins, *PHASE-TRANSITIONS AND UNIVERSAL DYNAMICS IN CONFINED FILMS.* Physical Review Letters, 1992. **68**(23): p. 3448-3451.

189. Bitsanis, I., et al., *MOLECULAR-DYNAMICS OF FLOW IN MICROPORES.* Journal of Chemical Physics, 1987. **87**(3): p. 1733-1750.
190. Khare, R., J.J. dePablo, and A. Yethiraj, *Rheology of confined polymer melts.* Macromolecules, 1996. **29**(24): p. 7910-7918.
191. Stevens, M.J., et al., *Comparison of shear flow of hexadecane in a confined geometry and in bulk.* Journal of Chemical Physics, 1997. **106**(17): p. 7303-7314.
192. Jabbarzadeh, A., J.D. Atkinson, and R.I. Tanner, *Wall slip in the molecular dynamics simulation of thin films of hexadecane.* Journal of Chemical Physics, 1999. **110**(5): p. 2612-2620.
193. Koike, A. and M. Yoneya, *Chain length effects on frictional behavior of confined ultrathin films of linear alkanes under shear.* Journal of Physical Chemistry B, 1998. **102**(19): p. 3669-3675.
194. Gao, J.P., W.D. Luedtke, and U. Landman, *Structures, solvation forces and shear of molecular films in a rough nano-confinement.* Tribology Letters, 2000. **9**(1-2): p. 3-13.
195. Cui, S.T., et al., *Molecular dynamics study of the nano-rheology of n-dodecane confined between planar surfaces.* Journal of Chemical Physics, 2003. **118**(19): p. 8941-8944.
196. Priezjev, N.V. and S.M. Troian, *Molecular origin and dynamic behavior of slip in sheared polymer films.* Physical Review Letters, 2004. **92**(1).
197. Priezjev, N.V., *Shear rate threshold for the boundary slip in dense polymer films.* Physical Review E, 2009. **80**(3).
198. Leng, Y.S. and P.T. Cummings, *Shear dynamics of hydration layers.* Journal of Chemical Physics, 2006. **125**(10).
199. Paliy, M., O.M. Braun, and S. Consta, *The friction properties of an ultrathin confined water film.* Tribology Letters, 2006. **23**(1): p. 7-14.
200. Pertsin, A. and M. Grunze, *A computer simulation study of stick-slip transitions in water films confined between model hydrophilic surfaces. 1. Monolayer films.* Langmuir, 2008. **24**(1): p. 135-141.
201. Pertsin, A. and M. Grunze, *Quasistatic computer simulation study of the shear behavior of Bi- and trilayer water films confined between model hydrophilic surfaces.* Langmuir, 2008. **24**(9): p. 4750-4755.
202. Khomenko, A.V. and N.V. Prodanov, *Molecular dynamics simulations of ultrathin water film confined between flat diamond plates.* Condensed Matter Physics, 2008. **11**(4): p. 615-626.
203. Lorenz, C.D., et al., *In press.* Modelling and Simulation in Materials Science and Engineering, 2009.
204. Chandross, M., et al., *Simulations of nanotribology with realistic probe tip models.* Langmuir, 2008. **24**(4): p. 1240-1246.
205. Chandross, M., et al., *Systematic study of the effect of disorder on nanotribology of self-assembled monolayers.* Physical Review Letters, 2004. **93**(16).
206. Wakai, F., et al., *A Superplastic Covalent Crystal Composite.* Nature, 1990. **344**(6265): p. 421-423.
207. Untiedt, C., et al., *Fabrication and characterization of metallic nanowires.* Physical Review B, 1997. **56**(4): p. 2154-2160.
208. Kuipers, L. and J.W.M. Frenken, *Jump to Contact, Neck Formation, and Surface Melting in the Scanning Tunneling Microscope.* Physical Review Letters, 1993. **70**(25): p. 3907-3910.

209. Yanson, A.I., I.K. Yanson, and J.M. van Ruitenbeek, *Observation of shell structure in sodium nanowires.* Nature, 1999. **400**(6740): p. 144-146.
210. Wu, Y., et al., *Single-crystal metallic nanowires and metal/semiconductor nanowire heterostructures (vol 430, pg 61, 2004).* Nature, 2004. **430**(7000): p. 704-704.
211. Zhang, Y.F., et al., *Direct observation of super-plasticity of beta-SiC nanowires at low temperature.* Advanced Functional Materials, 2007. **17**(17): p. 3435-3440.
212. Han, X.D., et al., *Low-temperature in situ large strain plasticity of ceramic SiC nanowires and its atomic-scale mechanism* Nano Letters, 2007. **7**(2): p. 452-457.
213. Han, X.D., et al., *Low-temperature in situ large-strain plasticity of silicon nanowires.* Advanced Materials, 2007. **19**(16): p. 2112-2118.
214. Huang, J.Y., et al., *Superplastic carbon nanotubes - Conditions have been discovered that allow extensive deformation of rigid single-walled nanotubes.* Nature, 2006. **439**(7074): p. 281-281.
215. Wu, Y., et al., *Single-crystal metallic nanowires and metal/semiconductor nanowire heterostructures.* Nature, 2004. **430**(6995): p. 61-65.
216. Barnes, R.B., *The plasticity of rocksalt and its dependence upon water.* Physical Review, 1933. **44**(11): p. 0898-0902.
217. Carter, N.L., et al., *Rheology of Rock-Salt.* Journal of Structural Geology, 1993. **15**(9-10): p. 1257-1271.
218. Weis, D.D. and G.E. Ewing, *Water content and morphology of sodium chloride aerosol particles.* Journal of Geophysical Research-Atmospheres, 1999. **104**(D17): p. 21275-21285.
219. Finlayson-Pitts, B.J., *The tropospheric chemistry of sea salt: A molecular-level view of the chemistry of NaCl and NaBr.* Chemical Reviews, 2003. **103**(12): p. 4801-4822.
220. Shindo, H., et al., *AFM observation of monatomic step movements on NaCl(001) with the help of adsorbed water.* Surface Science, 1996. **358**(1-3): p. 111-114.
221. Sheehan, P.E., *The wear kinetics of NaCl under dry nitrogen and at low humidities.* Chemical Physics Letters, 2005. **410**(1-3): p. 151-155.
222. Westwood, A.R., *Surface-Sensitive Mechanical Properties.* Industrial and Engineering Chemistry, 1964. **56**(9): p. 15-&.
223. Gorum, A.E., E.R. Parker, and J.A. Pask, *Effect of Surface Conditions on Room-Temperature Ductility of Ionic Crystals.* Journal of the American Ceramic Society, 1958. **41**(5): p. 161-164.
224. Joffe, A., N.W. Kirpitschewa, and M.A. Lewitzky, *Deformation and solidity of crystals.* Zeitschrift Fur Physik, 1924. **22**: p. 286-302.
225. Houston, J.E. and T.A. Michalske, *The Interfacial-Force Microscope.* Nature, 1992. **356**(6366): p. 266-267.
226. Otterson, D.A., *Influence of Room-Temperature Atmospheric Reaction Products on Ductility of Sodium Chloride Single Crystals.* Journal of Chemical Physics, 1963. **38**(7): p. 1481-1486.
227. Ewing, G.E., *Ambient thin film water on insulator surfaces.* Chemical Reviews, 2006. **106**(4): p. 1511-1526.
228. Johnson, K.L., K. Kendall, and A.D. Roberts, *Surface Energy and Contact of Elastic Solids.* Proceedings of the Royal Society of London Series a-Mathematical and Physical Sciences, 1971. **324**(1558): p. 301-&.

229. Zheng, J. and J.L. Streator, *A generalized formulation for the contact between elastic spheres: Applicability to both wet and dry conditions.* Journal of Tribology-Transactions of the Asme, 2007. **129**(2): p. 274-282.
230. Colchero, J., M. Luna, and A.M. Baro, *Lock-in technique for measuring friction on a nanometer scale.* Applied Physics Letters, 1996. **68**(20): p. 2896-2898.
231. Wong, E.W., P.E. Sheehan, and C.M. Lieber, *Nanobeam mechanics: Elasticity, strength, and toughness of nanorods and nanotubes.* Science, 1997. **277**(5334): p. 1971-1975.
232. Landman, U., et al., *Atomistic Mechanisms and Dynamics of Adhesion, Nanoindentation, and Fracture.* Science, 1990. **248**(4954): p. 454-461.
233. Tomagnini, O., F. Ercolessi, and E. Tosatti, *Microscopic Interaction between a Gold Tip and a Pb(110) Surface.* Surface Science, 1993. **287**: p. 1041-1045.
234. Bartenev, G.M. and Koryakdo.Eg, *Theoretical Strength of Nacl Crystal under Tension Along Its Body and Face Diagonals.* Izvestiya Vysshikh Uchebnykh Zavedenii Fizika, 1968(3): p. 100-&.
235. Suresh, S. and J. Li, *Materials Science Deformation of the Ultra-Strong.* Nature, 2008. **456**(7223): p. 716-717.
236. Sun, L.T., et al., *Plastic Deformation of Single Nanometer-Sized Crystals.* Physical Review Letters, 2008. **101**(15): p. -.
237. Roberts, M.W. and J.M. Thomas, *Surface and Defect Properties of Solids*. Vol. 4. 1975, London: The Chemical Society.
238. Allen, H.C., M.L. Mecartney, and J.C. Hemminger, *Minimizing transmission electron microscopy beam damage during the study of surface reactions on sodium chloride.* Microscopy and Microanalysis, 1998. **4**(1): p. 23-33.
239. Ahn, C.C. and O.L. Krivanek, *EELS Atlas*. 2007, Warrendale, PA: Gatan, Inc.
240. Muray, A., et al., *Radiolysis and resolution limits of inorganic halide resists.* Journal of Vacuum Science & Technology b 1985. **3**(1): p. 367-372.
241. Herrmann, F., P. Pinard, and Y. Farge, *About the displacement of the lithium ion in lithium fluoride by accelerated electrons.* Journal of Physics C-Solid State Physics, 1974. **7**(11): p. L199-L201.
242. Karch, J., R. Birringer, and H. Gleiter, *Ceramics Ductile at Low-Temperature.* Nature, 1987. **330**(6148): p. 556-558.
243. Du, Y., et al., *A parameter study of separation modes of adhering microcontacts.* Journal of Applied Physics, 2008. **103**(6): p. -.
244. Kendall, K., C.W. Yong, and W. Smith, *Deformation of NaCl particle in contact at the nano-scale.* Powder Technology, 2007. **174**(1-2): p. 2-5.
245. Verrall, R.A., R.J. Fields, and M.F. Ashby, *Deformation-Mechanism Maps for Lif and Nacl.* Journal of the American Ceramic Society, 1977. **60**(5-6): p. 211-216.
246. Gyulai, Z., *Festigkeits Und Plastizitatseigenschaften Von Nacl-Nadelkristallen.* Zeitschrift Fur Physik, 1954. **138**(3-4): p. 317-321.
247. Turchanyi, G., *Sodium Chloride Whiskers.* Nature, 1961. **190**(477): p. 79-80.
248. Bluhm, H., et al., *The premelting of ice studied with photoelectron spectroscopy.* Journal of Physics-Condensed Matter, 2002. **14**(8): p. L227-L233.
249. Dosch, H., A. Lied, and J.H. Bilgram, *Surface Melting of Ice 1(H) Single-Crystals Revealed by Glancing Angle X-Ray-Scattering.* Physical Review Letters, 1994. **72**(22): p. 3554-3557.

250. Golecki, I. and C. Jaccard, *Surface of ice near 0-Degrees-C Studied by 100 keV Proton Channeling.* Physics Letters A, 1977. **63**(3): p. 374-376.
251. Elbaum, M., S.G. Lipson, and J.G. Dash, *Optical Study of Surface Melting on Ice.* Journal of Crystal Growth, 1993. **129**(3-4): p. 491-505.
252. Gilpin, R.R., *Wire Regelation at Low-Temperatures.* Journal of Colloid and Interface Science, 1980. **77**(2): p. 435-448.
253. Wilson, P.W., J.W. Arthur, and A.D. Haymet, *Ice premelting during differential scanning calorimetry.* Biophysical Journal, 1999. **77**(5): p. 2850-2855.
254. Doppenschmidt, A., M. Kappl, and H.J. Butt, *Surface properties of ice studied by atomic force microscopy* Journal of Physical Chemistry B, 1998. **102**(40): p. 7813-7819.
255. Pittenger, B., et al., *Premelting at ice-solid interfaces studied via velocity-dependent indentation with force microscope tips* Physical Review B, 2001. **63**(13): p. 134102/1-15.
256. Bluhm, H., T. Inoue, and M. Salmeron, *Friction of ice measured using lateral force microscopy* Physical Review B, 2000. **61**(11): p. 7760-7765.
257. Hosler, C.L. and R.E. Hallgren, *The aggregation of small ice crystals.* Discussions of the Faraday Society, 1960. **30**(200).
258. Hellett, J., *Temperature Dependence of Viscosity of Supercooled Water.* Proceedings of the Physical Society of London, 1963. **82**(530).
259. Jellinek, H.H.G., *Liquid-like (transition) layer on ice.* Journal of Colloid and Interface Science, 1967. **25**(2).
260. Wehl, W.A., *Surface structure of water and some of its physical and chemical manifestations.* Journal of Colloid Science, 1951. **6**(5): p. 389-405.
261. Rosenberg, R., *Why is ice slippery?* Physics Today, 2005. **58**(12): p. 50-55.
262. Bowden, F.P. and T.P. Hughes, *The mechanism of sliding on ice and snow* Proceedings of the Royal Society of London Series a-Containing Papers of a Mathematical and Physical Character, 1939. **172**(A949): p. 280-298.
263. Persson, B.N.J., et al., *On the origin of Amonton's friction law.* Journal of Physics C-Solid State Physics, 2008. **20**(39): p. 395006.
264. Telford, J.W. and J.S. Turner, *Motion of a wire through ice.* PHILOSOPHICAL MAGAZINE, 1963. **8**(87).
265. Bhushan, B., *Nanotribology and Nanomechanics : An Introduction*. 2005, Berlin: Springer. xxviii, 1148.
266. Waters, J.F., S. Lee, and P.R. Guduru, *Mechanics of axisymmetric wavy surface adhesion: JKR-DMT transition solution.* International Journal of Solids and Structures, 2009. **46**(5): p. 1033-1042.
267. Attard, P. and J.L. Parker, *DEFORMATION AND ADHESION OF ELASTIC BODIES IN CONTACT.* Physical Review A, 1992. **46**(12): p. 7959-7971.
268. Ding, Y.R., *Micro/nano-particle manipulation and adhesion studies.* Journal of Adhesion Science and Technology, 2008. **22**(5): p. 457-480.
269. Packham, D.E., *Work of adhesion: contact angles and contact mechanics.* International Journal of Adhesion and Adhesives, 1996. **16**: p. 121-128.
270. Attard, P., *Friction, adhesion, and deformation: dynamic measurements with the atomic force microscope.* Journal of Adhesion Science and Technology, 2002. **16**(7): p. 753-791.
271. Kumar, G., et al., *Scaling of van der Waals and electrostatic adhesion interactions from the micro- to the nano-scale.* Journal of Adhesion Science and Technology, 2008. **22**(5-6): p. 407-428.

272. Craig, V., *An historical review of surface force measurement techniques.* Colloids and Surfaces a-Physicochemical and Engineering Aspects, 1997. **129-130**: p. 75-94.
273. Claesson, P.M., et al., *Techniques for measuring surface forces.* Advances in Colloid and Interface Science, 1996. **67**: p. 119-183.
274. Derjaguin, B.V., V.M. Muller, and Y.P. Toporov, *Effect of Contact Deformations on the Adhesion of Particles.* Journal of Colloid and Interface Science, 1975. **53**(2): p. 314-326.
275. Shi, X. and Y.-P. Zhao, *Comparison of various adhesion contact theories and the in uence of dimensionless load parameter.* Journal of Adhesion Science and Technology, 2004. **18**(1): p. 55-68.
276. Barthel, E., *On the Description of the Adhesive Contact of Spheres with Arbitrary Interaction Potentials.* Journal of Colloid and Interface Science, 1998. **200**: p. 7-18.
277. Butt, H.J., B. Cappella, and M. Kappl, *Force measurements with the atomic force microscope: Technique, interpretation and applications.* Surface Science Reports, 2005. **59**(1-6): p. 1-152.
278. Leckband, D. and J. Israelachvili, *Intermolecular forces in biology.* Quarterly Reviews of Biophysics, 2001. **34**(2): p. 105-267.
279. Leite, F.L. and P.S.P. Herrmann, *Application of atomic force spectroscopy (AFS) to studies of adhesion phenomena: a review.* Journal of Adhesion Science and Technology, 2005. **19**(3-5): p. 365-405.
280. Nosonovsky, M. and B. Bhushan, *Phase behavior of capillary bridges: towards nanoscale water phase diagram.* Physical Chemistry Chemical Physics, 2008. **10**(16): p. 2137-2144.
281. Thomas, R.C., et al., *Probing Adhesion Forces at the Molecular Scale.* Journal of the American Chemical Society, 1995. **117**: p. 3830-3834.
282. Houston, J.E., et al., *Comparative study of the adhesion, friction, and mechanical properties of CF3- and CH3-terminated alkanethiol monolayers.* Langmuir, 2005. **21**(9): p. 3926-3932.
283. Kim, S.H., D.B. Asay, and M.T. Dugger, *Nanotribology and MEMS.* Nano Today, 2007. **2**(5): p. 22-29.
284. Schwarz, U.D., *A generalized analytical model for the elastic deformation of an adhesive contact between a sphere and a flat surface.* Journal of Colloid and Interface Science, 2003. **261**(1): p. 99-106.
285. Greenwood, J.A. and K.L. Johnson, *An alternative to the Maugis model of adhesion between elastic spheres.* Journal of Physics D-Applied Physics, 1998. **31**(22): p. 3279-3290.
286. Xu, D.W., K.M. Liechti, and K. Ravi-Chandar, *On the modified Tabor parameter for the JKR-DMT transition in the presence of a liquid meniscus.* Journal of Colloid and Interface Science, 2007. **315**(2): p. 772-785.
287. Yang, F., *Effect of adhesion energy on the contact stiffness in nanoindentation.* Journal of Materials Research, 2006. **21**(10): p. 2683-2688.
288. de Boer, P.C.T. and M.P. de Boer, *Rupture work of pendular bridges.* Langmuir, 2008. **24**(1): p. 160-169.
289. de Boer, M.P. and P.C.T. de Boer, *Thermodynamics of capillary adhesion between rough surfaces.* Journal of Colloid and Interface Science, 2007. **311**: p. 171-185.

290. Argento, C. and R.H. French, *Parametric tip model and force-distance relation for Hamaker constant determination from atomic force microscopy.* Journal of Applied Physics, 1996. **80**(11): p. 6081-6090.
291. Sumant, A.V., et al., *Surface chemistry and bonding configuration of ultrananocrystalline diamond surfaces and their effects on nanotribological properties.* Physical Review B, 2007. **76**(23): p. 235429-1--235429-11.
292. Knauss, W.G. and V.H. Kenner, *On the Hygrothermomechanical Characterization of Polyvinyl Acetate.* Journal of Applied Physics, 1980. **51**(10): p. 5131-5136.
293. Chen, L., et al., *Ductile separation and its role in the evolution of gold contacts.* Proceedings of the Asme/Stle International Joint Tribology Conference, Pts a and B, 2008: p. 803-805 1131.
294. Chen, L., et al., *Separation modes in microcontacts identified by the rate dependence of the pull-off force.* Applied Physics Letters, 2008. **93**(5): p. -.
295. Komkov, O.Y., *Influence of Liquid Meniscus on Surface Forces.* Journal of Friction and Wear, 2007. **28**(1): p. 19-31.
296. Weeks, B.L. and J.J. DeYoreo, *Dynamic Meniscus Growth at a Scanning Probe Tip in Contact with a Gold Substrate.* Journal of Physical Chemistry B, 2009. **110**(21): p. 10231-10233.
297. Hinterdorfer, P. and Y.F. Dufrêne, *Detection and localization of single molecular recognition events using atomic force microscopy.* Nature Methods, 2006. **3**(5): p. 347 - 355.
298. Smith, W.L., *ProbeView v.1.8.6j1*. 2003, Sandia National Laboratories: Albuquerque. p. IFM instrument control and data logging software.
299. Houston, J.E., *Personal communication*.
300. Kushmerick, J.G., et al., *Hydration forces on protein-resistant polyethylene oxide surfaces.* Abstracts of Papers of the American Chemical Society, 2001. **221**: p. U357-U357.
301. Major, R.C., et al., *Tribological properties of alkoxyl monolayers on oxide terminated silicon.* Tribology Letters, 2003. **14**(4): p. 237-244.
302. Goertz, M.P., *Personal communication.*
303. Houston, J.E., *A local-probe analysis of the rheology of a "Solid liquid".* Journal of Polymer Science Part B-Polymer Physics, 2005. **43**(21): p. 2993-2999.
304. Goertz, M.P., X.Y. Zhu, and J.E. Houston, *Temperature Dependent Relaxation of a "Solid-Liquid".* Journal of Polymer Science Part B-Polymer Physics, 2009. **47**(13): p. 1285-1290.
305. Mesbah-Nejad, A., M. Moallem, and R.V. Patel, *Modeling and Control of a New Actuation Mechanism for Interfacial Force Microscopy.* Proceedings, American Control Conference, 2008. **2008**: p. 2052-2057.
306. Bao, M., et al., *Squeeze-film air damping of a torsion mirror at a finite tilting angle.* Journal of Micromechanics and Microengineering, 2006. **16**: p. 2330-2335.
307. Landman, U., W.D. Luedtke, and J.P. Gao, *Atomic-scale issues in tribology: Interfacial junctions and nano-elastohydrodynamics.* Langmuir, 1996. **12**(19): p. 4514-4528.
308. Hughes, B.D. and L.R. White, *Implications of Elastic Deformation on the Direct Measurement of Surface Forces.* Journal of the Chemical Society-Faraday Transactions 1, 1980. **76**: p. 963-978.

309. Chan, D.Y.C. and R.G. Horn, *The Drainage of Thin Liquid-Films between Solid-Surfaces.* Journal of Chemical Physics, 1985. **83**(10): p. 5311-5324.
310. Patil, S., et al., *A highly sensitive atomic force microscope for linear measurements of molecular forces in liquids.* Review of Scientific Instruments, 2005. **76**(10): p. 103705.
311. Houston, J.E. and W.L. Smith, *Laser Interferometry Force-Feedback Sensor for an Interfacial Force Microscope*, U.S.P. Office, Editor. 2004: United States.
312. Brake, M.R., et al., *Modeling and Measurement of a Bistable Beam in a Microelectromechanical System.* Journal of Microelectromechanical Systems, In press.
313. Mitchell, J.A., et al., *The Sandia MEMS Passive Shock Switch Sensor: FY07 Maturation Activities*, U.S.D.o. Energy, Editor. 2008, Sandia National Laboratories: Albuquerque. p. 71-80.
314. Wu, B., A. Heidelberg, and J.J. Boland, *Mechanical properties of ultrahigh-strength gold nanowires.* Nature, 2005. **4**: p. 525-529.
315. Moore, D.F., *The Friction and Lubrication of Elastomers*. 1972, Oxford: Pergamon Press. 288.
316. Tichy, J.A., *Modeling of Thin-Film Lubrication.* Tribology Transactions, 1995. **38**(1): p. 108-118.
317. Tichy, J.A., *A Porous-Media Model for Thin-Film Lubrication.* Journal of Tribology-Transactions of the Asme, 1995. **117**(1): p. 16-21.
318. Xu, D.W., K.M. Liechti, and K. Ravi-Chandar, *Mesoscale scanning probe tips with subnanometer rms roughness.* Review of Scientific Instruments, 2007. **78**(7): p. -.
319. Kunert, C., J. Harting, and O.I. Vinogradova, *Random-Roughness Hydrodynamic Boundary Conditions.* Physical Review Letters, 2010. **105**: p. 016001.
320. Ibrahim, M.B. and S. Veluri. *CFD Modeling of Surface Roughness in Laminar Flow*. in *2nd International Energy Conversion Engineering Conference*. 2004. Providence, Rhode Island: American Institute of Aeronautics and Astronautics,.
321. Pashley, R.M. and J. Israelachvili, *Molecular Layering of Water in Thin Films between Mica Surfaces and Its Relation to Hydration Forces.* Journal of Colloid and Interface Science, 1984. **101**(2): p. 511-523.
322. Perkin, S., et al., *Dynamic properties of confined hydration layers.* Faraday Discussions, 2008. **141**: p. 399-413.
323. Ruths, M., *Time-Dependent Interactions in Polymer and Liquid Crystal Systems* 1996, University of Californa-Santa Barabara: Santa Barabara, CA. p. 181.
324. Tjiptowidjojo, K., *Personal communication.* 2010.
325. Schmelzer, J.W.P., *Pressure Dependence of Viscosity.* Journal of Chemical Physics, 2005. **122**(7): p. 074511.
326. Granick, S. and Y. Zhu, *Slippery questions about complex fluids flowing past solids.* Nature Materials, 2003. **2**: p. 221-227.
327. Bonaccurso, E., M. Kappl, and H.J. Butt, *Hydrodynamic force measurements: Boundary slip of water on hydrophilic surfaces and electrokinetic effects.* Physical Review Letters, 2002. **88**(7): p. -.
328. Vinogradova, O.I., *Drainage of a Thin Liquid-Film Confined between Hydrophobic Surfaces.* Langmuir, 1995. **11**(6): p. 2213-2220.
329. Jarvis, S.P., et al., *Local Solvation Shell Measurement in Water Using a Carbon Nanotube Probe.* Journal of Physical Chemistry B, 2000. **104**(26): p. 6091-6094.

330. O'Shea, S.J., *Comment on "Oscillatory Dissipation of a Simple Confined Liquid".* Physical Review Letters, 2006. **97**(17): p. 179601.
331. Kapusta, P., et al., *Time-Resolved Fluorescence Anisotropy Measurements Made Simple.* Journal of Fluorescence, 2003. **13**(2): p. 179-183.
332. Tovbina, Z.M., V.S. Kuts, and V.V. Strelko, *Study of the Proton Relaxation Times of Water in the Pores of Silica Gels Having Different Structures.* Teoreticheskaya iEksperimentaPnaya Khimiya, 1969. **5**(6): p. 848-850.
333. Arnau, A., Y. Jimenez, and T. Sogorb, *An Extended Butterworth-Van Dyke Model for Quartz Crystal Microbalance Applications in Viscoelastic Fluid Media.* IEEE Transactions on Ultrasonics, Ferroelectrics, and Frequency Control, 2001. **48**(5): p. 1367-1382.
334. Branch, D.W., et al., *Shear Horizontal Surface Acoustic Wave Microsensor for Class A Viral and Bacterial Detection*, S.N. Laboratories, Editor. 2008: Albuquerque, NM.
335. Salomaki, M. and J. Kankare, *Large Apparent Interfacial Slippage at Polyelectrolyte-Perfluorocarbon Interfaces on a Quartz Crystal Resonator.* Langmuir, 2004. **20**(18): p. 7794-7801.
336. Yoshimoto, M., S. Tokimura, and S. Kurosawa, *Characteristics of the series resonant-frequency shift of a quartz crystal microbalance in electrolyte solutions.* The Analyst, 2006. **131**(131): p. 1175-1182.
337. Bowen, W.R. and H.N.S. Yousef, *Effect of salts on water viscosity in narrow membrane pores.* Journal of Colloid and Interface Science, 2003. **2003**: p. 452-457.
338. Reiter, G., et al., *Anomalous Behavior of Proton Zero Point Motion in Water Confined in Carbon Nanotubes.* Physical Review Letters, 2006. **97**(24): p. 247801.
339. Goertz, M.P., X.Y. Zhu, and J.E. Houston, *Temperature Dependent Relaxation of a ''Solid–Liquid''.* Journal of Polymer Science Part B-Polymer Physics, 2009. **47**: p. 1285-1290.
340. Khan, S.H., et al., *Dynamic Solidification in Nanoconfined Water Films.* Physical Review Letters, 2010. **105**(10): p. 106101.

Distribution

| | | | |
|---|---|---|---|
| 1 | MS0359 | Donna Chavez | 1911 |
| 1 | MS0899 | Technical Library | 9536 (electronic copy) |
| 1 | MS1303 | Gary Grest | 1114 |
| 1 | MS1314 | Matthew Goertz | 1132 |
| 1 | MS1415 | Carlos Gutierrez | 1114 |
| 1 | MS1415 | Peter Feibelman | 1130 |
| 1 | MS1415 | Gary Kellogg | 1114 |
| 1 | MS1415 | Nathan Moore | 1114 |


Sandia National Laboratories